UNIVERSITI TEKNOLOGI MARA

STUDY OF HYBRID TERNARY ZN-NI-CO/GRAPHENE NANOPLATELET COMPOSITE FOR SUPERCAPACITOR APPLICATIONS

NURUL INFAZA TALALAH BINTI RAMLI

PhD

March 2026

UNIVERSITI TEKNOLOGI MARA

STUDY OF HYBRID TERNARY ZN-NI-CO/GRAPHENE NANOPLATELET COMPOSITE FOR SUPERCAPACITOR APPLICATIONS

NURUL INFAZA TALALAH BINTI RAMLI

Thesis submitted in fulfilment
of the requirements for the degree of
Doctor of Philosophy
(Science)

Faculty of Applied Sciences

March 2026

CONFIRMATION BY PANEL OF EXAMINERS

I certify that a Panel of Examiners has met on 8 January 2026 to conduct the final examination of Nurul Infaza Talalah binti Ramli on her Doctors of Philosophy thesis entitled "Study of Hybrid Ternary Zn-Ni-Co/Graphene Nanoplatelet Composite for Supercapacitor Applications" in accordance with Universiti Teknologi MARA Act 1976 (Akta 173). The Panel of Examiners recommends that the student be awarded the relevant degree. The Panel of Examiners was as follows:

Abdel Baset M.A Ibrahim, PhD
Associate Professor
Faculty of Applied Sciences
Universiti Teknologi MARA
(Chairman)

Zakiah Mohamed, PhD
Associate Professor
Faculty of Applied Sciences
Universiti Teknologi MARA
(Internal Examiner)

Zurina Osman, PhD
Professor
Faculty of Science
Universiti Malaya
(External Examiner)

PROFESSOR DR HJH ZURAEDA IBRAHIM
Dean
Institute of Postgraduates Studies
Universiti Teknologi MARA

Date: 25 March 2026

AUTHOR'S DECLARATION

I declare that the work in this thesis was carried out in accordance with the regulations of Universiti Teknologi MARA. It is original and is the results of my own work, unless otherwise indicated or acknowledged as referenced work. This thesis has not been submitted to any other academic institution or non-academic institution for any degree or qualification.

I, hereby, acknowledge that I have been supplied with the Academic Rules and Regulations for Post Graduate, Universiti Teknologi MARA, regulating the conduct of my study and research.

Name of Student	:	Nurul Infaza Talalah binti Ramli
Student ID. No.	:	2021239984
Programme	:	Doctor of Philosophy (Science) – AS950
Faculty	:	Applied Sciences
Thesis Title	:	Study of Hybrid Zn-Ni-Co/Graphene Nanoplatelet Composite for Supercapacitor Applications
Signature of Student	:	……..
Date	:	March 2026

ABSTRACT

The evolution of the electrode materials for supercapacitor has become a pivotal role for advancing energy storage technologies. Among promising candidates, ternary mixed transition metal oxides (MTMOs) consisting of zinc (Zn), nickel (Ni), and cobalt (Co) offer multiple redox states, high theoretical capacitance, and tuneable electrochemical properties. However, the influence of Zn: Ni: Co stoichiometry and their interaction with conductive additives such as graphene nanoplatelets (GNPs) remains underexplored. This study aims to bridge these gaps by systematically synthesizing Zn Ni Co MTMOs with varying ratios (1:1:1, 1:2:1, 1:1:2, and 2:1:1) via the sol gel method and evaluating their electrochemical enhancement upon GNP incorporation (0.1, 0.2, and 0.3 wt.%). The synthesized materials were characterized using XRD, FESEM, EDX, FTIR, BET, and Raman spectroscopy, and evaluated in a three-electrode system using cyclic voltammetry (CV), galvanostatic charge discharge (GCD), electrochemical impedance spectroscopy (EIS), and Dunn's analysis in 2 M KOH electrolyte. Among the samples, ZNC-GNP 0.2 exhibited the best performance with a specific capacitance of 478 Fg^{-1} at 5 mV s^{-1}, owing to the synergistic contributions of electric double layer capacitance (EDLC) from GNP and the pseudocapacitive behaviour of the MTMOs. Dunn's analysis confirmed a predominantly diffusion-controlled charge storage mechanism (85% contribution at 5 mV s^{-1}), gradually transitioning to increased capacitive contributions (up to 44%) at higher scan rates, indicating hybrid storage behaviour. The ZNC GNP 0.2 electrode also demonstrated excellent cyclic stability, retaining 97.05% of its initial capacitance after 1000 cycles, comparable to the performance of similar MTMOs-carbon systems. GCD confirmed hybrid supercapacitor behavior with favorable energy and power density of 24.06 Wh/kg and 1375 W/kg, respectively shown by ZNC-GNP 0.2 sample. EIS results revealed the lowest solution resistance (Rs = 5.43 Ω) and charge transfer resistance among all compositions, further confirming enhanced ion diffusion and electronic conductivity. In contrast, excessive GNP content (0.3 wt.%) resulted in increased resistance due to agglomeration, while insufficient GNP (0.1 wt.%) limited conductive network formation. Overall, the findings underscore the critical role of compositional optimization and carbon integration in achieving high performance, stable, and conductive supercapacitor electrodes. The ZNC GNP system, particularly at 0.2 wt.% GNP, offers a balanced architecture combining high energy density, long term stability, and efficient charge transport, positioning it as a strong candidate for advanced energy storage applications in portable electronics, electric vehicles, and grid systems.

ACKNOWLEDGEMENT

I would like to express my deepest gratitude to my supervisors Prof Dr. Ab Malik Marwan Ali, Dr. Nur Hafiz bin Hussin, Assoc. Prof. Dr. Mohamad Fariz Mohamad Taib, and Prof. Ts. Dr. Oskar Hasdinor Hassan for their invaluable guidance, continuous support, and constructive feedback throughout the course of this research. Their expertise, patience, and encouragement have been crucial in shaping this thesis. I am deeply grateful for their unwavering belief in me, especially during moments when I doubted my own abilities.

I also sincerely thank the examiners for their insightful comments and suggestions, which have greatly improved the quality of this work.

My appreciation extends to the academic and technical staff of Faculty of Applied Science UiTM Pahang Branch, Jengka campus and UiTM Shah Alam for their assistance, particularly in providing laboratory facilities, administrative support, and technical guidance.

Finally, I would like to thank my family and friends for their unwavering encouragement, understanding, and emotional support throughout this journey. Their belief in me has been a constant source of motivation. This thesis is also specially dedicated to my mother and my late father. This piece of victory is dedicated to both of you. Alhamdulillah.

TABLE OF CONTENTS

LIST OF TABLES

LIST OF FIGURES

LIST OF SYMBOLS

Symbols

v	Potential scan rates
λ	Wavelength
ε	Molar absorptivity
ρ	Saturation pressure
α	Absorbance

LIST OF ABBREVIATIONS

Abbreviations

BET	Brunauer Emmett Teller
BJH	Barrett-Joyner-Halenda
CNTs	carbon nanotubes
CV	Cyclic voltammetry
EDLC	electrochemical double layer capacitors
EIS	Electrochemical Impedance Spectroscopy
EDX	Energy-Dispersive Spectroscopy
FESEM	Field-Emission Scanning Electron Microscopy
FTIR	Fourier Transform Infrared Spectroscopy
GCD	Galvanostatic charge-discharge cycle
GNFs	graphitic nanofibers
GNP	Graphene Nanoplatelet
GO	Graphene oxide
MOF	metal-organic framework
MTMOs	mixed transition metal oxides
PCs	Pseudocapacitors
SCs	supercapacitor
TMOs	transition metal oxides

XRD	X-ray Diffraction
ZNC	Zn-Ni-Co
ZNC-GNP	Zn-Ni-Co-GNP

CHAPTER 1
INTRODUCTION

1.1 Research Background

Society has become increasingly reliant on electronic devices, including mobile phones, computers, tablets, and various energy-powered machines. Of all the components that contributed to functioning the aforementioned devices, the vital aspect that will determine the performance of those devices is its energy storage system. Hypothetically, devices with excellent storage ability, together with a swift charging process will boost the quality rating of a specific device. By far, the benchmark for good energy storage devices is currently conquered by supercapacitors (SCs). Where, the storage process occurs via reversible faradaic reaction or surface-based redox reaction.

There are two distinct groups of SCs namely as electrochemical double layer capacitors (EDLCs) and Pseudocapacitors (PCs). EDLCs store energy by means of reversible ion adsorption on the electrode/electrolyte interface. EDLCs are commonly associated with carbon-based materials such as carbon nanotubes (CNTs), graphene, graphene oxide (GO), graphitic nanofibers (GNFs) and graphite. On the contrary, the storage mechanism of PCs is based on the rapid intercalation courses or reversible redox reactions on the electrode surface (Wang *et al*., 2020). Compared to EDLC, PCs are completely non- electrostatic in nature and arise as a consequence of electrochemical charge-transfer accompanied by the finite amount of active material. Since the storage is based on redox reactions, to some extent, PCs are similar to a battery in terms of its behaviour (Muzaffar *et al*., 2019).

Though EDLCs and PCs undergo different kinds of reaction, both charge mechanisms exist in an electrochemical capacitor. Consequently, based on the materials; one storage mechanism becomes the dominant contributor to the specific capacitance while the other contributes very little. Since the mainstream direction of energy storage research is to improve both energy and power density simultaneously, PCs are more favourable as they can store energy both at the interfaces and within the inner side of the electrode. In terms of capacitance, PCs are able to perform 10-100

times more than the normal EDLCs, thus justify its selection in this specific study.

PCs electrode materials mainly belong to three categories: transition metal oxides (TMOs), transition metal nitrides and conductive polymers. Among the lists, TMOs have been researched extensively as their capacitances often exceed the achievable double-layer capacitance of carbon materials (Yi *et al*., 2018). However, poor electrical conductivity, rate capability and low initial coulombic efficiency are a stumbling block for their practical use. Research has proved that an effective method of circumventing these drawbacks is via formation of mixed transition metal oxides (MTMOs) prepared by the combination of various transition metal cations stoichiometrically or non-stoichiometrically (Ezeigwe *et al*., 2020). Previously reported studies supported that the MTMOs have exhibited a better electrochemical performance if compared to the TMOs alone. This is due to the relatively low activation energy in MTMOs for electron transfer between cations which will improve electrical conductivity and shorten the diffusion paths for ionic transportation.

To date, various research has been steered towards the formation of composite materials, with the aim to improve the electrochemical performance of the device. For instance, it is noteworthy that spinel $NiCo_2O_4$ demonstrates an ultrahigh specific capacitance of 1400 Fg^{-1} under a mass loading of 0.4 $mgcm^2$ from an epoxide-driven sol-gel process (Zhu *et al*., 2014). Spinel $NiCo_2O_4$ not only has the advantages of low cost, environmental friendliness, and abundant resources, but also possesses a much better electronic conductivity (at least two orders of magnitude higher) and higher electrochemical activity compared with NiO and Co_3O_4, its single counterparts.

The pseudocapacitive electrochemical performance of 2D material-metal oxide nanocomposites has shown significant improvement, making them promising candidates for next-generation energy storage devices. Extensive research has demonstrated that 2D materials exhibit superior supercapacitance properties compared to their individual components, highlighting their potential for enhanced energy storage. For instance, a performance review gathered by Sahoo *et al*., (2023) proved that combined metal oxide-based electrode that combines two TMOs such as ruthenium oxide (RuO_2), manganese oxide (MnO_2), nickel oxide (NiO), iron oxide (Fe_3O_4), and cobalt oxide (Co_3O_4).

Given this, TMOs nanocomposite particularly Zn-Ni-Co-based systems are

expected to offer even greater performance benefits due to their broadened redox activity, improved intrinsic conductivity, and enhanced structural stability (González-Banciella *et al*. 2024; Marwat *et al*. 2024; Zhang *et al*. 2023). However, systematic studies exploring how Zn-Ni-Co stoichiometric ratios influence electrochemical performance remain limited. Moreover, despite the potential of combining these ternary oxides with conductive carbonaceous materials such as graphene nanoplatelets (GNPs) to boost electron transport, porosity, and mechanical integrity, there is a lack of detailed investigations into how such composites store charge at the mechanistic level.

In particular, the application of analytical tools such as Dunn's analysis to distinguish between surface capacitive and diffusion-controlled contributions in Zn-Ni-Co–GNP composites have rarely been reported. This represents a significant gap, as understanding the charge-storage mechanism is essential for the rational design of high-performance SCs. Addressing this gap, the present study focuses on synthesizing and optimizing Zn-Ni-Co ternary metal oxides with varying stoichiometric ratios, evaluating the influence of GNPs incorporation on their structural and electrochemical properties, and applying Dunn's analysis to elucidate their charge storage behaviour. This approach is anticipated to enhance the fundamental understanding of ternary TMO–carbon composites and guide the development of high-performance alternative electrode materials for the next-generation SCs.

1.2 Problem Statement

SCs have emerged as vital energy storage systems due to their exceptional features, including high power density, rapid charge–discharge rates, and long cycle life. These advantages make them ideal candidates for integration into modern electronic devices and renewable energy systems. However, a persistent challenge hindering their widespread application is the relatively low energy density, which is intrinsically limited by the nature of the electrode materials used (Naseri *et al*., 2022).

Among the various electrode materials explored, ruthenium oxide RuO_2 has demonstrated outstanding supercapacitive performance, with high specific capacitance, excellent rate capability, and remarkable cycling stability. These attributes are attributed to its highly reversible redox reactions and superior electronic conductivity.

Nonetheless, the practical deployment of RuO_2 in commercial supercapacitors is severely constrained by its high cost and scarcity, making it economically unviable for large-scale applications (Mevada & Mukhopadhyay, 2020).

In pursuit of cost-effective alternatives, researchers have investigated single transition metal oxides (TMOs) for instance NiO (Dhas *et al*., 2020), TiO_2 (Da Silva *et al*., 2019), ZnO (Zhao *et al*., 2018), Co_3O_4 (Ezeigwe *et al*., 2020), and Fe_3O_4 (Kim *et al*., 2020). These materials offer promising pseudocapacitive behaviour due to their multiple oxidation states. However, their practical application is limited by poor intrinsic electrical conductivity and structural instability, resulting in low-rate capabilities and limited cycling performance.

To overcome these limitations, hybrid structures combining TMOs with conductive materials such as carbon nanotubes (CNTs), graphene, and conductive polymers have been explored (Wu *et al*., 2020). While these hybrids improve conductivity and surface area, they often suffer from inadequate synergistic interaction and non-uniform dispersion, leading to only moderate improvements in capacitance and limited long-term stability.

Another approach involves forming binary metal oxides, such as $NiCo_2O_4$ (Liang *et al*., 2023) and $ZnCo_2O_4$ (Han *et al*., 2019), which exhibit enhanced electrochemical activity due to synergistic redox behaviour. However, these systems still encounter issues such as electrical resistance and limited redox versatility, hindering their overall performance.

Recently, attention has shifted towards ternary metal oxides (TMOs), where three different metal cations inclusive of Zn, Ni, Co, Mn, and Fe are combined to leverage multivalent redox reactions, improved conductivity, and enhanced structural integrity. For instance, ternary system such as Zn-Ni-Co (Zhang *et al*., 2023), Zn-Ni ferrites (Thokoane *et al*., 2024), and Co-Mn-Zn (Suganya *et al*., 2022) have been reported to exhibit synergistic effects arising from the coexistence of multiple redox-active cations. These ternary systems offer the potential to balance and enhance electrochemical performance by integrating the beneficial properties of each constituent. However, their performance is still hampered by suboptimal porosity, particle agglomeration, and relatively low surface area, resulting in incomplete utilization of active sites (Kiaeerad & Naji, 2021).

To address these challenges, researchers have begun incorporating ternary TMOs with carbonaceous materials such as GNPs, which offer excellent conductivity, high surface area, and mechanical stability. This hybrid approach aims to enhance charge transport and structural integrity. However, current studies often lack a systematic investigation of how variations in the Zn-Ni-Co ratios, when composited with GNPs, affect electrochemical performance. Moreover, there is limited application of analytical methods such as Dunn's analysis to distinguish between surface capacitive and diffusion-controlled charge storage processes in such hybrid systems.

Improving energy and power density while maintaining high cycling stability remains a key objective in supercapacitor research. One promising strategy is by the integration of transition metal oxides with conductive carbonaceous materials, which is anticipated to enhance electron transport, redox activity, and structural stability (Pramitha & Raviprakash, 2022). In particular, the combination of TMOs with GNPs is hypothesized to promote synergistic effects that could improve electrochemical performance. However, a comprehensive understanding of how different metal ratios interact with GNPs to influence charge storage behaviour is still lacking.

Therefore, this study aims to fill the existing knowledge gap by optimizing the electrochemical performance of Zn-Ni-Co ternary metal oxides through stoichiometric variation, evaluating the effect of GNPs addition, and analyzing the charge storage mechanisms using Dunn's analysis to support the development of high-performance, cost-effective, and stable electrode materials for next-generation supercapacitors.

1.3 Research Objective

This work proposed a comprehensive study on the synthesis of the ternary mixed transition metal oxides – Graphene Nanoplatelet nanocomposite that can function better as SCs electrodes. The specific objectives of this work are:

i. To optimize the electrochemical performance of Zn-Ni-Co ternary metal oxides with varying metal stoichiometric ratios.
ii. To evaluate the structural, morphological, and electrochemical characteristics of GNP addition to the optimized ternary metal oxide.
iii. To investigate the electrochemical performance of ZNC–GNP composite based on energy and power density measurements and charge storage

contributions using Dunn's analysis.

1.4 Research Scope and Limitations

This research is primarily focused on investigating the supercapacitive behaviour of advanced hybrid nanocomposites derived from ternary mixed-transition metal oxides (MTMOs) comprising zinc (Zn), nickel (Ni), and cobalt (Co). These materials are further modified through the incorporation of graphene nanoplatelets (GNPs) to enhance their electrochemical properties and structural stability. The synthesized nanocomposites will be comprehensively analysed to establish a fundamental understanding of their charge storage mechanisms, physicochemical characteristics, and energy storage capabilities. The research is structured around four core dimensions:

i. Material Synthesis:

The first phase of the research involves the synthesis of Zn-Ni-Co MTMOs (ZNC) with four distinct metal cation ratios: 1:1:1, 1:2:1, 1:1:2, and 2:1:1. These MTMOs will be synthesized using the sol–gel method, which offers better compositional control and homogeneity. The specific capacitance (Cs) obtained from initial electrochemical testing will be used as a performance metric to determine the most promising ZNC composition. Once the optimal composition is identified, the study will proceed to the second phase, where the selected ZNC material will be composited with graphene nanoplatelets at varying weight percentages (0.1 wt.%, 0.2 wt.%, and 0.3 wt.%) to enhance the surface area, and overall electrochemical response.

ii. Material Characterization:

The structural, morphological, and elemental properties of the synthesized samples will be examined through a suite of characterization techniques, including X-ray diffraction (XRD), Field Emission Scanning Electron Microscopy (FESEM), Energy Dispersive X-ray Spectroscopy (EDX), Brunauer–Emmett–Teller (BET) surface area analysis, and Fourier Transform Infrared Spectroscopy (FTIR). These techniques will be employed to confirm the successful formation of the desired crystal phases, determine particle size and morphology, analyse elemental distribution, and assess porosity and surface chemistry. The combination of these analytical tools will provide a comprehensive physicochemical profile of both the unmodified and GNP-modified

materials.

iii. Electrochemical Performance Evaluation:

The electrochemical behaviour of the MTMOs and their corresponding GNP composites will be investigated using standard electrochemical techniques, with a focus on assessing their performance as potential electrode materials for supercapacitor applications. Cyclic voltammetry (CV), galvanostatic charge–discharge (GCD) testing, and electrochemical impedance spectroscopy (EIS) will be employed to evaluate specific capacitance, charge–discharge efficiency, rate capability, and electrical resistance. Energy density and power density will be calculated to determine the practical energy storage potential of the materials. Furthermore, Dunn's analysis will be conducted to deconvolute the contribution of surface capacitive versus diffusion-controlled mechanisms, offering deeper insight into the underlying charge storage behaviour of the composites.

iv. Data Analysis and Optimization:

The final phase of the research focuses on comparing the performance of different ZNC compositions and their GNP-enhanced variants. A detailed analysis will be conducted to identify the most efficient composition in terms of electrochemical output, structural integrity, and stability. This phase aims to optimize the material design parameters to support the development of high-performance, cost-effective electrode materials suitable for next-generation supercapacitor systems.

Despite the contributions and importance of this work that have been mentioned above, certain limitations must be acknowledged. Herein, there are three categories of limitations of this work inclusive of:

i. Material Composition Constraints:

The study is limited to Zn-Ni-Co-based MTMOs and does not extend to other possible combinations of transition metal oxides such as MnO_2, Fe_2O_3, or V_2O_5. Furthermore, only three predetermined GNP loadings (0.1, 0.2, and 0.3 wt.%) will be explored. The influence of other GNP concentrations or alternative carbon-based additives like carbon nanotubes (CNTs) or activated carbon is beyond the scope of this investigation.

ii. Characterization Limitations:

While a comprehensive range of characterization techniques is employed, the

study does not include advanced surface chemistry analysis tools such as X-ray Photoelectron Spectroscopy (XPS) or Transmission Electron Microscopy (TEM). These techniques could provide additional insight into oxidation states, chemical bonding, and atomic-level morphology, which are not explored in this study due to equipment and time constraints.

iii. Computational or Theoretical Modelling:

This research is based entirely on experimental methodologies and does not incorporate computational simulations or theoretical modelling approaches such as density functional theory (DFT), molecular dynamics, or finite element analysis. While such modelling could complement and deepen the understanding of charge transfer dynamics and atomic-scale interactions, they fall outside the experimental nature and timeline of this work.

Despite these limitations, the outcomes of this research are expected to make a significant contribution to the fundamental understanding of ternary metal oxide systems and their hybridization with carbon-based materials. By elucidating the relationships between composition, structure, and electrochemical performance, this study will add valuable knowledge to the growing field of nanostructured electrode materials for energy storage technologies.

1.5 Significant of Study

The demand for an outstanding energy storage device has garnered extensive research into advanced materials for supercapacitor electrode. MTMOs such as Zn-Ni-Co-based materials appear to be a promising options owing to their multiple redox states and high theoretical capacitance. However, a fundamental understanding of how compositional variations influence their physicochemical and electrochemical properties remains limited.

This work aims to bridge this knowledge gap by systematically inquire into the synthesization of Zn-Ni-Co MTMOs with varying Zn: Ni: Co ratios via the sol-gel method. By implementing comprehensive material characterization via XRD, FESEM, EDX, BET, and FTIR, this research will contribute to the fundamental understanding of the physicochemical properties of MTMO which is crucial for advancing energy storage technologies.

Furthermore, while MTMOs exhibit excellent electrochemical potential, their Cs value and charge storage efficiency require further enhancement. On the other hand, GNP is known for their ability to improve electrical conductivity and charge storage performance. By incorporating GNP at different weight percentages, this study aims to optimize electrode composition and investigate its impact on energy and power density. These findings will provide insights into the synergistic interactions between MTMOs and 2D materials, reinforcing the role of nanocomposites in enhancing supercapacitor efficiency and sustainability.

Another key contribution of this work is its investigation into the charge storage mechanisms of Zn-Ni-Co/GNP composites. Utilization of Dunn's analysis will provide a key insight into the difference between surface capacitive and diffusion-controlled charge storage contributions, offering a deeper theoretical understanding of energy storage behaviour. The results will be instrumental in guiding future material design strategies for high-performance supercapacitors.

This research also aligns with Malaysia's National Energy Policy (2022-2040), which emphasizes energy sustainability, technological innovation, and the promotion of green energy solutions. By exploring high-performance electrode materials for supercapacitors, this study contributes to the nation's goals of enhancing energy security, reducing reliance on fossil fuels, and advancing clean energy technologies. Additionally, it supports Malaysia's National Nanotechnology Policy and Strategy (2021-2030) by promoting nanomaterials research for advanced applications, fostering innovation in energy storage, and strengthening Malaysia's position in the global scientific community.

Despite certain limitations as listed in previous sub-chapter, this work provides a strong foundation for further exploration in energy storage applications. The knowledge generated will not only enhance the fundamental understanding of MTMOs and their composites but also serve as a reference for future studies aimed to optimize nanocomposite materials for next-generation energy storage devices, supporting Malaysia's vision for a sustainable and technology-driven future. Moreover, this work is expected to give a positive impact to the society, economy, and nation by introducing a new material that can function better than the existing material for SCs that are currently available in the market. In line with prosperity vision 2030,

strategic thrust 2: Key economic growth (KEGA), the emphasis on industrialization has been the thrust of this specific research. This project also develops a new high-performance material for supercapacitor application, which will contribute to the automotive and automobile industry. Specifically, this study will contribute to:

i. New knowledge on the relationship between Zn: Ni: Co composition and the physicochemical properties of MTMOs by systematically evaluating different Zn-Ni-Co ratios (111, 121, 112, 211) through XRD, FESEM, EDX, BET, and FTIR characterization.
ii. New insights into the sol-gel synthesis parameters that influence the structural integrity, crystallinity, and surface properties of Zn-Ni-Co-based MTMOs and their composites with GNP.
iii. New findings on the electrochemical performance of Zn-Ni-Co MTMOs, particularly their specific capacitance, energy density, and power density, through cyclic voltammetry and charge-discharge measurements.
iv. A deeper understanding of the synergistic effects of ternary metal oxides and 2D materials by assessing the impact of GNP incorporation at different weight percentages (0.1, 0.2, 0.3 wt.%) on charge storage mechanisms.
v. New theoretical insights into charge storage behaviour in Zn-Ni-Co/GNP composites using Dunn's analysis to differentiate between surface capacitive and diffusion-controlled contributions, contributing to fundamental advancements in supercapacitor electrode materials.

1.6 Thesis Organization

This thesis is structured into five chapters, each designed to build upon the previous one and provide a comprehensive understanding of the research conducted. The flow of the chapters mirrors the research process which started from problem identification and literature analysis to methodology, results interpretation, followed by final conclusions and sets of recommendations.

Chapter 1 presents an overview of the entire study by outlining the background and motivations behind the investigation. It highlights the limitations of existing electrode materials used in SCs applications, particularly the persistent challenge of low energy density despite their high-power density and long cycle life. This chapter

establishes the research gap and frames the central problem on how to improve the energy storage capacity of supercapacitor electrodes without compromising other critical performance parameters. The research problem is systematically translated into specific research aims and objectives that guide the entire study. Additionally, this chapter defines the scope and delimitations of the research, ensuring that the study remains focused on its intended contribution.

Chapter 2 provides a critical review of the literature related to supercapacitors. It begins with a general overview of supercapacitor types and their operational mechanisms, followed by an in-depth discussion on the various classes of electrode materials previously explored. Special attention is given to transition metal oxides and carbon-based materials, including their individual and synergistic properties. The chapter also examines the fundamental charge storage mechanisms inclusive of both electric double-layer and pseudocapacitive behaviour, and summarizes different synthesis routes for hybrid materials, particularly metal oxide–carbon composites. This review helps establish the theoretical and experimental foundation upon which the present work is built.

Chapter 3 details the research methodology employed in this study. It elaborates on the synthesis approach used to prepare Zn-Ni- MTMOs and their composites with GNPs. The chapter also outlines the characterization techniques used to assess the materials' physicochemical properties and electrochemical performance. This includes the sequence of experiments, material processing parameters, and evaluation criteria.

Chapter 4 presents and discusses the results of the experimental work. It analyses the structural, morphological, and compositional properties of the synthesized materials. Additionally, this chapter evaluates the electrochemical performance of each sample in terms of specific capacitance, energy density, and power density. The effectiveness of GNP incorporation is discussed in detail, with emphasis on performance improvements and charge storage mechanisms. Comparative analysis between different metal ratios and GNP loadings is also included to support material optimization.

Finally, chapter 5 concludes the thesis by summarizing the key findings of the study in relation to the original research objectives. It highlights how the experimental

results contribute to the broader understanding of properties and performance relationships in ternary MTMO-based supercapacitor electrodes. The chapter reflects on the scientific significance of incorporating GNP for enhanced electrochemical properties. Furthermore, it outlines the limitations encountered during the study and provides several recommendations for future research. These include exploring other metal oxide combinations, broader GNP concentration ranges, advanced surface analysis techniques, and integration of computational modelling to deepen the mechanistic insights of energy storage systems.

CHAPTER 2
LITERATURE REVIEW

2.1 Overview of Energy Storage System

Over the last few years, there has been a significant rise in demand for energy storage technologies, largely driven by the growing need for sustainable and renewable power sources. Traditional fossil fuels offer only finite supplies, heightening interest in materials that enable clean energy. Dependence on non-renewables has depleted reservoirs, worsened climate change, and sparked conflicts. The need for solutions has prompted researchers to concentrate their efforts on inventing advanced and upgraded systems to store energy. Batteries were once the most widely used form of energy storage, prior to supercapacitors gaining substantial traction commercially. Batteries convert chemical energy into electrical energy by shuttling electrons between electrodes, prompted by an internal chemical reaction. Batteries can store more energy in a smaller space and operate at higher voltages than other options, but they lack durability over many cycles. The chemicals become depleted over time as well, resulting in fading charge capacity that shortens usable battery life (Olabi *et al*., 2022) . Despite higher energy density and voltage, these drawbacks of low stability and lifespan have posed challenges for batteries.

Fuel cells on the other hand, work similarly to batteries but do not deplete their charge over time. Although fuel cells are efficient, their expensive catalysts and continual fuel requirements restrict their possible applications (Poonam *et al*., 2019). Capacitors store electric charge between two plates, enabling rapid charging, longevity, and low maintenance (Ramachandran *et al*., 2023). However, conventional capacitors store less energy overall and lose voltage quickly. They offer less capacitance per unit volume than batteries as well. The emergence of supercapacitors, also termed ultracapacitors, overcame some key limitations faced by batteries, fuel cells, and capacitors. Supercapacitors charge rapidly like capacitors but store more energy through optimized materials and structural designs. This breakthrough has resolved major concerns around cost, fuel dependence, cycle life, and stability.

Supercapacitors store energy through a charging and discharging process

occurring at the electrode-electrolyte interface. The fundamental energy storage principle of supercapacitors is similar to that of conventional capacitors. However, a key difference lies in the rapid release and storage of energy. Supercapacitors have porous electrodes with a larger surface area, leading to a significant improvement in specific capacitance. The specific capacitance value of a supercapacitor can be several hundred to several thousand times higher than a conventional capacitor. While the storage capacity of conventional capacitors is typically in the microfarad or millifarad range, supercapacitors have capacities of a few hundred farads. Additionally, supercapacitors have a much lower equivalent series resistance compared to ordinary capacitors.

Selecting electrode materials with excellent electrical conductivity and a large specific surface area (SSA) is key for developing high-performance supercapacitors. Figure 2.1 displays a Ragone plot comparing different energy storage technologies - fuel cells, conventional batteries, supercapacitors and traditional capacitors - in terms of their power and energy densities. This plot highlights the strengths of supercapacitors, which bridge the gap between high-power, low-energy density conventional capacitors and low-power, high-energy density batteries. Table 2.1 presents the comparison of essential characteristics of the battery, supercapacitor, and conventional capacitor adapted from Borges *et al*., (2013). By carefully optimizing the electrode materials, supercapacitors can combine moderate energy density with very high-power density.

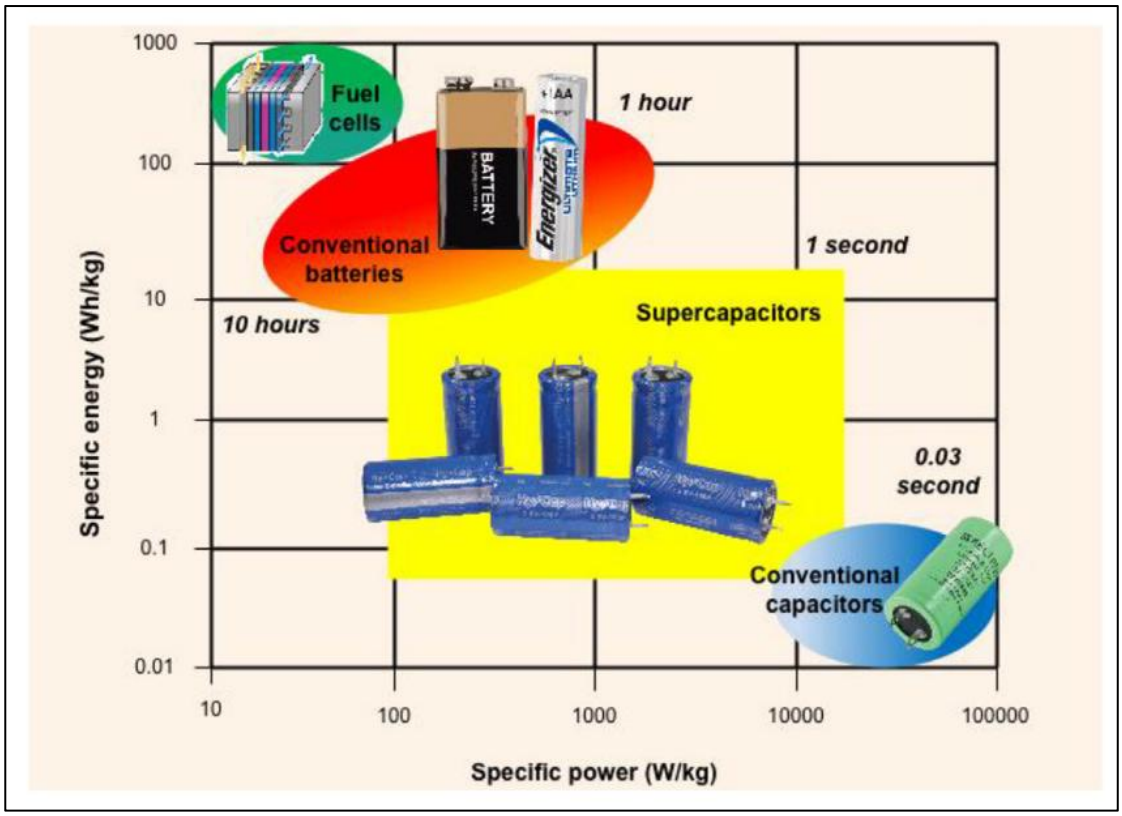

Figure 2.1 Graph of specific energy versus specific power for different types of energy storage devices (adapted from:(Mohd Abdah *et al.*, 2020)

Table 2.1

Comparison of essential characteristics of the battery, supercapacitor, and conventional capacitor

Characteristics	Battery	Supercapacitor	Conventional capacitor
Charging/discharging time	1 to 10 h	Milliseconds to seconds	Picoseconds to milliseconds
Energy density	8 to 600 Wh/kg	1 to 10 Wh/kg	0.01 to 0.05 Wh/kg
Power density	0.005 to 0.4 Wh/kg	1 to 120 Wh/kg	0.25 to 10,000 Wh/kg
Weight	1 to > 10kg	0.001 to 0.230 kg	1 to 10 kg
Operating voltage	1.25 to 4.2 V	6 to 800 V	2.3 to 2.75 V
Life	150 to 1500 cycles	> 50,000 cycles	>100,000 cycles

2.2 Classification of Supercapacitor

According to (Mohd Abdah *et al.*, (2020) , supercapacitors can be classified into three main groups (EDLC, pseudocapacitor, and hybrid capacitor), by referring to

their electrochemical performances, as can be seen on Figure 2.2. A glance on the cyclic voltammetry (CV) curves can describe the behaviour of the electrode materials. In most cases, EDLCs appeared to be current-independent, while battery-like materials showed a separate reduction and oxidation peaks on its CV curves. Moreover, EDLC's constant current discharge presents a linear E versus t plot, while the battery-like material is nonlinear with the existence of plateaus. Figure 2.3 shows the comparison of EDLCs-type and PCs-like material. Each cycle will provide a mirror image of the charging and discharging process that represent the reversible reaction. An ideal capacitor represented by a rectangular shape voltammetry profile as shown in figure 2.3. When electrochemical capacitors are associated with a resistive component, the measured current varies linearly depending on the contribution from the resistive component. The pseudocapacitive behaviour not only originates from the electric double layer such as that in EDLCs but also from the faradaic redox reactions of the electrolyte species. Faradaic redox pseudocapacitance occurs when the ions adsorbed onto the electrode material via faradaic charge-transfer. The ion might as well intercalate into the layer of a redox-active material also via faradaic charge-transfer process. This is called intercalation pseudocapacitance. The electron charge transfer between electrolyte and the active electrode is coming from the de-solvated and adsorbed ions. In contrast to the case of an ideal EDLCs, the charging and discharging of a PCs takes place through faradaic processes involving electron transfer across the electrode/solution interface. Usually, PCs can obtain greater specific capacitance and energy density compared to EDLCs since the faradaic process not only occurs on the surface but also within the body of the electrode (Obodo *et al.*, 2020).

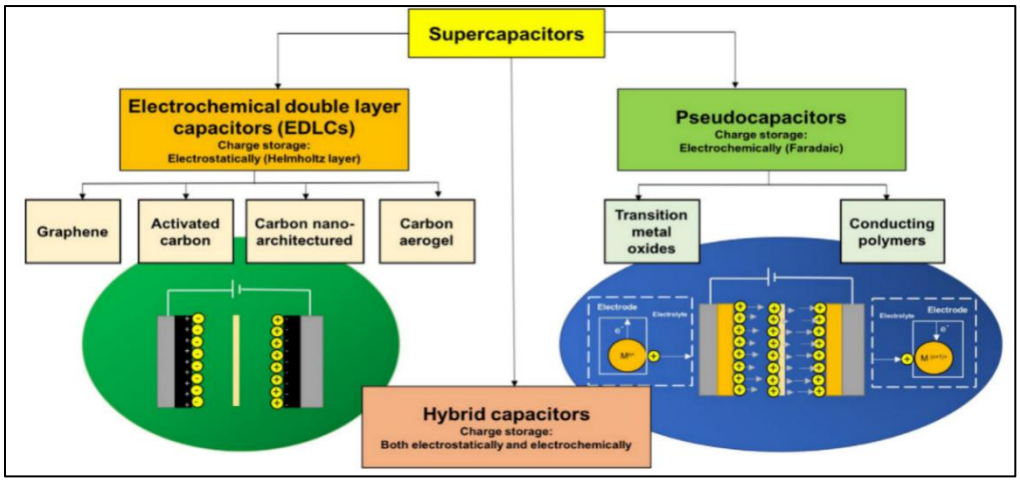

Figure 2.2 Classification of supercapacitors (adapted from: Mohd Abdah *et al.*, 2020)

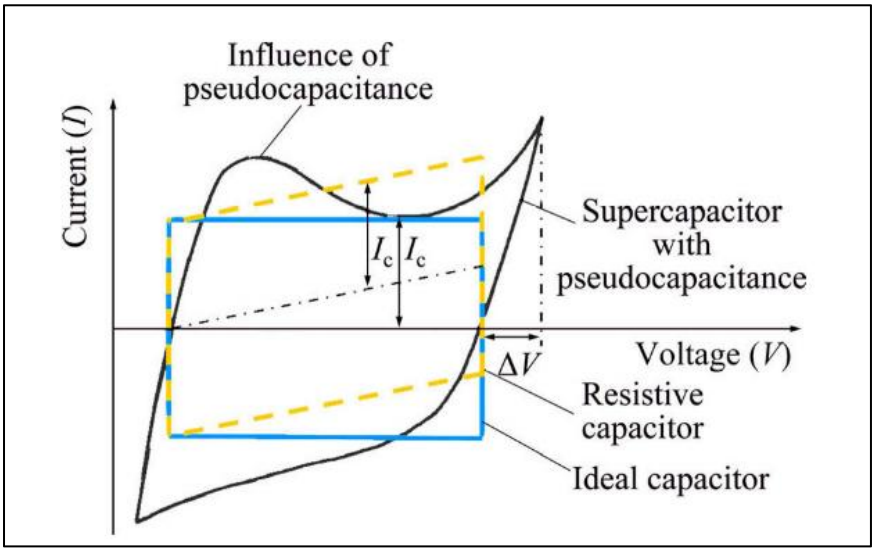

Figure 2.3 Fundamental difference between current curves of EDLCs and PCs (adapted from: Yi *et al.*, 2018)

2.2.1 Electrochemical Double Layer Capacitor

In general, the storage capacity of Electrochemical Double-Layer Capacitors (EDLCs) depends on the buildup of electrostatic charge at the electrode-electrolyte interface (Liu *et al.*, 2021) . This process involves the physical adsorption of ions, without any accompanying chemical reactions. When a voltage is applied across the EDLC, electrons flow through the external circuit from the negative to the positive electrode, resulting in the accumulation of positive and negative charges on the respective electrodes. Subsequently, cations from the electrolyte solution migrate towards the negative electrode, while anions move towards the positive electrode. The

discharge phase reverses this process. In this type of SCs, the reversible adsorption and desorption of ions leads to the formation of double electric layers at the electrode-electrolyte interface, thus allowing energy to be stored within the double-layer interfaces. EDLCs typically have a higher energy density than conventional capacitors due to the concentration of the potential drop within a confined region (0.1–10 nm). As a result, the capacitance of EDLCs is closely related to the interfacial area of the electrodes (Saikia *et al*., 2020) . These electrodes primarily consist of highly porous carbon-based materials with expansive surface areas, such as graphene, activated carbon, activated carbon fibre, and carbon nanotubes (CNTs) (Liu *et al*., 2021) . Extensive research has highlighted the notable attributes of these electrode materials, including high conductivity and robust mechanical stability. However, the lack of a Faraday redox reaction in the energy storage process limits the charge mechanism, confining the capacitance to a narrow range. Consequently, although EDLCs exhibit a relatively high-power density, they manifest a low specific capacitance and energy density.

2.2.2 Pseudocapacitor

The second type of SCs is pseudocapacitors (PCs) which belong to a category characterized by the reversible redox reaction between surface functional groups and electrolyte ions (Liu *et al*., 2021) . Pseudocapacitive energy storage involves conducting polymers, certain oxide compounds of transition metals like ruthenium and manganese, and carbon materials doped with heteroatoms (Saikia *et al*., 2020) . Generally, pseudocapacitors exhibit significantly higher specific capacitance compared to EDLCs (Suganya *et al*., 2023) . The effectiveness of electrochemical supercapacitors is contingent upon the attributes of their active materials. However, their capacity retention under high current density and prolonged operation is limited due to the sluggish and deteriorative nature of the redox process.

PCs contain two major types of pseudo-capacitance: redox pseudocapacitance and intercalation pseudocapacitance (Liu *et al*., 2021) . Redox pseudo-capacitance involves the adsorption of ions from the electrolyte solution on or near the electrode surface, enabling electron transfer during the redox process. On the other hand, PCs through intercalation entails the insertion of electrolyte ions into voids or layers within

active electrode materials, coupled with a charge transfer process.

2.2.3 Hybrid Capacitor

A hybrid capacitor, constituting a third category of supercapacitors, is essentially a hybridization of a non-faradaic EDLCs-type electrode on one end and a faradaic battery-type electrode on the other end. The battery-type electrode typically consists of transition metal oxides, sulphides, phosphides, and similar materials(Liu *et al*., 2021) . Hybrid capacitors are engineered to function in tandem, fulfilling the simultaneous needs for power and energy density. One acts as a capacitive electrode, while the other functions as a faradaic electrode. Typically, carbon-derived materials are employed as the negative electrode, with a metal or metal oxide electrode serving as the anode. Metal electrodes, known for their high intrinsic volumetric capacity, contribute to enhanced energy densities (Najib & Erdem, 2019) . Hybrid capacitors typically demonstrate significant operational potential and deliver higher capacitance than standalone EDLCs or PCs. Depending on the arrangement of electrodes, hybrid capacitors can be either symmetric or asymmetric. A symmetric assembly consists of identical electrode components, while an asymmetric assembly is composed of dissimilar electrodes (Pramitha & Raviprakash, 2022) . For easy understanding of the SCs classification, Figure 2.4 provides a summary of the classification of electrochemical capacitors.

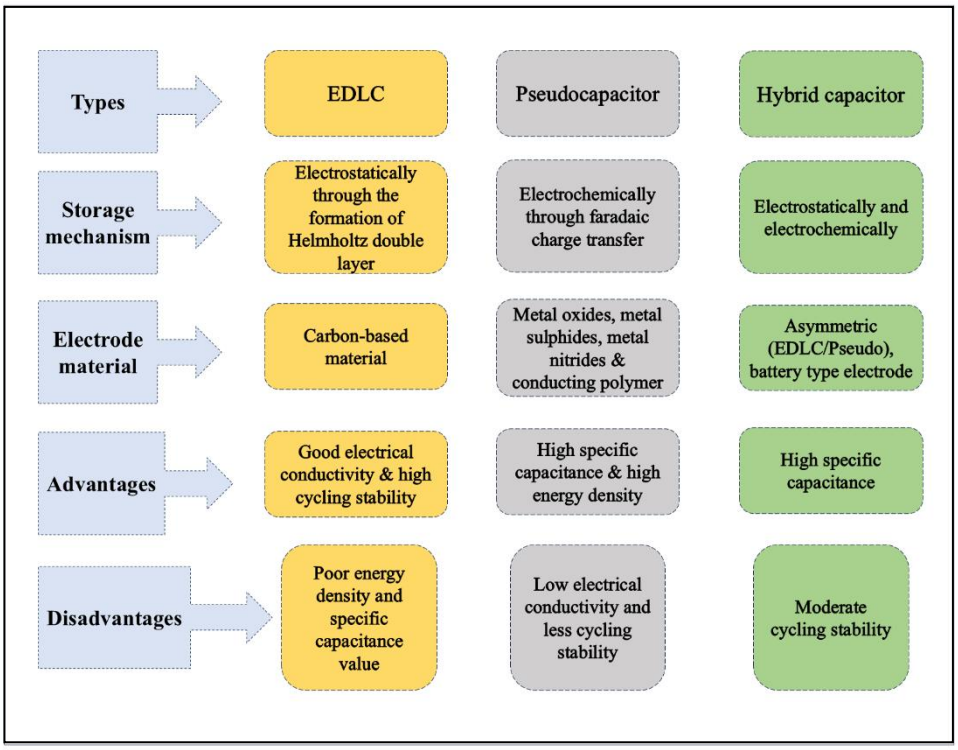

Figure 2.4 classification of electrochemical capacitors (adapted from: Pramitha & Raviprakash, 2022).

2.3 Electrolytes for supercapacitor

In a typical supercapacitor setup, it comprises electrode, electrolyte, current collector, binder, and separator. The active elements in supercapacitors consist of the electrolyte and electrode, while the current collector, binder, and separator are deemed as inactive components. Of all components mentioned, electrode materials play a vital role in determining the supercapacitance, hence the importance of electrode materials optimization. In order for a supercapacitor material to be considered as superior, it should exhibit the following traits: effective conductivity, substantial specific surface area, favourable stability, outstanding reversibility, facile preparation route and abundance in nature (L. Wang *et al.*, 2023). One of the main obstacles that hinder the supercapacitive performance is the energy density values. Enhanced energy density is achievable by either improving the capacitance of electrode materials or altering the operating potential. Notably, the expansion of the voltage window holds potential benefits for augmenting the device's energy density. The robustness of cell potential

largely relies upon the electrochemical stability of the electrolyte employed to prevent undesirable and exhaustive reactions. Therefore, selecting a suitable electrolyte is crucial. Electrolytes are vital in supercapacitors as they facilitate the chemical reactions at the electrodes. Consequently, three classes of electrolyte are available, encompassing aqueous, organic, ionic liquid (IL), ionic gel, and solid-state electrolytes (Zhou *et al*., 2018). The summary of electrolyte classes and its operating potential is listed in Table 2.2.

2.3.1 Aqueous Electrolytes

Among the three classes of electrolytes, aqueous electrolytes stand out as the most utilized and researched. Among the most notable aqueous electrolytes heavily used in the supercapacitor realm are Na_2SO_4, H_2SO_4, KCl, KOH, NaOH, and NaCl (Patel *et al*., 2021) . Aqueous electrolyte is known to have a potentially high conductivity. Yet, the stability limit for aqueous electrolytes is considerably low, which ranged from 1.0 V to 1.3 V (Fong *et al*., 2017). Aqueous electrolytes also offer a combination of better ionic concentration and reduced resistance, hence facilitating improved power performance when compared to organic electrolytes. Thus, supercapacitors utilizing an aqueous electrolyte solution could potentially exhibit greater capacitance and higher power output over organic electrolytes (Zhou *et al*., 2018) . X. Wang *et al*., (2023) utilized 6 M KOH in the electrochemical characterization setup. The same work also compares the performance of two other electrolytes: organic and ionic liquid. To summarize the findings, Aqueous electrolyte shows highest capacitance (457 Fg^{-1}) compared to organic (261 Fg^{-1}) and ionic liquid (250 Fg^{-1}). The outstanding performance of 6 M aqueous KOH is analogous to high ionic conductivity and electrolyte accessibility to electrode pores (X. Wang *et al*., 2023).

2.3.2 Organic Electrolytes

Another known class of electrolyte is organic electrolyte (OE). It possesses a higher range of potential window (2.5-2.7 V) (Fong *et al*., 2017) . Apart from its upstanding potential, the preparation procedure of OE is more rigorous as compared to aqueous electrolytes, which makes it the less popular option in supercapacitors (Zhou

et al., 2018). There have been numerous reports on the usage of OE. For instance, a non-flammable triethyl phosphate (TEP)-based binary electrolyte was studied by S. Li *et al*., (2023). It was found that it can operate at a wider potential window, up to 2.5 V. However, based on open circuit potential (OCP), the potential degrades from 2.5 V to 1.4 V upon 20 h of charging. The decomposition of electrolyte that causes capacity attenuation is common in organic-type electrolyte (Y. Wang *et al*., 2012). In a work conducted by Banavath *et al*., (2022), 1 M $TEABF_4$ in ACN was verified to have wider usable operating potential of 1.8 V compared to 1 V for aqueous, allowing higher energy density storage. In the same work, Banavath *et al*., compared the electrolyte performance of 1 M $TEABF_4$ in ACN with 1 M KOH aqueous electrolyte. The obtained specific capacitance when using OE was uncovered to be 26 Fg^{-1} and 86 Fg^{-1} for aqueous electrolyte. The capacity retention for aqueous electrolyte was better (38%) whilst OE settled at 33% retention at higher scan rates. In short, it is evidence that while OE enables higher voltage window and energy density, the higher conductivity aqueous electrolyte allows better capacitance, rate capability, and charge-discharge speeds (Banavath *et al*., 2022).

2.3.3 Ionic Liquid

Apart from aqueous and organic electrolyte, ionic liquid (IL) represents another category of electrolytes. IL are composed of salts with a low melting temperature and consist of inherently conducting ions. The crucial characteristics of ionic liquids, such as thermal stability, electrochemical stability across a broad potential range, and non-toxicity, are essential for their application in supercapacitors (Patel *et al*., 2021). Moreno-Fernández *et al*., (2021) proved the effectiveness of 1-Ethyl-3-methylimidazolium bis (trifluoromethyl sulfonyl) imide (EMI TFSI) by comparing it with aqueous and organic electrolyte. In terms of supercapacitance values, IL shows greater values over OE, but lower values compared to aqueous electrolyte. Moreover, EMI TFSI allows maximum voltage window (~3V) enabling highest energy density but has limitations in power performance due to high viscosity. Another electrolyte performance comparison reported by B. Liu *et al*., (2023) supports the capacitance trend mentioned before. They describe the capacitance value for aqueous electrolyte as the highest (247 Fg^{-1}), followed by IL and OE, which shows the

same value (188 Fg^{-1}). In summary, while aqueous KOH enables highest capacitance, the ionic liquid and organic electrolytes allow wider voltage stability window leading to significantly higher energy density. The prepared electrodes also demonstrate excellent compatibility with all three electrolytes.

2.3.4 Comparisons of Various Electrolytes

The comparative overview of the operating potentials of various electrolyte systems, classified into aqueous, organic, and ionic liquid types is presented in Table 2.2. From the table, it is evident that aqueous electrolytes like KOH, H_2SO_4, and Na_2SO_4 possess lower operating potentials ranging from 0.5 to 1.2 V. On the other hand, organic electrolytes such as $LiPF_6$, $TEABF_4$ in acetonitrile, and $LiClO_4$ in ethylene carbonate has higher potential window up to 3.0 V. Ionic liquids, notably $[EMIM]BF_4$ and EMI TFSI also displays a noteworthy operating potential up to 3.0 V, making it suitable for higher voltage tolerance applications. Furthermore, it is observable from the table that the variations in operating potentials for the same electrolyte type reflect differences in experimental setups, electrode materials, and measurement techniques. Aqueous electrolytes remain to be an effective choice despite their relatively lower operating potentials due to their inherent advantages such as safety, low cost, environmental friendliness, and high ionic conductivity. The choice of electrolyte must be compatible with the testing material to ensure stable electrochemical performance. For instance, aqueous electrolytes are particularly well-suited for pseudocapacitive and battery-type materials that operate efficiently within narrower voltage windows. Ultimately, the synergy between electrolyte type and electrode material is critical in tailoring performance for specific energy storage systems.

Table 2.2
Operating potential of various types of electrolytes

Class	Electrolytes	Operating potential	Reported by
Aqueous	6 M KOH	1.0	(X. Wang *et al*., 2023)
	6 M KOH	0.8	(Jin *et al.*, 2023)
	6 M KOH	0.55	(Q. Liu *et al*., 2022)
	2 M KOH	0.5	(Karuppaiah *et al*., 2020)
	2 M KOH	0.7	(Z. Li *et al*., 2021)
	2 M KOH	0.9	(Acharya *et al*., 2021)
	1 M KOH	0.5	(Iqbal *et al*., 2019)
	1 M H_2SO_4	1.2	(Soundarya *et al*., 2023)
	1 M Na_2SO_4	0.6	(dos Santos Costa *et al*., 2023)
	1 M Na_2SO_4	2.0	(Haldar, 2021)
	0.5 M Na_2SO_4	2.0	(Grover *et al*., 2020)
Organic	(TEP)/ ($EMIMBF_4$)	2.5	(S. Li *et al.*, 2023)
	1M $LiPF_6$	1.0	(Ding *et al*., 2019)
	1 M $TEABF_4$ in ACN	1.8	(Banavath *et al.*, 2022)
	1 M of $LiClO_4$ in EC	3.0	(X. Li *et al*., 2018)
	$MeEt_3N$ BF_4	2.5	(X. Wang *et al*., 2023)
Ionic Liquid	[Emim] BF_4	2.5	(X. Wang *et al*., 2023)
	[Emim] BF_4	2.0	(B. Liu *et al*., 2023)
	EMI TFSI	3.0	(Moreno-Fernández *et al*., 2021)

TEP = triethyl phosphate
$EMIMBF_4$ = 1-butyl-3-methylimidazolium tetrafluoroborate
$LiPF_6$ = Lithium hexafluorophosphate
$TEABF_4$ = Tetraethylammonium tetrafluoroborate
ACN = acetonitrile

$LiClO_4$ = Lithium perchlorate
$MeEt_3N$ BF_4 = Triethyl methylammonium tetrafluoroborate
[Emim] BF_4 = 1-Ethyl-3-methylimidazolium tetrafluoroborate
EMI TFSI = 1-Ethyl-3-methylimidazolium bis (trifluoromethyl sulfonyl) imide

2.4 Recent Advances of Metal Oxide in Supercapacitor

Due to their redox properties, TMOs serve as promising electrode materials for supercapacitors, offering enhanced energy density and improved electrochemical stability. The distinct attributes of TMOs arise from their ability to exist in various oxidation states, facilitating rapid faradaic reactions. This characteristic allows them to seamlessly transition between different oxidation states during charge and discharge, facilitating swift entry and exit of electrolyte ions into the oxide lattice. This subchapter collectively discusses the previously reported work on various materials and the reasoning behind the material's potentiality in SCs. The detailed SCs properties in terms of Cs value, rate capability, energy density, and power density will be discussed under the performance of SCs subtopic.

2.4.1 Zinc Cobaltite and its Composites

$ZnCo_2O_4$ stands out as an economically advantageous binary transition metal oxide among its counterparts. In the quest for good-performing $ZnCo_2O_4$ electrode materials, researchers have endeavoured to produce $ZnCo_2O_4$ materials with diverse morphologies. Simultaneously, there is a need for the development of straightforward methods to facilitate cost-effective preparation. In the work of Mohamed *et al.*, (2017), nanosphere $ZnCo_2O_4$ with outstanding supercapacitive behaviour was effectively produced. A noteworthy Cs value as high as 1596 Fg^{-1} was acquired via a H_2O_2-urea-supported hydrothermal reaction without additional calcination step. As is known, the performance of supercapacitor electroactive materials relies significantly on the presence of a well-developed mesoporous structure (Guo *et al.*, 2019). Han and coworkers successfully procured $ZnCo_2O_4$ mesoporous microspheres prepared via solvothermal method followed by annealing treatment in air (Xingrong Han *et al.*, 2019). The porous structure not only allows excellent Cs value, but also remarkable long-term cycling stability. The performance is owing to the unique porous structure, thus offering an abundant active reaction site, facilitating swift ion and electron

transfer, and demonstrating commendable strain accommodation as well. Furthermore, a potential material for supercapacitor electrodes made of urchin-like mesoporous $ZnCo_2O_4$ microstructure was well-produced by H. Chen, *et al*., (2019). The synthesized material portrays an impressive 107.3% capacitance retention, implying an advantageous cycling stability and excellent reversible redox properties. In another work, Silambarasan *et al*., (2021) reported a slightly lower Cs but good capacity retention $ZnCo_2O_4$ nanostructure. On the side note, the work did not emphasize on the advantages of material porosity since the obtained morphology was an aggregated bundle-like nanostructures. In 2022, a study utilizing using a solvothermal approach with a mixed solvent system, $ZnCo_2O_4$ microstructures were synthesized in two distinct morphologies – porous polygonal microparticles (ZCO-EGD) and smooth polygonal microparticles (ZCO-EG). The porous architecture of ZCO-EGD provided a substantially higher effective SSA of 50.17 m^2/g compared to 38.14 m^2/g for the non-porous ZCO-EG variant. This surface area enhancement severely impacts the electrochemical performance, with ZCO-EGD displaying vastly superior output attributed to the increased SSA. In essence, precise tailoring of morphology during microparticle fabrication induces major differences in electrochemical activity, confirming the structure-property relationship where surface area is a key indicator of performance (Gedi *et al*., 2022).

Compositing $ZnCo_2O_4$ with other classes of material with the aim of improving the energy storage capability are also widely researched. For instance, multilayer graphene nanoplatelets/$ZnCo_2O_4$ (MGNs/$ZnCo_2O_4$) microspheres produced by B. Huang *et al*., (2021) and $ZnCo_2O_4$/CNT prepared by L. Wu *et al*., (2020). Both of these $ZnCo_2O_4$-carbon composites deliver excellent electrochemical performance. The notable supercapacitive ability of MGNs/$ZnCo_2O_4$ is leveraged from its spherical morphology and the incorporation of additional active sites through mesoporous construction for redox reactions (B. Huang *et al*., 2021). Likewise, the enhanced electrochemical behaviour possessed by $ZnCo_2O_4$/CNT is also associated with its morphological nature. The uniform integration of $ZnCo_2O_4$ micro flowers with CNT in the composite architecture induces synergistic effects for enhanced performance. Specifically, the highly conductive CNT network furnishes rapid electron transport pathways that are critical for efficient electrochemical reactions. Additionally, the

CNTs act as a versatile matrix reinforcing the mechanical stability of the $ZnCo_2O_4$ microflowers by absorbing stresses during repeated charge-discharge cycling. This robust composite nanostructure ensures a durable, integrated conduction network with maximized electrochemically active surface area. Consequently, the complementary attributes enable stable cycling along with fast electron transfer kinetics (L. Wu *et al*., 2020). In 2021, Wei *et al*., came up with an excellent idea of fabricating ultrathin nanosheets $ZnCo_2O_4$ on a carbon cloth (CC) substrate (referred to as ZCO/CC). ZCO/CC was fabricated through controlled electrochemical deposition using a bidirectional pulse current method within an organic system. This ZCO/CC architecture comprises congruent interfacing between the active nanosheets and conductive CC substrate. With an expansive SSA stemming from the nanoscale lateral dimensions, these conformal $ZnCo_2O_4$ nanosheets are enriched in exposed electrocatalytic active sites. Moreover, the ultrathin nature substantially curtails electron transmission distances, thereby accelerating charge transfer kinetics. Compared to conventional $ZnCo_2O_4$ nanostructures, these unique structural and interfacial attributes equip the as-developed ZCO/CC electrode with superior electrochemical activity emanating from the ultrathin nanosheets that enable maximized surface area-to-volume ratios (Wei *et al*., 2021). Further, a novel reduced graphene oxide (rGO)-encapsulated needle-shaped $ZnCo_2O_4$ nanocomposite ($ZnCo_2O_4$@rGO) was successfully fabricated using an accessible, affordable solvothermal method followed by thermal annealing (Naresh *et al*., 2023). The rationale behind the composite design was to leverage the conductive rGO sheets to closely wrap the $ZnCo_2O_4$ nanostructures. This construction induces multiple advantageous effects including - i) shortened diffusion paths that accelerate ion transport kinetics, ii) preclusion of $ZnCo_2O_4$ aggregation by physical separation for stable cycling, and iii) establishment of percolating electron-conducting networks via the highly conductive rGO matrix. Collectively, these attributes equipped the $ZnCo_2O_4$@rGO nanocomposite with excellent electrochemical properties (Naresh *et al*., 2023).

Another advanced material that incorporates polyaniline (PANi) into the zinc cobalt oxide-nitrogen doped graphene ($ZnCo_2O_4$@N-GO) composite led to significant improvements in supercapacitor performance (Kathalingam *et al*., 2020). Specifically,

the resulting $ZnCo_2O_4$@N-GO/PANi ternary composite exhibited an outstanding maximum specific capacitance approaching 720 Fg^{-1} at a scan rate of 10 mVs^{-1}. Moreover, even after 10,000 consecutive charge-discharge cycles, the capacitance retention remained remarkably high at 96.4%. These electrochemical enhancements are ascribed to the increased material porosity enabled by the PANi network. Given the simple and cost-effective fabrication methodology, this ternary composite demonstrates immense potential for next-generation supercapacitor devices with its superior capacitive performance combined with long-term cycling stability. In a study conducted by Faras *et al*., (2023), a binder-free 3D marigold flower-like $ZnCo_2O_4$ architectures on a conductive Ni foam substrate through a straightforward one-pot hydrothermal-assisted thermal annealing process was successfully procured. The marigold flower-shaped $ZnCo_2O_4$ nanostructures possess well-defined morphology and remarkable SSA. These traits synergistically equipped the material with excellent charge storage properties and kinetics. Also, the robust interfacial binding between the nanostructured $ZnCo_2O_4$ electrodes and the nickel foam current collector provides critical electrical contact. Consequently, the morphological appeal stemming from the tailored marigold structures coupled with facile charge transfer and collection induced by the strong substrate adhesion enables the demonstration of exceptional capacitive performance in terms of Cs value and energy density (Faras *et al*., 2023).

2.4.2 Nickel Cobaltite and its Composites

Numerous transition metal oxides have served as electrode materials for SCs. Notably, $NiCo_2O_4$ stands out as not just a cost-effective and eco-friendly choice but also boasts greater electronic conductivity and superior electrochemical performance compared to its counterparts: NiO and Co_3O_4. Akin to $ZnCo_2O_4$, the potentials of $NiCo_2O_4$ in SCs are worth acknowledging. In 2016, Zhang and coworkers had prepared a $NiCo_2O_4$ with various morphology such as nanopetal, nanosheet, nanoneedle, and nanorod arrays (Y. Zhang *et al*., 2016). Their work reveals the potentiality of $NiCo_2O_4$ in storing energy. Of the four electrode samples tested, the nanoneedle electrode demonstrated superior electrochemical performance compared to the rest. This optimal result highlights the nanoneedle sample as having the most propitious attributes, from both an electrochemical activity and efficiency standpoint,

out of all morphologies examined. In a different work, an urchin like $NiCo_2O_4$ microspheres was synthesized via hydrothermal route with subsequent annealing process, and its electrochemical behaviour was studied (Nayak *et al.*, 2020). This notable electrochemical performance is attributed to the high surface area stemming from the interconnected nanoporous network within each nanoneedle subunit. This nanoporous structure exists inside the larger, urchin-like microspheres that make up the nanoneedle morphology. In addition, another unique 3D miniature sea urchin-like $NiCo_2O_4$ with profound electrochemical performance was effectively synthesized by Q. Liu *et al.*, (2022). This work also claimed that the effective surface area affects the overall supercapacitive behaviour of $NiCo_2O_4$. Besides urchin-like morphology, flower-like $NiCo_2O_4$ was also reported to facilitate great SSA and allows effective electrolyte penetration (Kim *et al.*, 2018).

Combining transition metal oxides with carbon has been regarded as a suitable approach to enhance their electrochemical properties for supercapacitor applications. In 2015, a bimodal pore size distribution, consisting of small and large mesopores, characterized the growth of nickel cobaltite nanograss on different electrode substrates through a one-pot hydrothermal synthesis (M. S. Wu *et al.*, 2015). In this work, the nanograss morphology of the individual nanorods contains tiny pores smaller than 5 nm, which grant a high surface area for the material. Additionally, the larger vacant spaces between adjacent nanorods have pore sizes exceeding 20 nm. This dual nano- and mesoporous structure facilitates rapid electrolyte diffusion throughout the network via these large inter-rod pore channels, while maximizing surface area through the small nanopores within each rod. In another work, $NiCo_2O_4$-graphene quantum dots ($NiCo_2O_4$/GQDs) composite has been prepared by Kharangarh *et al.*, (2021) through hydrothermal method. The study concluded a strong interaction between $NiCo_2O_4$ and GQDs showcased a rapid reversible redox reaction and displays a significant Cs value. More importantly, the composed version of $NiCo_2O_4$ and GQDs exhibits better electrochemical properties compared to its single constituents.

Apart from $NiCo_2O_4$-carbon composites, metal doped $NiCo_2O_4$ were also commonly reported. For instance, Cu-doped $NiCo_2O_4$ nanosheets with inherent porosity were well-prepared by Han *et al.*, (2020). The doping effect brought about alterations in the electronic structure, leading to the formation of intrinsic porosities.

The doped sample retains approximately 94.6% after 3000 cycles, indicating favourable stability. Enhanced capacitive performance of $NiCo_2O_4$ was once again proven by aluminium (Al) doped approach. X. Chen *et al*., (2022) had evidently obtained nanosheet-wire structure composed of one-dimensional (1D) nanowires and two- dimensional (2D) ultrathin nanosheets. The synergistic integration of 1D nanowires and 2D nanosheets in the composite architecture offers complementary advantages. Specifically, the nanowires act as longitudinal highways to accelerate electron and ion transport kinetics courtesy of the continuous 1D conductive pathways. Meanwhile, the ultrathin 2D nanosheets expand the interface area to maximize exposure of catalytically active surface sites. Furthermore, theoretical simulations based on density functional theory (DFT) predict that doping the composite with Al can modulate the electronic band structure to significantly promote electrical conductivity. This multifaceted approach unlocks superior electrochemical properties.

2.4.3 Ternary Mixed Transition Metal Oxides and its Composites

Nowadays, ternary metal oxides comprising three distinct metal ions have garnered significant research attention over their single or binary counterparts. This is attributed to the synergistic interactions between the three metal species, which provide access to multiple oxidation states and significantly lower the activation energy barrier for electron transport. Consequently, ternary metal oxides boast improved electrical conductivity and ion diffusion kinetics. The cumulative impact of these favourable attributes leads to superior electrochemical properties including enhanced capacitance and higher charge-discharge rates compared to simpler transition metal oxides. Therefore, the intrinsic complexity engineered via compositional multiplicity makes ternary metal oxides promising candidates to push the forefront of electrochemical performance. For instance, Suganya *et al*., (2023) have worked on a facile synthesis of Ni-Mn-Zn oxide nanocomposites for hybrid supercapacitors. The prepared sample evidently manifests good Cs, notable energy density and longer discharge time. Another work by Malik *et al*., (2021) developed a Mn-Ni-Co MTMOs with a randomly arranged plant-like dendrites morphology. The findings of this work indicated that the fabricated material demonstrates promising supercapacitive performance, attributed to its well-organized morphology and the

synergistic contributions of its individual components. Furthermore, ternary $NiCoFeO_4$ nanorod is another example of synthesized MTMOs that can be utilized as active material for SCs electrodes (Faid & Ismail, 2019). Similar to most MTMOs, the reason behind the electrochemical potentiality is attributed to the hierarchical porosity of the nanorods architecture. Specifically, the porous nature facilitates efficient ion diffusion both within the inner regions of each nanorod as well as through the inter-rod void spaces. Furthermore, the ternary nickel cobalt iron oxide composition provides access to abundant redox states that promote surface electrochemical reactions. Collectively, these merits of structural porosity enhancing ion transport in tandem with compositional advantages of rich redox behaviour collaborate to unlock the superior capabilities (Faid & Ismail, 2019).

2.5 Application of Carbon in Supercapacitor

Carbon has received a considerable interest in SCs electrodes attributed to their substantial surface area, open porosity, impressive charge mobility, and robust mechanical strength. As part of ongoing endeavours to enhance device energy density, these carbon structures have been subject to a plethora of modifications (Yang *et al*., 2023). For instance, Recent advancements in engineered porous carbon electrodes have focused on strategic optimization across multiple techniques:

a) Tailoring pore architecture parameters including specific surface area and tuned pore size distributions to provide abundant charge storage sites while maximizing ion transport kinetics.
b) Sculpting novel carbon morphologies to induce advantageous effects regarding flexibility, accumulation behaviour and establishing integrated ion/electron pathways.
c) Surface functionalization via heteroatom doping using O, N, P and other dopants to improve hydrophilicity and introduce pseudo-capacitive redox reactions.
d) Decorating the carbon surface with pseudo-capacitive compounds like transition metal oxides/hydroxides to further amplify specific capacitance and energy density.

However, rationally synthesizing porous carbon electrodes that harmoniously

optimize pore structure, morphology, surface properties and pseudo-capacitive composition remains an outstanding challenge.

2.5.1 Graphene/Graphene Oxide/Reduced Graphene Oxide and its Composites

Recently, a binder-free electrode compositing graphene and PANI was effectively formulated via facile solution intercalation method (Thejas Prasannakumar *et al*., 2024). The exceptional electrochemical potential exhibited by the graphene/PANI electrode is achieved through the optimal amalgamation of both materials. Thejas Prasannakumar *et al*., stated that this combination effectively mitigates internal resistance and charge transfer resistance, fostering enhanced synergistic effects. Graphene acts as both a conductive agent and a supporting material, while PANI introduces pseudocapacitance, markedly elevating the electrochemical performance of the hybrid. Furthermore, graphene serves as a stable carbon framework, preventing the electrochemical dissolution of PANI through its elastic constraint. Another research performed by F. Zhu *et al*., (2024) in the fabrication of flexible reduced graphene oxide/polypyrrole nanotubes (rGO/PPy) films was reported. The comparison study of rGO/PPy and rGO film in terms of capacitance shows that the rGO/PPy films has greater capacitance than that of rGO and gradually increased with the increase in the amount of PPy nanotubes in the films. Subsequently, another advanced material incorporating N, S dual-doping porous Eucalyptus wood tar-based activated carbon aerogels (GDAC) was developed by Cheng *et al*., (2024). Like most carbon hybrid electrode materials, the reasoning behind the good electrochemical potential possessed by these materials can be credited to the hierarchical pore structure and impressive SSA features. This architecture provides more space and promotes ion diffusion within the electrolyte system. Additionally, Junchen Chen *et al*., created a composite graphene fibre by incorporating electrochemically exfoliated GO and chemically oxidized GO through a facile wet spinning route. The uniformly dispersed EGO in between the graphene sheet layers functioned as conductive fillers that boost the rate capability (Junchen Chen *et al*., 2023).

2.5.2 Carbon Nanotubes and its Composites

Despite being expensive and difficult to process, CNTs portray excellent characteristics that make them relevant in the realm of supercapacitors. CNTs exhibit a distinctive tubular nanostructure characterized by high electrical conductivity. Their combination of elevated SSA and robust mechanical strength renders them well-suited for serving as electrodes in supercapacitors, facilitating the attainment of both high capacitance and mechanical stability (Meena *et al*., 2023). CNTs paired with metal cobaltite shows good compatibility in delivering excellent energy storage capability. As an example, Isacfranklin *et al*., (2022) reported to enhance the Cs and stability of $ZnCo_2O_4$ by adding CNTs to make a composite material. Similarly, Nare and co-workers stated that combining $NiCo_2O_4$ and nitrogen doped CNTs makes a good composite with the ability to preserve approximately 99% of its initial capacitance upon 5000 cycles (Nare *et al*., 2024). In another work, Hadizadeh & Faraji, (2023) prepared leached graphite coin decorated with tungsten oxide nanoparticles and CNTs with high SSA and good mechanical strength. Moreover, the fabricated solid-state supercapacitor coin cell of these materials displays excellent electrochemical capabilities including a broad operating voltage window, high Cs, and long-term cycling stability. Such superior performance combined with the scalable manufacturability of the coin cell format pave the way towards translating lab-scale research to commercially viable large-scale fabrication of high-power supercapacitor devices. Hence, by leveraging simple, solution-based processing, this strategy is promising for enabling mass production of high-performance supercapacitor coin cells (Hadizadeh & Faraji, 2023). Further, Y. Xu *et al*., constructed a nitrogen, boron, and fluorine co-doped CNT which presented as NBF-CNT, grown on carbon cloth (CC). In this work, the electrochemical characterizations were directly employed NBF-CNT grown on CC as the electrode. The electrode displays excellent energy storage capability which benefited from: i) The binder-free direct growth of the CNTs on the current collector overcomes impedances tied to binder additions while maximizing utilization of the active material, and ii) multi-heteroatom doping of the CNTs induces synergistic effects that boost electrical conductivity via bandgap engineering and concurrently enhance hydrophilicity and surface redox activity (Y. Xu *et al*., 2023). Additionally, Shi *et al*., (2024) constructed an EDLCs type electrode material

composed of novel carbon aerogel doped with activated short multi-walled carbon nanotube (CA/AMWCNT composite aerogel). The work is focusing on studying the effects of AMWCNT addition into CA, in terms of changes in morphological and electrochemical properties. As a result, with a suitable amount of AMWCNT addition, enhancements in SSA, pore diameter, and pore volume are observed.

2.5.3 Graphene Nanoplatelets and its Composites

In terms of cost effectiveness, compared to other nanocarbons for instance CNTs, GNPs can be produced at relatively lower cost in bulk quantities. Moreover, the platelet morphology with thin sheets stacked together provides more conductive pathways between sheets, thus reducing the electron transport resistance between layers. In 2020, Ag-tuned AgCo (Ag@Co) 3D hierarchical network structures encapsulated in C, N, and S-tri-doped layers (CNS@$Ag_{0.5}$@Co) were well manufactured by Y. Li *et al*., (2020). Subsequently, CNS@$Ag_{0.5}$@Co was subjected to GNPs-hybridization with the aim to obtain a new novel composite that works effectively as electrode material for SCs. The CNS@$Ag_{0.5}$@Co-180-10/GNPs nanocomposite exhibits exceptional electrochemical performance due to the combined beneficial effects of its multiple components. Specifically, the nanocomposite has a large SSA, suitable mesopore porosity, and an excellent hierarchical conductive network interconnected throughout its structure, leading to outstanding electrochemical capabilities (Y. Li *et al*., 2020). In 2021, Indium (III) oxide (In_2O_3) nanoparticles with incorporation of GNPs were successfully prepared by Jabeen and team. The effect of various GNPs addition percentage (10%, 30%, 50%, 80% and 100%) was studied in this work. The results proposed that 30% addition of GNPs shows the highest capacitance and has a better chance to be SCs electrode material (Jabeen *et al*., 2021). Another study conducted by Polat & Faris, (2022) reveals the electrochemical potentials of copper ferrite ($CuFe_2O_4$) combined with graphitic carbon nitride (g-C_3N_4) and GNPs on Ni foam surface. The CV measurements indicated the occurrence of redox peaks for Cu^{+2}/Cu^{+1} and Fe^{+3}/Fe^{+2}, with a predominantly diffusion-controlled charging mechanism. Moreover, GCD measurements revealed that the electrode exhibited a characteristic battery-type loop. Also, the capacitance of $CuFe_2O_4$ enhanced by 87% and 116% with the addition of g-C_3N_4 and GNPs,

respectively in a separate system. Evidently, GNPs shows apparent effects towards the overall energy storage capability of $CuFe_2O_4$. Further, another spinel ferrite-GNPs combination was reported by Mashrah & Polat, (2023). Herein, the effect of GNPs attachment with magnesium ferrite ($MgFe_2O_4$) was examined with the material being synthesized directly on the surface of nickel foam. The interaction of $MgFe_2O_4$ and GNPs give off a distinctive electrochemical behaviour owing to oxidation/reduction reaction on the nickel foam surface coupled with the synergistic effects of the individual component.

2.6 Synthesis Approach of MTMO-Based Electrode Material

Various methods, such as electrodeposition, chemical reduction, atomic layer deposition, hydrothermal, and sol-gel method have been developed to prepare high pseudocapacitive performance MTMOs nanocomposites. As summarized in Table 2.3, MTMOs-based material undergoes a different synthesis route in accordance with the end-product target.

2.6.1 Electrodeposition Technique

Electrodeposition allows uniform and controllable coatings onto conductive substrates, ensuring homogeneous distribution of carbon nanomaterials in the metal matrix. For instance, layer by layer deposition technique was utilized to deposit the S-SnO_2 nanoparticles on a rough and compact film of RuO_2/BCC. In the experiment described here, the electrodeposition was carried out in a three-electrode configuration with BCC acting as the working electrode, exposing 1 cm^2 area. A platinum mesh of dimensions 2 cm x 2 cm served as the counter electrode while a double junction Ag/AgCl electrode provided the reference potential. To ensure a uniform RuO_2 coating on the BCC substrate is achieved, a constant current density in the range of 5 mA/cm^2 to 35 mA/cm^2 was supplied for a duration of 30 minutes. Morphologically, RuO_2/BCC shows a rough and dense RuO_2 coating on the BCC substrate. Moreover, the cross-sectional imaging revealed that the BCC had a thickness of approximately 303 μm, while the electrodeposited RuO2 film was about 2.29 μm thick (Mevada & Mukhopadhyay, 2020).

Deposition technique is suitable for thin film samples while methods like chemical reduction, solvothermal, hydrothermal, and sol-gel hydrothermal route are appropriate for powder and solution-type samples. This technique, followed by thermal treatment was employed by Orhan *et al*., (2023) in which cobalt chromite ($CoCr_2O_4$)/electro-reduced graphene oxide (ERGO) (CCO/ERGO) nanocomposites were successfully prepared. The setup involved a three-electrode cell with nickel foam working electrode, Pt wire counter electrode and Ag/AgCl reference electrode. The deposition solution consisted of 5 mM cobalt nitrate hexahydrate (Co $(NO_3)_2 \cdot 6H_2O$), 10 mM chromium nitrate nonahydrate (Cr $(NO_3)_3 \cdot 9H_2O$), and 0.1 mg/mL graphene oxide suspension dissolved in 0.1 M KNO_3. The deposition potential was determined to be -1.4 V by cyclic voltammetry in the precursor mixture. In this work, nickel foam surface was coated with cobalt and chromium hydroxide composites by electrochemically reducing the nitrate precursors for 0.5 hours, allowing precise control over the deposition. The coated electrode was then annealed at 500°C for 1 hour under nitrogen gas. This thermal treatment converts the amorphous hydroxide structures into crystalline cobalt chromite (CCO) while retaining the ERGO component. After slowly cooling the annealed electrode to room temperature, the final CCO/ERGO nanocomposite electrodes were successfully obtained on the conductive nickel foam surface.

Recently, Zhang *et al*., (2023) reported an electrodeposition-derived reduced graphdiyne oxide/$NiCo_2S_4$ hierarchical nanosheet array (r-GDYO/$NiCo_2S_4$) electrodes. The electrodeposition progressed in a typical three-electrode system setup consisting of $NiCo_2S_4$ working electrode, platinum plate counter electrode and saturated calomel electrode as the reference. The electrolyte used is 0.2 mg/mL GDYO, and a multi-potential step method was used for the electrodeposition. The deposition potential was set at -1.2 V vs Ag/AgCl reference electrode, and the deposition time was 5 minutes to synthesize the composite r-GDYO/$NiCo_2S_4$ material (Zhang *et al*., 2023).

2.6.2 Solvothermal and Hydrothermal Method

Another popular synthesis methods are solvothermal and hydrothermal. Solvothermal method is a variation of the hydrothermal method, where the synthesis is carried out in a solvent rather than water. Like solvothermal, the hydrothermal

method is known to have sets of advantages including low operating temperature, easy operation, and simple instrumentation (Dhas *et al*., 2021). Moreover, it also facilitates uniform nucleation and growth of the materials which are beneficial for ensuring long-term cyclic stability properties of the electrode material. The versatility of this method has also been reported to give a noteworthy effect on the properties of the synthesized dimensional hierarchical porous carbon (3D-HPCs) (H. Li *et al*., 2021). Where, the properties of the final product can be tailored via tuning the hydrothermal processing parameters. Another work reported by L. Huang *et al*., (2022) proposed the same facile hydrothermal method which resulted in a greater surface area, improved electrical conductivity, as well as its electrochemical performance.

In a typical hydrothermal route, it commonly involves homogeneous mixing of precursors, hydrothermal processing under pressure at elevated temperatures, and post-treatment to develop required properties. For metal composites, the most common precursors used are nitrates, chlorides, and acetates. For instance, a work led by Mashrah & Polat uses Fe_3Cl and $MgCl_2 \cdot 6H_2O$ as the metal source compounds for hydrothermal synthesis because of their good water solubility and lack of secondary phase formation. The hydrothermal technique was selected as an accessible, low-cost, and low-temperature route to synthesize the target compound. The key parameters controlling particle size in hydrothermal reactions are temperature, duration, and precursor concentration. By optimizing these conditions, this single-step hydrothermal approach provides a simple yet effective method to synthesize the desired material. The compounds' aqueous solubility and thermal stability facilitate homogeneous nucleation and controlled growth of the product crystals, avoiding unwanted secondary species. Overall, the judicious choice of metal salts combined with appropriately tailored hydrothermal parameters enables precise size and compositional control in synthesizing the target compound (Mashrah & Polat, 2023).

2.6.3 Sol-gel Method

Apart from solvothermal and hydrothermal, another synthesis method for producing versatile compositions is sol-gel method, as illustrated in figure 2.5. It allows production of a wide range of single, double, and triple metal composites with tailored ratios. Key advantages that make sol-gel attractive include economical

precursor materials and straightforward processing resulting in overall lower manufacturing costs compared to alternate methods (Bokov *et al*., 2021). The sol-gel technique provides a simple route for synthesizing uniformly dispersed powders with excellent control over composition at mild temperatures (Jittiarporn *et al*., 2017). The basic preparation only involves mixing and reacting metal salts in solution without complex equipment (T. Huang *et al*., 2021). In general, the sol-gel process relies on two reactions involving hydrolysis and condensation of a molecular compound, to produce a solid material under gentle conditions. There are two primary chemical methods employed currently: 1) The metal-organic path, involving metal alkoxide compounds dissolved in organic solutions which then undergo controlled reactions, 2) The inorganic path, using aqueous solutions of metal salts like chlorides, nitrates, and sulphides which follow reaction conditions favouring eventual production of a solid phase end-product (Jittiarporn *et al*., 2017). Moreover, the porosity of the prepared materials is tuneable by imposing variations in the drying and sintering process. In 2020, Uke *et al*., (2020) employed a sol-gel citrate method for the synthesis of $MgFe_2O_4$ nanocrystals doped with Zn. The obtained product is composed of spherical grains with sizes varying between 50 and 100 nm. The presence of mesopores facilitates substantial channels for the bulk flow of electrolytic fluid. In the following year, T. Huang *et al*., yielded a hierarchical porous $CoFe_2O_4$ prepared via citric acid-assisted sol-gel auto-combustion method. The study highlighted the advantages of using the sol-gel auto combustion method including its ease of preparation steps, cost-effectiveness, and easy control of the stoichiometric ratio (T. Huang *et al*., 2021). Furthermore, mixing in liquid phase processing promotes homogeneous distribution of components, even at nanoscale. By avoiding prolonged exposure to extreme temperatures, uniform dispersion can be maintained while inhibiting segregation. The relatively low temperatures employed also facilitate large-scale production. In summary, the sol-gel approach enables affordable and reliable synthesis of tailored powders with precision over the composition and particle characteristics. The scarcity of study on the effects of sol-gel technique on the performance of PCs electrodes quickly became one of the motivations that triggered this study. Hence, this specific study will focus on the influence of the aforesaid method on the performance of PCs electrode material.

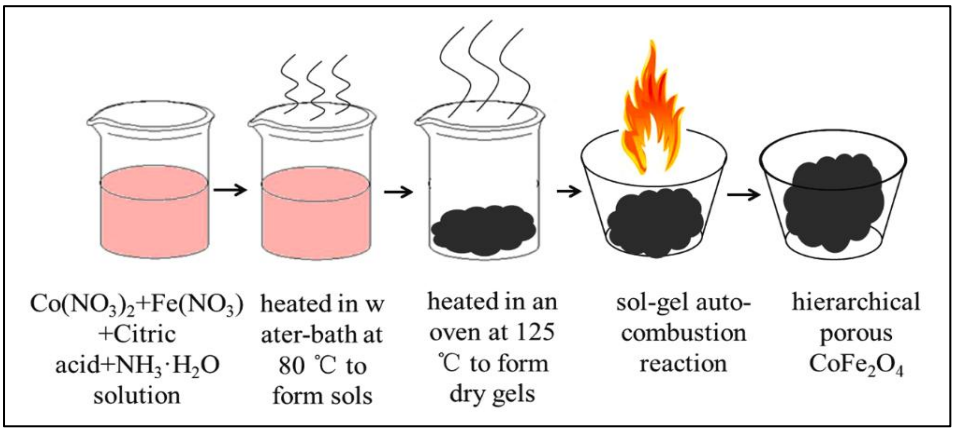

Figure 2.5 Schematic representation of the citric acid-assisted sol-gel auto-combustion synthesis of $CoFe_2O_4$ (T. Huang *et al*., 2021)

Table 2.3
Synthesis method of preparing metal-based nanocomposites in previous reported studies.

Material	*Synthesis method*	*Conditions*	*Morphology*	*Reported by*
S-SnO_2 NPs-RuO_2@BCC	Electrodeposition followed by spin coating	Use three-electrode system consists of BCC as the working electrode, platinum mesh as counter electrode and double junction Ag/AgCl reference electrode.	nanosphere	(Mevada & Mukhopadhyay, 2020)
($CoCr_2O_4$)/electro-reduced graphene oxide (ERGO)	Electrodeposition followed by thermal treatment	three-electrode cell with nickel foam working electrode, Pt wire counter electrode and Ag/AgCl reference electrode.	narrow size distribution with smaller nanoparticles.	(Orhan *et al.*, 2023)
r-GDYO/$NiCo_2S_4$	Electrodeposition and hydrothermal method	Use three-electrode system setup consisted of $NiCo_2S_4$ working electrode, platinum plate counter electrode and saturated calomel electrode as the reference.	$NiCo_2S_4$ nanosheets are hexagonal and cross-linked to each other and grow uniformly on the surface of the carbon cloth	(Zhang *et al.*, 2023)
Co–B@GO	Chemical reduction approach	The chemical reduction reaction was carried out by adding borohydride solution	crumpled layered structure with several stacking layers GO, spherical	(Wei Zhang *et al.*, 2017)

			particles Co-B	
Zn/Ni-MOF/rGO	Solvothermal	Kept in Teflon-lined stainless steel and heated at 120 ˚C for 12 h. Then, precipitate vacuum dried at 100 ˚C for 12 h.	MOF microspheres and rGO flakes	(Jin *et al*., 2023)
ZnO nanomembranes	Atomic layer deposition	A typical ALD sequence enclosed the following: DEZ pulse (30 ms), waiting time (2 s), N_2 purge (20 s), DIW pulse (20 ms), waiting time (2 s), and N_2 purge (20 s)	ultra-thin nature with folded edges, ripples, and curls.	(Naeem *et al.*, 2020)
CoO–ZnO/rGO	Hydrothermal and subsequent annealing treatment	heated to 400 °C under a nitrogen atmosphere with a heating rate 5 °C/min, and then kept heating at 400 °C for 2 h	clustered nanowires like chrysanthemums	(M. Xu *et al*., 2020)
GNPs doped $MgFe_2O_4$	Hydrothermal	Heated at 130 ˚C for 6 h	-	(Mashrah & Polat, 2023)
Zn-Ni-Co	Hydrothermal	Zn, Ni, and Co salts were mixed and heated at 120 ℃ for 5 h, followed by calcination at 350 ˚C for 2 h in a muffle furnace to obtain ZNCO.	urchin-like, flaky ZNCO microspheres	(L. Huang *et al*., 2022)
Zn doped $MgFe_2O_4$	Sol-gel	Stir at 80 ˚C for 3 h, heated on	Spherical grain, 50 to 100	(Uke *et al.*, 2020)

		pressure bomb at 120 ˚C for 12 h, then calcined 550 ℃ up to 6 h	nm	
$CoFe_2O_4$	Sol-gel auto combustion	heated in water-bath at 80 °C for 2 h to form sols, heated 125 °C for 12 h to form dry gels, then calcined under air atmosphere at 350 °C for 6 h.	hierarchical porous features	(T. Huang *et al*., 2021)
ZnO/graphene		Substrate cured at 120 ℃ for 1 min, repeated 20 times. Then, annealed at 500 °C for 1 h	-	(Gu *et al*., 2017)

S = Tin
SnO_2 = Tin Oxide
RuO_2 = Ruthenium Oxide
BCC = bare carbon cloth
Co = Cobalt
B = Boron
GO = reduced graphene oxide
ZnO = Zinc Oxide
Ni = Nickel

2.7 Critical Parameters Influencing the Supercapacitor Performance

A typical supercapacitor performance evaluation is often carried out via three-electrode configuration. Electrochemical characterization such as cyclic voltammetry (CV) and galvanostatic charge discharge (GCD) test enables the discovery of specific capacitance (Cs), energy density and power density. For instance, a typical setup with a glassy carbon electrode (GCE) serves as a working electrode, Ag/AgCl as reference electrode and platinum wire works as a counter electrode, as displayed in Figure 2.6.

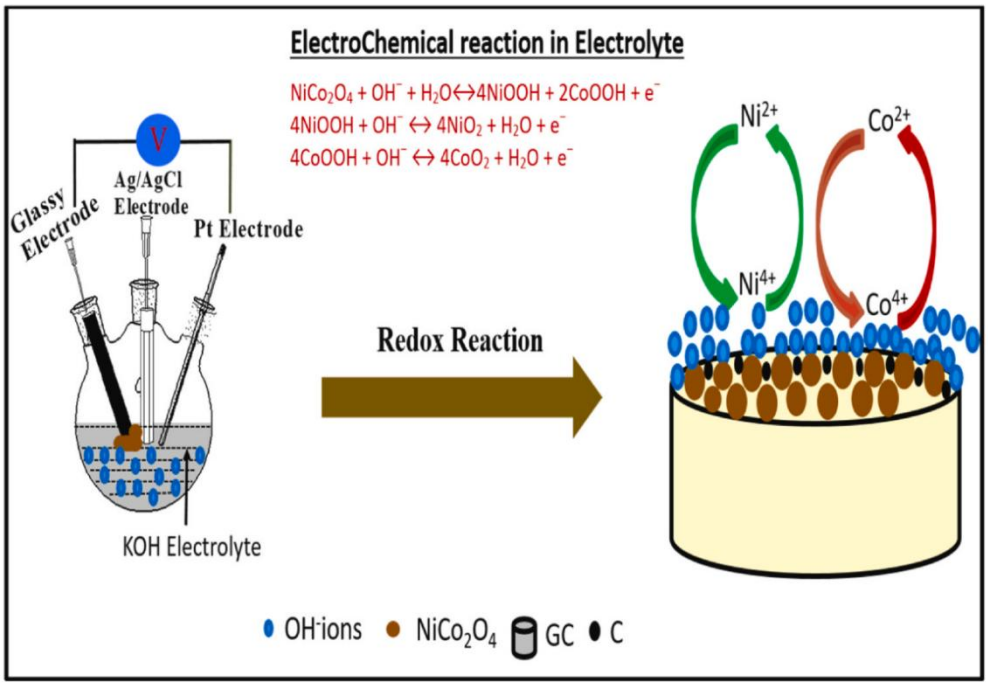

Figure 2.6 Schematic Diagram for the redox behaviour during electrochemical reaction of $NiCo_2O_4$/GQDs composite (Kharangarh *et al.*, 2021)

2.7.1 Specific Capacitance

Generally, the performance of SCs is evaluated based on the Cs value, energy and power density and its electrochemical stability upon being subjected to repeated charging-discharging cycles. The following sub-chapter will highlight on the SCs performance properties that have significant effect towards how the device is rated. Cs is a very important characteristic that needs to be studied when working with SCs. It can be termed as the ability of a body to store electrical charges or energy. The Cs values for every material are mainly depending on the pore volume and size, as well

as the surface area of the material (Da Silva *et al*., 2019). Thus, it is favourable to use the material with high surface area as the electrode material for SCs. In SCs, the Cs value may vary depending on the mass or area of the active material, the scan rate value, the current density value, potential window, and the conductivity of electrolyte used. These factors will diversify the output electrochemical performance of each tested sample. As it is mentioned, the effect of the parameters on the value of Cs is proved by Equation (2.1) when utilizing CV analysis, while Equation (2.2) for the case of using GCD method.

$$C_s = \frac{\int_{V_a}^{V_c} I\ (V)dv}{Vm\ (V_c - V_a)} \tag{2.1}$$

$$C_s = \frac{I \times \Delta t}{\Delta v \times m} \tag{2.2}$$

Where Cs representing the specific capacitance (Fg^{-1}), Vc and Va are the potential window (V), $I(V)$ is the response-current (A), v is the potential scan rates (mVs^{-1}), Δt in seconds represent the time for one sweep segment and m as the mass of the active material (g).

Table 2.4 and 2.5 summarizes the electrochemical performance of various metal-based electrode materials reported in previous research. It was found that the Cs values for composite samples varies from 250 – 1950 F/g at various current densities. The obtained Cs values are often associated with the conductivity and types of the electrolyte and the scan rate used. A more conductive electrolyte allows more electrons to be transferred to the surface of the material, hence contributing to higher Cs value. The vital effect of morphology in the Cs value of SCs material is also highlighted in table 2.4, wherein different ZnO morphologies shows varied Cs values. For instance, hexagonal cup-shaped ZnO exhibits the highest specific capacitance (6.4 Fg^{-1}), followed by nano assemblies (5.75 F g^{-1}), nanorods (4.03 F g^{-1}), and nanospheres (3.67 Fg^{-1}), all tested at the same scan rate of 10 mV s^{-1}. Hexagonal cup-shaped and nano assemblies shapes are likely to have a greater SSA and more porous structures compared to the other morphologies, thus leading to a higher Cs value. The Hexagonal cup-shaped ZnO is typically an open, hollow structure that tends to provide more available sites for the electrolyte's interaction. On the other hand, nano

assemblies often referring to a hierarchical, aggregated structures that made up from smaller units which can produce internal voids and pathways that leads to an improves ion diffusion. In contrast, closed structures like nanorods and nanosphere offer less available sites for electrolyte interaction, thereby reducing the Cs value.

Table 2.4 and 2.5 also presents a comparative analysis of various ZnO-based and transition metal-based electrode materials in terms of their specific capacitance, energy and power densities, and electrochemical stability. Among the listed materials, NiCo-SOH on nickel foam exhibits the highest specific capacitance (2092.7 F g^{-1} at 1 A g^{-1}) with excellent cycling stability (98% retention after 9000 cycles), indicating its strong electrochemical performance. Zn–Ni–Co on Ni foam also demonstrates high capacitance (1837 F g^{-1} at 2 A g^{-1}) and good stability (82% after 10,000 cycles), along with a power density of 824.5 W kg^{-1}. Co–Ni–ZnO@$NiWO_4$, despite its moderate capacitance (229.7 F g^{-1}), offers a notably high energy density (81.6 Wh kg^{-1}) and strong capacity retention (93.1% over 10,000 cycles), suggesting its potential for high-energy applications. Copper-doped cobalt manganese phosphate achieves a balance between high energy density (56 Wh kg^{-1}), strong power density (800 W kg^{-1}), and excellent cycle stability (97.2% after 2000 cycles). In contrast, ZnO/CeO_2 and Ni–Zn–Co shows comparatively lower specific capacitances (1069 and 776 F g^{-1}, respectively) but maintain reasonable energy densities (39.6 and 44.5 Wh kg^{-1}). Overall, the data emphasize the significance of material composition and structural design in achieving optimal supercapacitor performance, with nickel foam-supported and multi-metallic systems showing superior electrochemical behaviour.

2.7.2 Energy and Power Density

The amount of previously reported energy and power density performance of electrode materials seem trivial and lack attention. Despite its importance, the energy and power density performance of SCs electrode material has remained understudied. In a study reported by Shin & Shin (2021), NiO/C@CNF sample shows a noteworthy output performance up to 58.43 Wh/kg and 1947 W/kg energy and power density values, respectively. As can be seen in table 2.1, a study conducted by Xu *et al.*, 2020 provides another successful example of using pseudocapacitive materials. In this study, CoO-ZnO/rGo supported Nickel foam samples evidently proves a high energy density

up to 45.9 Wh/kg and power density of 800 W/kg can be delivered through this combination. In general, the performance indicator including Cs, energy and power density value can be tailored to its ideal values if the factors that contribute to the increase of SCs performance is identified. Table 2.6 presents the contributing factors that have a significant effect on the specific capacitance performance of a material. Several factors have been associated with the escalation of the Cs values, energy, and power density, which includes the active surface area, surface affinity, doping process, metallic structure generation, porosity, and the availability of oxygenated functional groups on the surface of the material. By tuning the aforementioned factors, the easiness of ion transportation and augmented storage ability can be promoted, hence, improving the overall performance of the supercapacitor.

2.7.3 Equivalent Series Resistance

The SCs voltage is made up of two components - a capacitive component and a resistive component. The capacitive component represents the voltage changes that occur due to the charging and discharging of SCs. These voltage changes are caused by the accumulation and depletion of electric charge in the SCs. The resistive component represents the voltage drop that occurs due to the equivalent series resistance (ESR) of the SCs. The ESR causes an internal resistance to current flow during charge and discharge, resulting in an internal voltage drop. Therefore, the resistive voltage component accounts for the internal losses due to the ESR, while the capacitive component accounts for ideal voltage changes from charge accumulation and release. Together, these two components make up the total voltage across the SCs (Gautham Prasad *et al*., 2019).

ESR can be measured in two ways. First, it can be measured directly as the impedance at the resonant frequency of the supercapacitor. Second, it can be calculated from the AC impedance measured at a specific frequency. Hence, ESR is determined either from the impedance at resonance or from an impedance calculation using an AC measurement at a chosen frequency. But in both cases, the cell construction and physical dimensions directly impact the internal resistance represented by the ESR. In addition, ESR has contributions from both ionic and electronic components. The ionic component comes from the inherent inertia of ion

movement as well as the conductivity of the electrolyte and any impurities present. The electronic component arises from the natural resistance of the electrode materials and connections as well as the contact resistance between carbon particles. Specifically, factors like the resistivity of the conductors, the ohmic resistance, and the size and connectivity of carbon particles determine the electronic resistance. The ionic resistance relates to the mobility and transport rates of the electrolyte ions.

In addition to intrinsic factors like the electrodes, electrolyte properties, surface traits, and structural packing, the manufacturing processes used by different manufacturing companies' impact ESR. Each supercapacitor manufacturer has proprietary fabrication techniques developed through experience. They keep these techniques confidential to maintain a competitive advantage in the market (Yassine & Fabris, 2017). Consequently, advancements in lab-scale research do not always translate directly to commercial production. The specific methods used to construct a supercapacitor at an industrial scale play an equally important role in determining its achievable ESR performance.

2.7.4 Cycle life and electrochemical stability

Apart from enhancing the energy and power densities of energy storage systems, another key factor in meeting the demand for cutting-edge electronic devices is long cycle life. Optimizing these Metrics in energy storage is vital for enabling the next generation of electronics. Cycle life refers to how many charge/discharges cycles the SCs can undergo before there is a degradation in performance. A longer cycle life means the SCs have better durability and can undergo more charging/discharging without capacity or power fade over time. This is important for applications that require frequent energy delivery and storage. On the other hand, electrochemical Stability indicates the ability of the electrode materials and electrolyte to withstand electrochemical reactions without significant structural or chemical changes when charged/discharged. Higher electrochemical stability depicts the ability of SCs to operate at higher voltages without compromising its performance. It is of vital importance because the energy density of a supercapacitor depends on the operating voltage squared. Higher stability enables higher usable voltages.

Shin & Shin (2021) and Mevada & Mukhopadhyay (2020) reported an

approximate electrochemical stability upon 5000 charge/discharge cycles (also presented in Table 2.5). Both studies reported a metal oxide-carbon hybrid composites that involves the synergistic effect of high theoretical capacity metal oxides and high conductivity and surface area of carbon materials. This then allows an enhancement of electron transport and electrochemically surface interactions. Additionally, nanostructured carbons can mechanically buffer the metal oxides through composite formation, accommodating stresses and preventing aggregations to occur. This leads to stabilized SEI layer formation and resolves interfacial issues (Yang *et al*., 2019). Together, these synergistic mechanisms between the constituents result in increased cycling stability, higher achievable voltages and charge rates, and longer usable lifetimes compared to its single component.

An outstanding electrochemical stability can be seen on active carbon cloth (AECC) reported by Su *et al*., (2024). Benefiting from the rich-functional group properties, it delivers excellent cyclic stability of 100 % after 10,000 cycles at 16 mA cm^{-2} . The oxygen functional groups present on the surface may contribute extra pseudocapacitance. Moreover, the core-shell architectures and abundant pore volume facilitate the penetration of electrolyte into the interior carbon fibre pores. This allows efficient access to the high surface area interior, reducing internal resistance and charge transfer impedance, hence contributing to an excellent electrochemical stability.

Table 2.4
The electrochemical performance of various transition metal electrode materials.

Material	Specific Capacitance/Areal Capacitance	Energy Density (Wh kg^{-1})	Power Density (W kg^{-1})	Electrochemical Stability/capacity retention	Reported by
Hexagonal cup shaped ZnO	6.4 Fg^{-1} at 10 mVs^{-1}	N/A	N/A	N/A	(Murali *et al*., 2020)
ZnO (nanoassemblies)	5.75 Fg^{-1} at 10 mVs^{-1}				
ZnO (nanorod)	4.03 Fg^{-1} at 10 mVs^{-1}				
ZnO (nanosphere)	3.67 Fg^{-1} at 10 mVs^{-1}				
ZnO/CeO_2	1069 Fg^{-1} at 5 mVs^{-1}	39.6 Wh kg^{-1}	N/A	N/A	(Arunpandiyan *et al*., 2020)
Ni-Zn-Co	776 Fg^{-1} at 2 Ag^{-1}	44.5 Wh kg^{-1}	880 W kg^{-1}	88.9% after 10000 cycles	(W. Hu *et al*., 2017)
NiCo-SOH on nickel foam (NF)	2092.7 Fg^{-1} at 1 Ag^{-1}	34.3 Wh kg^{-1}	N/A	98% after 9000 cycles	(Pu *et al.*, 2021)
Zn-Ni-Co on Ni foam	1837 F g^{-1} at 1 Ag^{-1}	41 Wh kg^{-1}	824.5 W kg^{-1}	82% after 10,000 cycles	(Ali *et al.*, 2021)
Co–Ni–Zn O@NiWO4	229.7 F g^{-1} at 0.5 Ag^{-1}	81.6 Wh kg^{-1}	N/A	93.1% up to 10,000 cycles	(Kumar *et al.*, 2019)
Copper doped cobalt manganese phosphate	498.2 at 3 mV/s	56 Wh kg^{-1}	800 W kg^{-1}	97.2% after 2000 cycles	(Iqbal *et al*., 2021)

Table 2.5
The electrochemical performance of transition metal oxides-carbon material

Material	Specific Capacitance/Areal Capacitance	Energy Density (Wh kg^{-1})	Power Density (W kg^{-1})	Electrochemical Stability/capacity retention	Reported by
Amorphous Cobalt Boron Alloy@Graphene Oxide	460 Fg^{-1} at 1 Ag^{-1}	N/A	N/A	84% after 1000 cycles at 10 mVs^{-1}	(Wei Zhang *et al.*, 2017)
ZnO/carbon hybrids	145 Fg^{-1} at 2 mVs^{-1}	N/A	N/A	91% after 10000 cycles at 2 mVs^{-1}	(Y. Zhao *et al*., 2018)
CoO–ZnO/rGO supported on Ni foam	1951.8 F/g at 1 Ag^{-1}	45.9 Wh kg^{-1}	800 W kg^{-1}	90.1% after 5,000 cycles	(M. Xu *et al*., 2020)
NiO/C@CNF composite	742.2 Fg^{-1} at 1 Ag^{-1}	58.43 Wh kg^{-1}	1,947 W kg^{-1}	88% after 5000 cycles	(Shin & Shin, 2021)
S-SnO_2NPs-RuO_2@BCC	794 $mFc^{-1}m^{-2}$ at 5 mVs^{-1}	N/A	N/A	87.5 % after 5000 cycles	(Mevada & Mukhopadhyay, 2020)
$RuNi_2O_4$/rGO	792 F g^{-1} at 1 Ag^{-1}	110 Wh kg^{-1}	500 W kg^{-1}	93% after 10,000 cycles	(Bera *et al*., 2022)

Ni-Zn hydroxide/rGO	615.4 Fg^{-1} at 1 Ag^{-1}	53.7 Wh kg^{-1}	825.1 W kg^{-1}	87.5% after 8000 cycles	(Du *et al.*, 2021)

Table 2.6
The contributing factors that affect the supercapacitive performance of a material

Factors	Reported by
Large effective area for ion transport and energy storage	(Ramanathan *et al*., 2021)
Swift ion diffusion in electrolyte and the effective adsorption onto the electrode surface	(Ezeigwe *et al*., 2020)
Favourable charge-transfer kinetics and much faster electron transport	(Ezeigwe *et al*., 2020)
Increase in surface affinity enhances electrolyte/electrode interactions and electrolyte wettability	(Ezeigwe *et al*., 2020)
Appropriate doping amount and surface-driven behaviour contribution rate	(H. Liu *et al*., 2019)
Defect engineering, metallic structure generation, and heteroatom doping	(R. Liu *et al*., 2021)
Modified pore structure or combined oxygenated groups to improve wettability of materials	(X. Zhao *et al*., 2020)

2.7.5 Supercapacitor Self-Discharge Rate

Supercapacitor tends to self-discharge, which can be observed as a gradual voltage drop over time, when it is left under open-circuit condition. This creates a significant gap between laboratory research and practical applications. Self-discharge has always been one of the major limitations in the performance of supercapacitors and is typically observed as a gradual decline in voltage over time after the device has been charged (Helseth, 2021). This behaviour is often associated to several mechanisms, inclusive of internal charge redistribution along the electrode surface, redox reactions at the electrode–electrolyte interface, as well as leakage current. While eliminating self-discharge phenomenon completely remains beyond our reach, it is both possible and feasible to minimize this rate to its lowest practical level, thereby enhancing the viability of supercapacitors for real-world implementation. To address this issue, various strategies has been employed by the supercapacitor community.

For instance, incorporating blocking layers on carbon electrodes has been shown to reduce self-discharge. However, this caused a drawback of decreasing the capacitance and the storage capability of a supercapacitor's material. Apart from that, another factor affecting the se-lf-discharge behaviour is by tuning the surface chemistry of carbon material, though the underlying processes are not yet fully discovered. Despite being a drawback, compared to more traditional approaches such as potential floating, self-discharge also offers diagnostic potential and has been reported to provide faster insight into device stability, particularly in systems that employs ionic liquids.

When voltage levels fall to half their initial value, supercapacitors become virtually ineffective, as this initial 50% voltage threshold contains approximately 75% of the device's stored energy (Liu *et al.*, 2021). Current scientific consensus recognizes three predominant self-discharge mechanisms which inclusive of leakage current, faradaic reactions, and charge redistribution. Leakage current predominantly cause by two factors which are parasitic redox reactions near the interface between electrode and electrolyte and the internal short-circuit occurred during the supercapacitor assembly process. The relationship between the self-discharge voltage (V) of supercapacitors and the duration of self-discharge (t) is presented in Equation (2.3):

$$\frac{V}{V_i} = \exp\left(\frac{t}{RC}\right) \tag{2.3}$$

Where V_i is the steady voltage value at the beginning of the self-discharge, C represents the capacitance, while R is the ohmic load resistance.

Faradaic reaction is the reaction that is associated with the electrochemical reactions occurred between the oxygen-containing functional groups and redox mediators present in redox-active electrolytes. Faradaic reaction is reportedly having a significant effect towards accelerating the self-discharge rates, particularly in EDLC system. The electron transfer processes promote the self-discharge rate, consequently diminishing the supercapacitor's voltage retention capacity. Faradaic reaction can typically be categorized into two distinct mechanisms based on reactant species concentration: activation-controlled and diffusion-controlled reactions. When reactant species exist at sufficiently high concentrations, their concentration gradient exerts

negligible influence on the Faradaic reaction rate. Consequently, the self-discharge phenomenon induced by Faradaic reactions becomes predominantly governed by activation-controlled kinetics. Contrast to that, when reactant species exist at sufficiently low concentrations, they require extended periods to traverse the electrical double layer and undergo oxidation or reduction processes near the electrode surface. Under these conditions, the mechanism becomes diffusion-controlled (Andreas, 2015).

When a supercapacitor is fully charged and then disconnected from its external power source, the charges inside has insufficient time to distribute evenly throughout the tiny pores of the electrode material, for instance activated carbon. Alternatively, the charges tend to accumulate near the openings of the pores. The charges will then gradually be transported deeper into the pores due to the difference in charge concentration. However, this movement is strongly resisted because the small pores create much higher resistance, up to 10,000 times greater than that of the surrounding electrolyte (Graydon *et al*., 2014). This resistance significantly slows down the redistribution process. As a result, a spontaneous drop in voltage occurs, which is known as self-discharge or charge redistribution.

2.7.6 Dunn's Analysis

Dunn model is a theoretical method used to validate experimental findings by quantitatively analyzing the maximum diffusive and capacitive contributions of an energy storage device. In electrochemical studies, apart from Dunn, there are another method which known as Trasatti model. Both analysis models are commonly used to differentiate between capacitive and diffusive charge storage mechanisms (Chinnalagu *et al*., 2023). The Trasatti method provides an estimation of surface-controlled and diffusion-controlled processes by analyzing charge contributions at varying scan rates, often requiring extrapolation to extreme scan limits. This method is very helpful in figuring out the energy stored on the surface of the material, but not deep within it. Hence, this approach may result to a less accurate energy quantification. Contrast to Dunn's analysis, it acquires more detailed direct quantification by applying a power-law relationship between current and scan rate. Owing to its precision, Dunn's model is more favourable in interpreting the electrochemical behaviour of energy storage devices.

In Dunn's method, the current response obtained from the CV curves at a particular potential for a specified scan rate can be described as the amount of capacitive and diffusive current. This representation can be expressed as the Equation (2.4):

$$I(v) = K_1 v + K_2 v^{1/2} \quad (2.4)$$

Wherein, $I(v)$is the total current obtained at a specific potential in the CV curves, $K_1 v$ represents the capacitive contribution whilst the second part of the equation $K_2 v^{1/2}$ indicates the diffusive contribution. This equation will be used in constructing the Dunn's plot, by plotting $\frac{i(V)}{V^{1/2}}$ versus $V^{1/2}$. By comparing Equation 2.4 with the graph equation of y=mx+c, K_1 indicates the slope of the graph and K_2 is the y-intercept (Raavi *et al*., 2023).

Capacitive behaviour which associated to EDLC, and PCs mechanism are known to be very beneficial for applications that require high power density properties, which associated to fast kinetic and accessibility at the electrode surface. On the other hand, diffusive behaviour is often correlated with faradaic reaction within the electrode bulk, which linked to the ability to enhance the energy density. Therefore, while capacitive behaviour is often prioritized for fast response and cycle stability, a well-engineered contribution from diffusive processes can be equally valuable, especially in applications aiming to maximize both energy and power densities.

The experimental findings from the work conducted by Aftab *et al*., (2023) demonstrate the combined behaviour of asymmetric supercapacitor, which integrate the EDLCs and PCs characteristics. Through Dunn's analysis, the charge storage dynamics following the power law was examined. It was observed that the capacitive contribution increases significantly from 23% at a lower scan rate of 10 mVs^{-1} to 77% at a higher scan rate of 100 mVs^{-1}. At a higher scan rate, electrolyte ions have limited time to diffuse deeply into the electrode material, leading to a reduced diffusion-controlled (redox) contribution. Instead, surface-controlled (capacitive) processes become more dominant. These results indicate that the electrochemical performance of the asymmetric supercapacitor is governed by a combination of redox (diffusion-limited) and non-Faradaic (capacitive) mechanisms. Moreover, the higher energy density observed at lower scan rates can be attributed to enhanced redox reactions,

whereas the improved specific power at higher scan rates results from a decreased extent of electrochemical interactions between the electrode and electrolyte ions.

In a work reported by Iqbal *et al*., (2023), it was found that nickel sulphide/activated carbon (NiS/AC) sample exhibits a hybrid charge storage behaviour, as shown in Figure 2.7. At lower scan rates, the diffusive contribution dominates the overall capacitance, whilst capacitive contribution is evident on higher scan rates. The trend concluded that NiS/AC composite behave like a battery at lower scan rates and the performance shifted to an EDLC-like behaviour as the scan rate is increased. The synergistic effect between nickel sulphides and activated carbon is likely to be the reason behind the trend, in which nickel sulphides assists in the faradaic redox reaction and activated carbon is responsible for the EDLC behaviour. This dual mechanism is beneficial for practical applications that offers high energy storage high energy storage capability at lower scan rates and fast charge/discharge capability at higher scan rates.

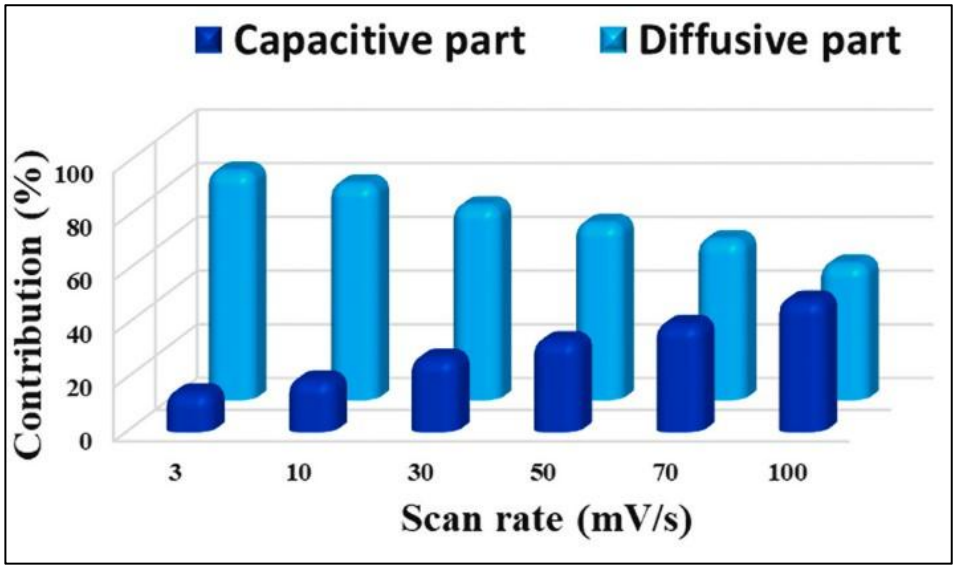

Figure 2.7 Capacitive and diffusive percentage bar graph by using Dunn's model (Iqbal *et al*., 2023)

Dunn's analysis for metal-organic framework/ carbon nanotube (MOF-CNT) has been studied by Anwer *et al*., (2023). In this specific work, generally similar trend in capacitive and diffusion contribution is observed, as reported by Iqbal *et al*., (2023). Figure 2.8 shows that at the lowest scan rate of 1 mVs^{-1}, the diffusive-controlled contribution dominates, accounting for approximately 80% of the total charge storage.

On the other hand, as the scan rate increases from 2 to 9 mVs^{-1}, the capacitive contribution increases steadily and become dominant, reaching more than 70% at 9 mVs^{-1}. This dual mechanism is expected for a hybrid electrode material, in which the synergy between the two combined materials contributed to the battery and EDLC-like properties. The MOF-CNT sample exhibit a sharp increase in capacitive controlled part at lower scan rates, implying faster transition from diffusion controlled to capacitive behaviour. This is likely due to the conductive properties of CNTs and the porous structure of MOFs, leading to a pronounce capacitive behaviour even at a very low scan rate.

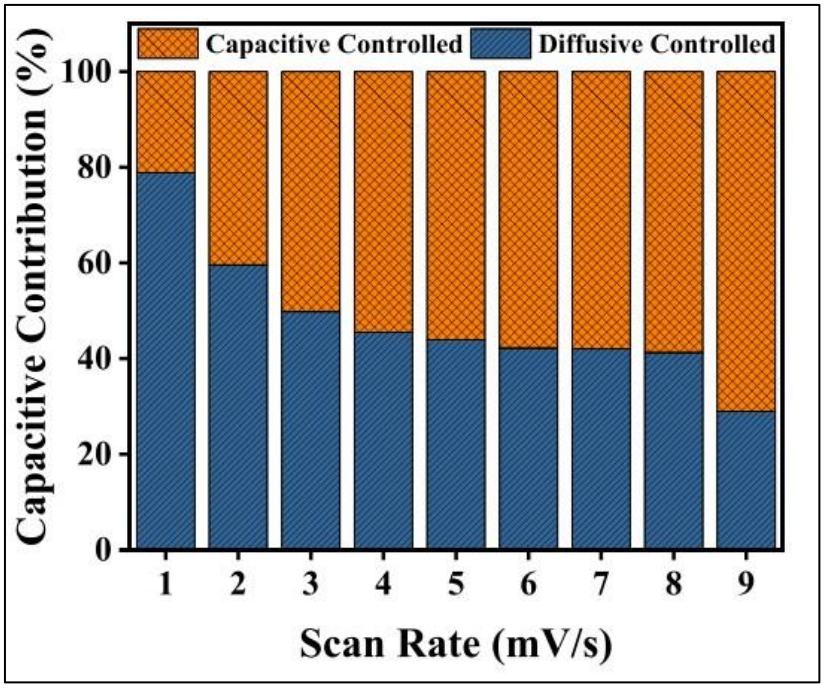

Figure 2.8 Capacitive and diffusive contribution percentage graph by using Dunn's model (Anwer *et al*., 2023)

2.8 Supercapacitor Material Selection via Theoretical Approach

Density functional theory (DFT) study is a powerful tool to study the fundamental structure, magnetic, and electronic properties of materials. For instance, a study conducted by Goclon, 2020 successfully discovered the effects of boron doping on carbon nano-onions (B-CNOs) with different numbers of layers. Numerous structures were examined with increasing boron content including two distribution patterns: a random distribution and a cluster formation. These findings are crucial as it can allow theoretical optimization of MTMOs before the actual experiments take

place. Therefore, the existence of certain material clusters in the real system can be postulated.

In the case of supercapacitor study, DFT analysis can justify the supercapacitive behaviour from the mechanistic standpoint. For example, in one DFT study, it was revealed that the pseudocapacitive charge storage observed in hydrous ruthenium oxide (RuO_2) electrodes is afforded by the excellent electronic and ionic transport through combined metallic conductivity and facile ion transport pathways between grain boundaries. The thermodynamic potentials and the electronic structure of the electrochemical interface can be apprehended by utilizing the first-principles simulation, in contrast to the continuum model, which requires the reaction free energy and transport barrier as input parameters. The capacitive-to-faradaic transition for anatase TiO_2 nanosheets were then revealed via these DFT calculations (Fleischmann *et al*., 2020).

Studies employing both theoretical modelling and experimental testing have shown that the total capacitance (CT) of a supercapacitor is dependent on two main components: the quantum capacitance (CQ), which originates from electrochemical charge storage processes, and the double-layer capacitance (CD), originates from ion adsorption at the electrode interface., with 1/CT = 1/CQ + 1/CD theoretical relationship (Li *et al*., 2023). It is also proven through DFT analysis that QC can be improved significantly through the addition of heteroatoms via co-doping (Majdi *et al*., 2023).

In summary, we utilized first-principles calculations to investigate how transition metal oxides (TMOs) and nitrogen atom modification affect the structure, electronic properties, quantum capacitance, and surface charge storage capacity of graphene-based materials. Our results showed that MnO, FeO, CoO, NiO, CuO and ZnO can stably adsorb onto graphene surfaces and significantly improve graphene's conductivity. This indicates their promise as electrode materials for electrochemical applications. The modelled quantum capacitance (CQ) and stored charge (Q) for the TMO-decorated graphene exhibited an asymmetric response, reaching maximum values under negative bias. This suggests these composite systems, especially NiO-graphene, are well-suited as cathode materials for asymmetric supercapacitors. Ultimately, our theoretical modelling provides atomic-level insights into how TMO

adsorption and nitrogen doping tailor graphene for optimized capacitive energy storage performance. Further experimental testing is still needed to realize the predicted enhancements in real-world supercapacitor devices.

Density functional theory (DFT) calculations provide insights into the interactions between electrons and nuclei in atoms, the nature of bonding between atoms, and ultimately allow us to predict the physical properties of materials. DFT has successfully described the characteristics and behaviours of materials by fundamentally understanding aspects like crystal structure, ion diffusivity, electronic interactions, phase transitions, etc. DFT has been able to successfully characterize and model the properties and behaviours of materials by elucidating fundamental features such as crystal structure, ion mobility, electronic interactions, phase transitions, and more. Research demonstrates that DFT calculations can substantially foresee the characteristics of material structures at the atomic scale. There exist various computational simulation software and methodologies that execute DFT computations, some examples being the Cambridge Serial Total Energy Package (CASTEP), Quantum Espresso Package, Wien2K, DMol3, and the Vienna Ab-Initio Simulation Package (VASP).

CHAPTER 3
METHODOLOGY

3.1 Introduction

Previously in literature review, the significance of various parameters on the optimization of SCs electrode material is highlighted. The synergy between structural and electrochemical conditions, as well as the comparisons of metal oxides, carbons, and hybrid SCs material are also emphasised. This work primarily focuses on comprehending essential specifications of EDLCs, pseudocapacitors, and its hybrid form. The objective is to facilitate the coordination between the initial selection of suitable electrode materials and the specific requirements of the intended final use. The evaluation of electrode criteria and overall device performance is conducted through a combination of methods, as depicted in figure 3.1.

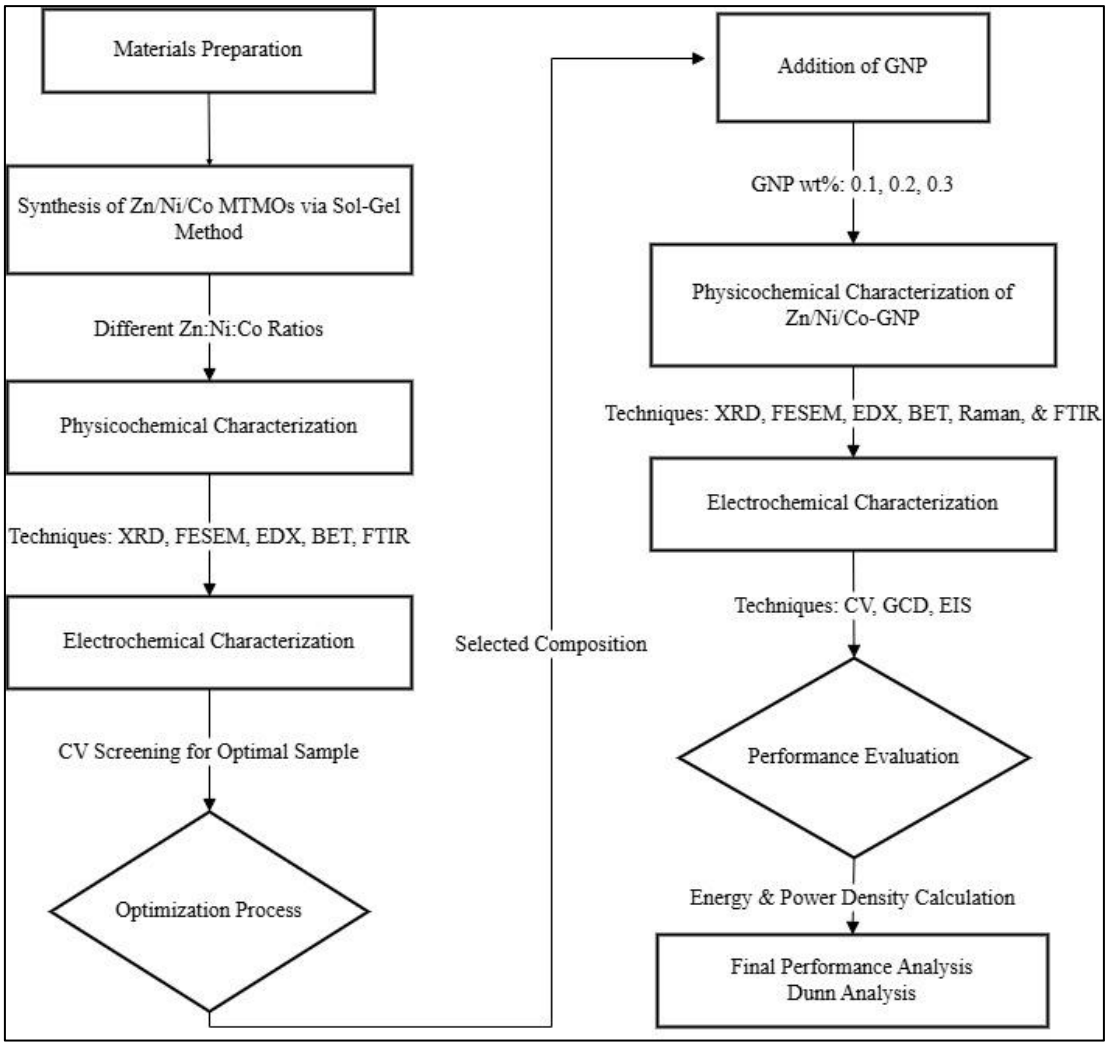

Figure 3.1 Methodology flowchart

3.2 Materials

The materials involved in the synthesis process are listed in table 3.1.

Table 3.1
List of material used in the preparation of Zn-Ni-Co MTMOs ternary nanocomposites and electrochemical characterization work

Material	Source
Cobalt nitrate hexahydrate	Merck
Nickel nitrate hexahydrate	Merck
Zinc nitrate hexahydrate	Merck
Oxalic Acid	
Ethanol	Merck
Potassium hydroxide electrolyte	Alfa Aesar
Sulphuric acid electrolyte	Alfa Aesar
Sodium hydroxide electrolyte	Alfa Aesar
Graphene Oxide	Merck

3.3 Preparation of Samples

The first phase of the research involves the synthesis of Zn-Ni-Co MTMOs (ZNC) with four distinct metal cation ratios: 1:1:1, 1:2:1, 1:1:2, and 2:1:1, followed by the physicochemical analysis. The Zn:Ni:Co molar ratios of 1:1:1, 1:2:1, 1:1:2, and 2:1:1 were deliberately selected to enable a systematic investigation of the individual and synergistic roles of Zn, Ni, and Co within a ternary mixed transition metal oxide (MTMO) system. The equimolar composition (1:1:1) serves as a balanced reference, providing a baseline for evaluating compositional effects. Next, the optimized ternary MTMOs obtained in part 2 will undergo supercapacitive studies which involve a series of electrochemical analyses as detailed out in Figure 3.1. The study will also be extended on the effect of GNP addition on the supercapacitive performance of optimized ternary MTMOs with GNP addition.

3.3.1 Formation of Zn-Ni-Co and Zn-Ni-Co/GNP Hybrid Composite

The ternary metal oxides consisting of Zn, Ni, and Co were synthesized via a sol-gel co-precipitation method, with oxalic acid as the chelating agent. The oxalic acid reacts with metal nitrates ($Zn(NO_3)_2$, $Ni(NO_3)_2$, and $Co(NO_3)_2$, forming a metal-

oxalate complexes with the general reaction constituted as:

$$M(NO_3)_2 + H_2C_2O_4 \rightarrow M(C_2O_4) + 2HNO_3$$

Where M represents Zn, Ni, or Co. The mixed metal oxalate complex was then subjected to thermal decomposition to form the desired ternary Zn-Ni-Co MTMOs. Upon heating, the oxalate decomposes, thus releasing CO and CO_2 gases, leaving behind a MTMO residue also constituted as:

$$M(C_2O_4)_n \rightarrow M_nO_m + \text{gaseous products}$$

3.3.2 Zn-Ni-Co Ternary Mixed Transition Metal Oxides

The preparation route for ZNC MTMOs is presented in Figure 3.2. Accordingly, the starting material consisting of metal nitrates hexahydrate of Co, Ni and Zn, $H_2C_2O_4 \cdot 2H_2O$ (oxalic acid) was used to prepare ZNC MTMOs via a modified oxalate assisted sol-gel co-precipitation route. In a typical procedure, 3.412 mmol of zinc nitrate hexahydrate ($Zn(NO_3)_2 \cdot 6H_2O$, molecular weight , MW = 297.49 g/mol), 3.412 mmol of nickel nitrate hexahydrate ($Ni(NO_3)_2 \cdot 6H_2O$, MW = 290.79 g/mol), and 3.412 mmol of cobalt nitrate hexahydrate ($Co(NO_3)_2 \cdot 6H_2O$, MW = 291.03 g/mol) were each dissolved separately in 10 mL of deionized water to form clear aqueous solutions.

The three metal precursor solutions were then combined in a 100 mL beaker under constant magnetic stirring to ensure uniform mixing. Subsequently, 20.472 mmol of oxalic acid dihydrate ($H_2C_2O_4 \cdot 2H_2O$, MW = 126.07 g/mol) was added slowly to the mixed solution. The presence of oxalate ions induced co-precipitation of the metal oxalates while the progressive gelation of the system facilitated homogeneous particle distribution, characteristic of the sol–gel process.

Following that, the mixture was stirred at 80 °C until a viscous and homogeneous gel was formed. This gel was oven-dried at 110 °C for 12 hours to remove residual water, producing a solid powder. The powder was ground using a mortar and pestle, followed by calcination in air at 350 °C for 3 hours with a heating rate of 5 °C/min to yield the Zn–Ni–Co ternary metal oxide composites. The steps were then repeated for other samples ratio according to Table 3.2.

Table 3.2
Stoichiometric calculations of precursor masses and molar amounts for Zn-Ni-Co TMO preparation

Zn: Ni: Co Ratio	$Zn(NO_3)_2 \cdot 6H_2O$	$Ni(NO_3)_2 \cdot 6H_2O$	$Co(NO_3)_2 \cdot 6H_2O$	$H_2C_2O_4 \cdot 2H_2O$
1: 1 :1	5.687 mmol, 1.691 g	5.687 mmol, 1.654 g	5.687 mmol, 1.656 g	34.130 mmol, 4.298 g
1: 2: 1	3.338 mmol, 0.993 g	6.676 mmol, 1.941 g	3.338 mmol, 0.972 g	26.706 mmol, 3.366 g
1: 1: 2	3.338 mmol, 0.993 g	3.338 mmol, 0.971 g	6.676 mmol, 1.943 g	26.706 mmol, 3.366 g
2: 1: 1	2.293 mmol, 0.682 g	1.146 mmol, 0.333 g	1.146 mmol, 0.334 g	9.173 mmol, 1.157 g

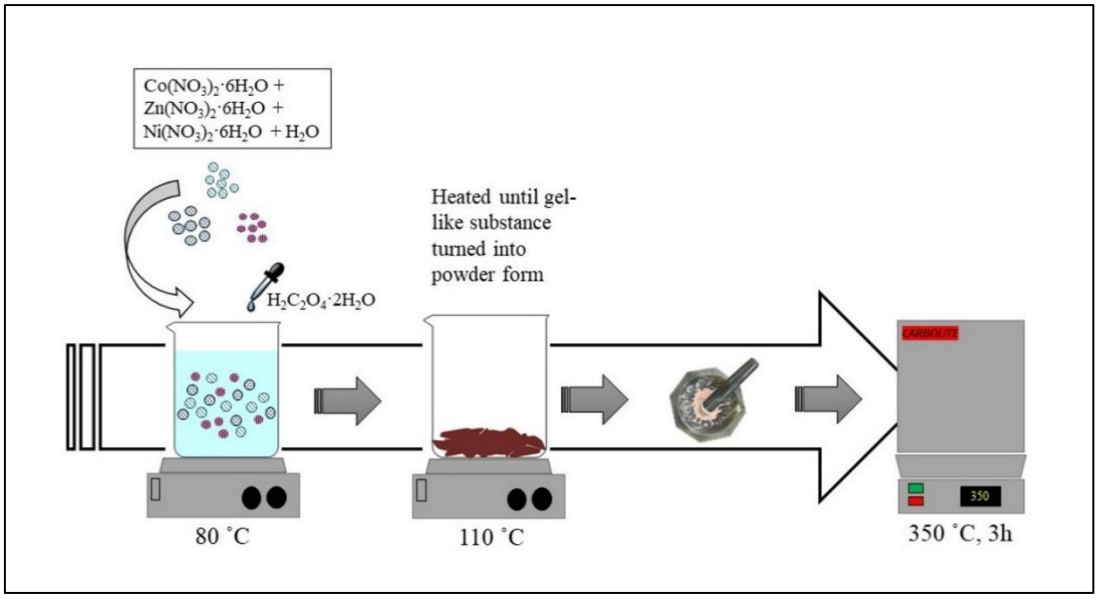

Figure 3.2 Preparation route Zn-Ni-Co MTMOs nanocomposite via sol-gel method

3.3.3 Zn-Ni-Co/GNP Hybrid Composites

ZNC was synthesized via a modified oxalate-assisted sol–gel co-precipitation method, as described previously. The molar ratio of Zn: Ni: Co precursors was

selected based on the optimum ratio determined in the specific capacitance screening described in Section 3.3.1. For the preparation of ZNC–GNP composites, a fixed mass of ZNC powder was dispersed in DI water and stirred for 30 min. In a separate beaker, GNP were dispersed in DI water via ultrasonication for 30 min to achieve a homogeneous suspension. The GNP addition was varied at 0.1 wt%, 0.2 wt%, and 0.3 wt% relative to the ZNC mass. The two suspensions were then combined and subjected to a continuous stirring for 24 h. The resulting mixture was centrifuged, washed several times with DI water and ethanol, and dried at 80 °C for 24 h to obtain the final ZNC–GNP composites. The overall synthesis procedure is illustrated in Figure 3.3.

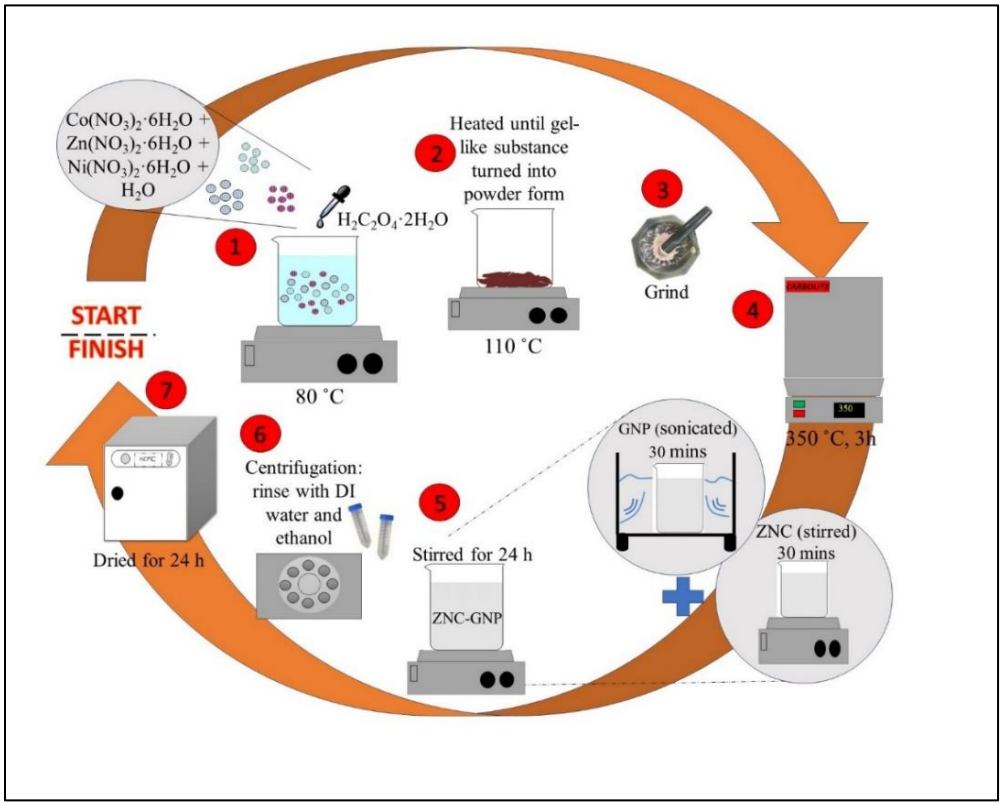

Figure 3.3 Preparation route Zn-Ni-Co/GNP nanocomposite via sol-gel method

3.4 Physicochemical Characterization

The physicochemical properties of the prepared materials were carefully analysed using various characterization techniques to assess their structural, morphological, compositional, textural, and functional attributes. The characterization techniques involve X-ray Diffraction (XRD), Field-Emission Scanning Electron

Microscopy (FESEM), Energy-Dispersive Spectroscopy (EDX), Brunauer Emmett Teller (BET), and Fourier Transform Infrared Spectroscopy (FTIR), Raman spectroscopy, and Ultraviolet-visible (UV-Vis) spectroscopy as described in the next sub-section.

3.4.1 X-ray Diffraction

The structures of the as prepared Zn-Ni-Co and Zn-Ni-Co/GNP samples were characterized by XRD (X'Pert Pro, PANalytical) with CuKα radiation, λ= 1.5406 Å at a voltage of 40 kV and a current of 40 mA. XRD serves as a valuable technique for structurally characterizing crystalline materials like MOFs, aiding in the phase identification process. The XRD system comprises three essential components: the X-ray tube, sample holder, and X-ray diffractometer. The XRD operates on the principle of generating X-rays through a cathode ray tube. In this process, a filament inside the cathode tube is heated, producing electrons. These electrons are then accelerated towards the sample by applying voltage, effectively bombarding the sample. When electrons gain sufficient energy from the incident beam, they can eject from their bound inner atomic shells and transition to higher energy outer shells. Additionally, the diffractometer directs X-rays of a defined frequency towards the sample. These incident X-rays interact with the periodic lattice of the sample's crystalline atoms, producing constructive interference and diffracted rays when Bragg's law is fulfilled. More specifically, diffraction occurs at angles where the path length difference between X-rays scattered from adjacent lattice planes results in reinforcing wave phases, detectable as intense exiting beams. The crystallite size of the prepared sample is computed by employing the Scherrer Equation (3.1) whilst the lattice constant is deduced by implementing Equation (3.2).

$$D = \frac{k\lambda}{\beta \cos \cos \theta} \tag{3.1}$$

$$a = D\,(h^2 + k^2 + l^2)^{\frac{1}{2}} \tag{3.2}$$

In which D is the crystallite size (nm), k is the Scherrer constant, λ represent the

wavelength of the x-ray source, β symbolizes the full width at half maximum (FWHM) of the diffraction peak, θ is the peak positions, and hkl is referring to the miller indices.

3.4.2 Field Emission Scanning Electron Microscopy- Energy Dispersive X-Ray Spectroscopy

Field emission scanning electron microscopy (FESEM) is a powerful technique for obtaining high-resolution images of material surfaces, which enable extensive observation of microstructural features such as morphology, particle size, and surface texture. It is commonly integrated with energy-dispersive X-ray spectroscopy (EDX), which allows simultaneous qualitative and quantitative analysis of elemental composition at specific regions of interest. This combined approach is widely employed in materials characterization to correlate surface features with chemical composition, providing comprehensive insights into the structural and compositional attributes of the sample. In this study, FESEM imaging was performed to examine the surface morphology of the samples, while EDX analysis was conducted to determine the elemental distribution and composition at selected points on the sample surface. In this work, as prepared Zn-Ni-Co and Zn-Ni-Co/GNP samples were analysed via FESEM Thermo Scientific Apreo 2 S equipped with an EDX system (Bruker). Imaging was performed in high vacuum mode at an accelerating voltage of 5 kV using a T2 detector, with a working distance of approximately 7.94 mm. Elemental composition was determined at selected points on the sample surface using the Bruker EDX under the same operating conditions.

FESEM typically utilizes a focused electron beam to image a sample's surface topography at high resolution. Resolutions from the micrometre to nanometre scale can be achieved. The sample being analysed is irradiated with electrons of a defined energy. These electrons interact with the sample's atoms at various depths. This interaction results in emitted electrons and signals that provide information to reconstruct an image revealing the surface structural features of the specimen. The generation of signals such as back-scattered electrons, secondary electrons, and characteristic X-rays occurs during the process. The detector collects topographic images of the sample from either the back-scattered or secondary electrons, depending

on the specific type of detector integrated into the machine.

Energy-dispersive X-ray spectroscopy (EDX), also referred to as EDS or EDXS, is a widely used and reliable method for chemical characterization and imaging. This technique enables localized chemical analysis by detecting X-rays emitted from a solid specimen when it is bombarded with a focused electron beam (Bernardi 2021). This interaction causes the emission of characteristic X-rays unique to each element, allowing identification and quantification of the sample's composition. In principle, EDX can detect elements ranging from beryllium (atomic number 4) to uranium (atomic number 92). However, the ability to detect lighter elements ($Z < 10$) is dependent to the specific capabilities of the instrument that is being used. The qualitative analysis via EDX spectroscopy involves identification of the characteristic X-ray peaks in the spectrum, which is typically straightforward due to the relatively simple structure of X-ray emission patterns. On the other hand, quantitative analysis requires measurement of the intensities of these peaks. These values are then compared to those obtained from reference standards with known elemental compositions, allowing for the calculation of element concentrations within the sample.

The accuracy of the peak identification in EDX is heavily dependent to a proper system calibration. Therefore, to ensure good accuracy measurements for characteristic X-ray peaks, calibration is needed prior to any automated or manual identification process. In general, the first step of calibration process involves analysing a material with well-established X-ray emission lines where copper (Cu) is commonly used for this purpose since its spectrum provides distinct peaks at both low and high photon energies (Scimeca *et al*. 2018). Another approach is to use a sample that combines aluminium (Al) and Cu, for instance a copper coin partially covered with aluminium foil. By continuously scanning this sample, the system can simultaneously detect the Al K–L_3 peak at 1.487 keV and the Cu K–L_3 peak, effectively covering both ends of the energy spectrum needed for calibration. Once calibrated, the system’s accuracy and linearity should be verified by analysing elements with known intermediate photon energies. A well-calibrated EDX detector is expected to report photon energies within ±2.5 eV of the known values.

3.4.3 Fourier Transform Infrared Spectroscopy

Fourier transform infrared spectroscopy (FTIR) is a widely utilized technique for identifying the functional groups present in materials (gas, liquid, and solid) by employing a beam of infrared radiations. This work employs FT-IR spectrometer (PerkinElmer Spectrum 100) for this purpose. The FTIR analysis was performed in the frequency range of 500 cm^{-1} to 4000 cm^{-1} at room temperature. In this method, an infrared spectroscopy measures the absorption of infrared radiation by each bond in the molecule, resulting in a spectrum commonly represented as % transmittance versus wavenumber (cm^{-1}), which is known as infrared spectrum (Khan *et al.*, 2018). The absorbance spectrum of a sample is calculated from Equation (3.3):

$$A = \log\left(\frac{I_0}{I}\right) \tag{3.3}$$

In which A represents the absorbance, I_0 is the intensity in the background spectrum, whilst I is the intensity in the spectrum of the sample. The correlation between absorbance and the concentration of molecules in a sample can also be established using the Beer's law equation presented in Equation (3.4):

$$A = \varepsilon l C \tag{3.4}$$

In which, ε represents the molar absorptivity, ι is the path length, and C denotes the sample's concentration. The height or area of a peak in an absorbance spectrum is proportional to concentration; therefore, Beer's law can be used to determine the concentrations of molecules in samples.

3.4.4 Brunauer Emmett Teller

Nitrogen adsorption/desorption measurements were performed using a surface area analyser (Micromeritics, ASAP 2060) at 77K. The specific surface areas of the Zn-Ni-Co and Zn-Ni-Co/GNP were determined by BET method, using the BET equation and the pore diameters were evaluated using the Barrett-Joyner-Halenda (BJH) method. The theory of BET, examining the physical adsorption of a gas adsorbate on a solid adsorbent, was initially published in 1938 by Stephen Brunauer, Paul Hugh Emmett, and Edward Teller. The BET method enhances the Langmuir theory by incorporating multilayer adsorption, extending beyond monolayer coverage.

It considers the possibility that molecules already adsorbed on the surface can serve as sites for additional adsorption. Therefore, as layers build up, the number of available sites for attaching new molecules increases, enabling multilayer formation. For accurate analysis, an inert gas like nitrogen (N_2) is utilized to avoid any surface reactions. N_2 is most often used for BET analysis since it satisfies the key requirement of being non-reactive with the material surface under study. The equation used in this analysis is presented as Equation (3.5) and Equation (3.6):

Wherein, ρ_0 is the equilibrium pressure, ρ represents the saturation pressure, C is the BET constant, n_m denoted the number of gas molecules adsorbed, whilst E_1 is the heat of adsorption for the first layer, and E_L is the liquefaction energy.

$$\frac{\rho}{n(\rho_0 - \rho)} = \frac{1}{n_m C} + \frac{C-1}{n_m C} \times \frac{\rho}{\rho_0} \tag{3.5}$$

$$C = \boldsymbol{exp}\, exp\, (\frac{E_1 - E_L}{RT}) \tag{3.6}$$

3.4.5 Raman Spectroscopy

Raman spectroscopy is a tool that is utilized in investigating the molecular structure as well as the composition of samples. It provides a pivotal insight into the structural characteristics of the carbon component in the Zn-Ni-Co–GNP composite, particularly the degree of graphitization and the presence of structural defects. In this work, Raman spectroscopy (Witec, Alpha 300R) was utilized to measure the molecular vibrations. principle used is based on the inelastic scattering of monochromatic light from a laser source. The energy difference between the incident and scattered photons gathered the information about the vibrational modes of the molecules in the tested samples. In a typical Raman testing, the sample is exposed to an intense monochromatic light source, commonly at λ= 532 nm and 785 nm. A phenomenon named Rayleigh scattering is associated with this technique, in which the scattered radiation retains the same wavelength as the incident light. However, a small fraction of light will be found to be scattered at a slightly different wavelength than that of incident ray, resulting in a wavelength shift. In this work, we specifically employed λ= 532 nm due to its ability to enhance the Raman signals for both carbon

structures and metal oxides/hydroxides. The range of Raman shift scanned was from 100 cm^{-1} to 3500 cm^{-1}. Prior to measurements, the samples were placed on a clean, non-fluorescent substrate to minimize background interference. The laser power and exposure time were optimized to prevent sample degradation while ensuring adequate signal-to-noise ratios. To ensure a reliable data collection, multiple spectra were acquired from different regions of each sample.

Raman spectroscopy is known to have good ability in capturing signals from non-polar functional groups, such as carbon and symmetric aromatic ring vibrations. Like infrared spectroscopy, Raman spectra provide the molecular fingerprints that consists of the compound's information, the pattern in bonding, as well as the differences in crystalline forms. The compound identification is done by comparing the observed peaks to known references. For instance, this technique is capable in distinguishing between diamond and graphite which are both in the same family of carbon, by analysing its atomic arrangements (Jayasooriya & Jenkins, 2002).

3.4.6 UV-Visible Spectroscopy

The optical properties of the samples were investigated using a UV-Vis spectrophotometer (Shimadzu UV-2600, wavelength range: 200–900 nm). Powder samples (approximately 3 g) were placed directly into the solid-sample holder without pelletization. In a typical UV-Vis spectrophotometer, the intensity of light is assessed as it passes through a sample solution within a cuvette, comparing it to the light intensity before entering the sample. Essential components of a UV-Vis spectrophotometer consist of a light source, a sample holder, a dispersive mechanism for separating light into different wavelengths (e.g., a monochromator), and an appropriate receptor. The light absorption is measured as a function of wavelength, which gives the electronic transitions information that occurred in the material.

The optical bandgap (E_g) was determined using the Tauc method, first introduced by Tauc in 1966 (Makuła *et al.*, 2018), which estimates E_g from the optical absorption spectra. The Tauc method relies on the premise that the energy-dependent absorption coefficient α can be represented by the absorbance at energies below E_g, yielding results according to Equation (3.7).

$$(\alpha \cdot hv)^{\frac{1}{\gamma}} = B(hv - E_g) \quad (3.7)$$

Planck constant is represented by h, v for frequency of photon, Eg depicts the band gap energy, and B is a constant. The γ factor varies based on the characteristics of the electron transition, which equal to either ½ for direct band gap or 2 for the indirect transition. The energy of the band gap is typically extracted from diffuse reflectance spectra (Makuła *et al*., 2018).

3.5 Electrochemical Characterization

The electrochemical measurements were conducted via a three-electrode system operated by an Autolab PGSTAT204N potentiostat. A standard three-electrode electrochemical cell consists of a working electrode (where the active material is coated), counter electrode, and reference electrode submerged in the same electrolyte solution, as seen on Figure 3.4. The reference electrode provides a stable and known potential, ensuring precise control over the potential applied to the working electrode. This allows for a clearer understanding of the redox processes and charge storage mechanisms occurring on the surface of the electrode material. In a typical experiment, electrical current flows between the working and counter electrodes. Simultaneously, the working electrode's potential is measured against the reference electrode, which maintains a steady baseline potential. This setup allows both controlling and monitoring the working electrode's potential precisely by separating the current-carrying and potential-sensing functions across two distinct electrode interfaces. Hence, the main current circulates between working and counter electrodes only, while the reference electrode tracks the working electrode potential to complete the circuit. In this work, the setup was using a glassy carbon electrode (GCE) with drop-casted sample on its tip as the working electrode, Ag/AgCl served as the reference electrode, platinum wire used as the counter electrode, with 2 M KOH as the electrolyte.

Compared to a two-electrode system which often used in practical device testing, the three-electrode system eliminates the interference from the counter electrode, which can otherwise contribute to the measured capacitance and obscure the intrinsic properties of the material under study. As these external factors are minimized, the three-electrode system enables a more focused investigation of the

specific capacitance, charge/discharge kinetics, and reversibility of the electrode reactions. By employing the three-electrode setup in this work, it allows a detailed understanding of the material's electrochemical behaviour before progressing to full-cell configurations. This serves as a foundational evaluation to optimize the material synthesis and electrode preparation parameters prior to device-level testing.

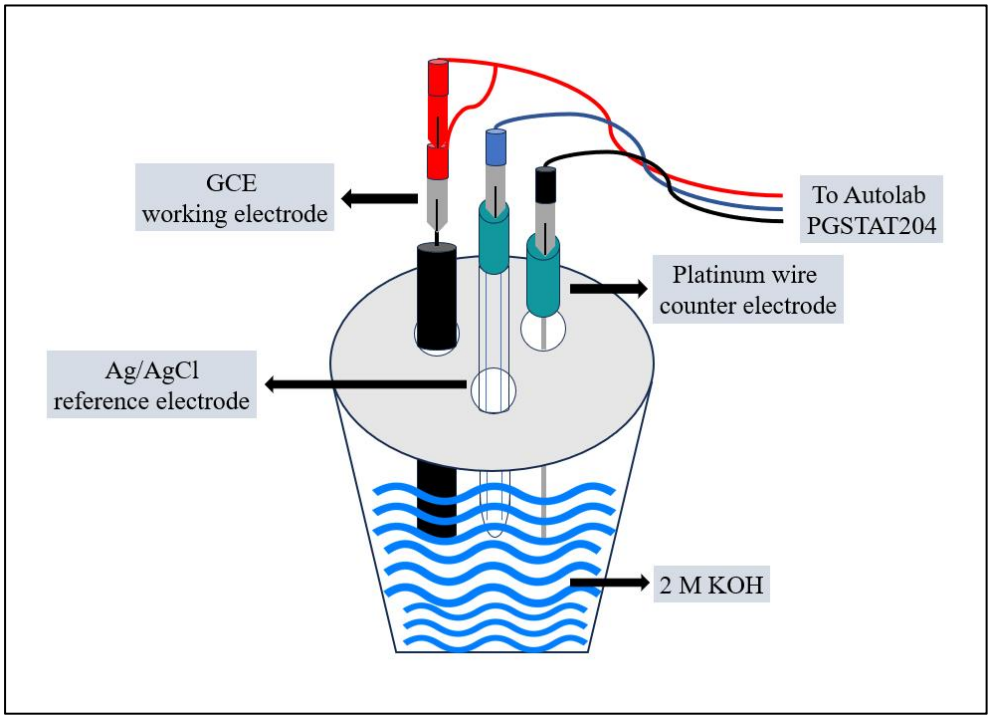

Figure 3.4 Three electrode system setups

In a three-electrode electrochemical system, it is important for the working electrode and reference electrode tips/surfaces to be positioned at the same height in the cell, such that they are making contact with the electrolyte solution at the same depth. This same plane positioning is crucial for the following reasons:

i. To minimize interference from solution resistance (IR drop). If the distance between the working and reference tips varies significantly, the resistance that is experienced by the electrode can be differ. This causes an IR drop effect that leads to inaccurate potential measurement.

ii. To avoid variability in diffusion layer thickness because both working and reference electrode need to be kept at identical spots in the electrolyte to

ensures they have similar diffusion layer thicknesses. If one is higher, convection effects can thin out the diffusion layer near it.

iii. To maintain identical temperature zones since thermal gradients can develop in the cell if the electrodes are located far apart vertically. The temperature directly impacts the measured potentials.

3.5.1 Electrode Cleaning

The GCE surface was polished using alumina slurry along with a polishing cloth or pad. Polishing gave the surface a mirror finish and eliminated any loose graphite or contaminants. After polishing, the GCE was sonicated in deionized water for 5 to 10 minutes, to remove any leftover alumina particles.

3.5.2 Cyclic Voltammetry

The electrochemical cell required cleaning before use. To clean it, the cell was filled with 99.9% H_2SO_4 and allowed to sit overnight at room temperature. Afterwards, the cell underwent several rinses with DI water to remove residual acid. Next, the cell was filled with the 2M KOH electrolyte. Finally, the reference electrode, counter electrode, and working electrode were assembled into the clean cell, preparing the full setup for the electrochemical experiments.

3.5.3 Galvanostatic Charge Discharge Cycle

Galvanostatic charging/discharging provides a more precise way to determine a material's Cs. This method applies consistent anodic and cathodic currents to the working electrode to charge and discharge it within a defined voltage window. It applies a constant current load that mimics real charging/discharging conditions better than the variable currents in CV. This allows measuring the intrinsic capacitance performance directly. From the obtained galvanostatic data, the Cs value can be accurately calculated using the absolute current, voltage range, and discharge time (Parsapour *et al.*, 2023). By employing Equation (3.8), the Cs value can be determined.

$$C_s = \frac{I \times \Delta t}{m \times \Delta V} \tag{3.8}$$

Based on the equation, I represent the applied current (A), Δt defines the discharge period in seconds, m denotes the mass of the active materials in the unit of gram, and ΔV is the potential window (V).

3.5.4 Electrochemical Impedance Spectroscopy

Electrochemical impedance Spectroscopy (EIS) is an essential tool to provide thorough electrochemical performance examination on the electrode materials, specifically probing into attributes like conductivity and the charging transport properties at the interface between the electrode and electrolyte. Moreover, EIS can highlight the mobility of electrons and ions. EIS has become more widely used because it can determine and supply data on the electrical resistance present in systems including SCs and LIBs. A diverse array of physical and chemical phenomena in EIS is delineated by executing a single experiment encompassing a broad frequency range. The Bode plot, a crucial representation in EIS, illustrates the frequency-dependent behaviour of the impedance phase angle. It presents the connection between frequency and the imaginary part of impedance, $Z''(\omega)$. The material's capacitance can be derived from the linear segment of a graph plotting log Z'' against log f, by employing Equation (3.9).

$$C = \frac{1}{2\pi f \left|Z''\right|} \tag{3.9}$$

Herein, C denotes the capacitance (F), f represents the frequency, whilst Z'' corresponds to the imaginary impedance. In a typical EIS plot, it consisted of a low-frequency region and high-frequency region. At the lower frequency region, the straight line is attributed to the Warburg element (W), which characterizes diffusion within the electrode materials. In the high frequency region, the solution resistance (R_s) can be obtained from the intersection of the semicircle with the real axis Z'. Furthermore, another resistance occurred at a higher frequency region known as charge transfer resistance (R_{CT}) which arises because of impediments to the smooth

flow of electrons across the interface between the electrode surface and the electrolyte solution. (Parsapour *et al*., 2023).

3.5.5 Dunn Analysis

Dunn's model is employed on the Zn-Ni-Co and Zn-Ni-Co/GNP samples to articulate the capacitive and diffusive contributions. The analysis model will be using CV analysis data at various scan rates in order to collect the current response data across a range of electrochemical condition. Next, the area under the CV curve is obtained for each scan rate to extract the corresponding charge capacity. This step allows for quantification of the total stored charge, which is then used to calculate capacitance as a function of scan rate. The resulting data are plotted to observe how capacitance trends evolve with increasing scan rates, providing preliminary insight into kinetic behaviour. The methodology flowchart for Dunn's analysis is presented in Figure 3.5. This analysis describes the relationship between peak current (i) and voltage (v) in an asymmetric SCs electrode via a power law equation presented in Equation (3.10) and Equation (3.11).

$$i = av^b \tag{3.10}$$

$$log\ log\ (i)\ = log\ log\ (a) + b\ log(v) \tag{3.11}$$

In this equation, i represents the peak current and v stands for the scan rate. The b value indicates the type of electrochemical process taking place. Typically, b value that is close to 0.5 suggests a diffusion-controlled battery-like process. On the other hand, b value close to 1 depicted a pseudocapacitive charge storage mechanism. By examining how the b value changes, the dominating electrochemical reaction in the SCs electrode can be determined (Asghar *et al*., 2023). The shifts in the b parameter provides insights into the transitions between capacitive, diffusion-limited, and resistive behaviours in the electrode material. The total capacitance stored in an electrode arises primarily from two mechanisms: surface capacitive effects and diffusion-controlled processes. Surface capacitance consists of both a faradaic contribution, resulting from pseudocapacitive redox reactions at the electrode surface, and a non-faradaic contribution, originating from electrical double-layer formation. In

contrast, diffusion-controlled capacitance is governed by ion transport into the electrode bulk, where ion diffusion plays a more significant role than surface interactions.

In support of experimental analysis, this mathematical modelling can also contribute to an insight towards the effect of the structure of material and its composition on the charge storage mechanism. Through Dunn's analysis model across varying scan rates, it is highly possible to associate the morphological features such as surface area and porosity on the capacitive contribution of the tested material. This model will provide a comprehensive validation on the role of GNP in enhancing the storage ability, particularly at higher scan rates. Theoretically, the trends observed in Dunn's analysis will be consistent with the trend shown in CV and GCD analysis.

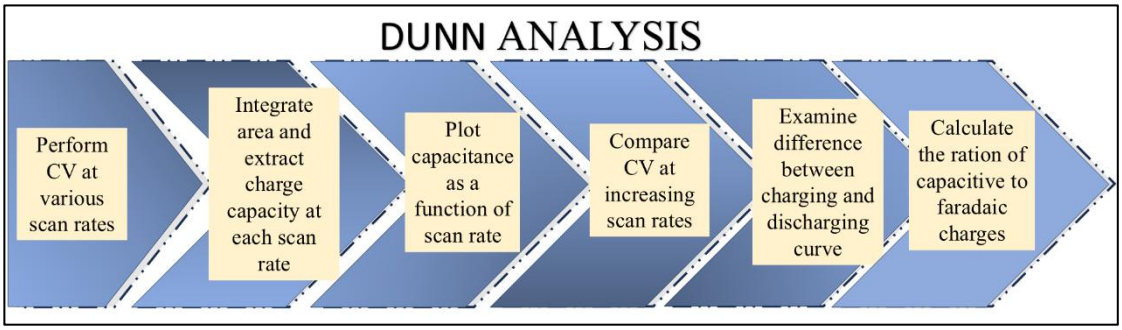

Figure 3.5 Dunn's Analysis method flowchart

CHAPTER 4
RESULT AND DISCUSSION

4.1 Structural Characterization

Understanding the structure of Zn-Ni-Co mixed transition metal oxides (ZNC) is all about exploring and identifying their physical and chemical makeup. This process is vital for comprehending the properties of these materials, which are key to their effectiveness in applications, especially in energy storage system. The crystal structure, phase composition, and crystallite size of ZNC at various compositions is determined via XRD analysis as shown in Figure 4.1. Evident from figure 4.1, similar peak positions can be seen on both ZC and the group of ZNC samples. The arising diffraction peaks as shown in Table 4.1 are in good agreement with the simulated crystallographic data (JCPDS:00-023-1390) reported by (Faras *et al.* (2023). Compared to the stick pattern of zinc cobaltite shown on Figure 4.1, the resemblance proves that zinc cobaltite and the ZNC MTMOs have similar spinel cubic structure. The crystallite size of the prepared sample is computed by employing the Scherrer equation (4.1), whilst the lattice constant is deduced by implementing Equation (4.2)

$$D = \frac{k\lambda}{\beta \cos \cos \theta} \tag{4.1}$$

$$a = D\,(h^2 + k^2 + l^2\,)^{\frac{1}{2}} \tag{4.2}$$

In which D is the crystallite size (nm), k is the Scherrer constant, λ represent the wavelength of the x-ray source, β symbolizes the full width at half maximum (FWHM) of the diffraction peak, θ is the peak positions, and hkl is referring to the miller indices. The details on FWHM, crystallite size, and cell parameter of ZC and ZNC samples using XRD spectra are presented in Table 4.1. The resulting crystallite size from the most intense peak (311) of ZC appeared to be smaller compared to the ZNC samples with various Zn: Ni: Co ratios. The crystallite size of ZNC 111 sample which indicates equal Zn: Ni: Co ratios is 16.32 nm, which is almost doubled from ZC.

For ZNC 121 sample, more Ni is available in the mixed oxides thus resulted to the smallest crystallite size (11.39 nm) compared to the other ZNC samples because of the small ionic radii nature, compared to Zn and Co. As for ZNC 112, more Co in the mixed oxide allows formation of greater crystallite size (16.05 nm) particles compared to ZNC 121, but less than ZNC 211 sample (19.14 nm) which shows the largest crystallite size of all four ZNC composites prepared in this work.

The size obtained is in agreement to the value acquired by Kumar *et al*. (2021), which ranged between 12 nm to 17 nm. The reduction of crystal size is apparent as greater Zn^{2+} ions (ionic radii of 0.74 Å) are substitute with Ni^{2+} ions which have smaller ionic radii of 0.69 Å, as well as the difference in their atomic number (Co = 27, Zn = 30, and Ni = 28) (Raja *et al*., 2014). The crystallite size is also paramount to the energy storage capability, supposing that it describes the material's degree of electrical conductivity. Smaller crystallite size is analogous to a wider redox active site for reaction to take place, thus promoting the specific capacitance (Cs) (Hepel, 2022).

Figure 4.2 portrays the magnified view of the (311) diffraction peaks as a function of x. Evident from the graph, the (311) peak of ZC is slightly shifted to the right when Ni is added onto the ZC matrices. $ZnCo_2O_4$ has a spinel structure, where Zn^{2+} and Co^{3+} ions occupy specific lattice sites. Hence, when Ni^{2+} is introduced into the system, it can partially substitute for either Zn^{2+} or Co^{2+} ions in the spinel structure. In the event Ni^{2+} replaces Zn^{2+} or Co^{2+} in the crystal lattice, the smaller ionic size of Ni^{2+} causes a contraction of the unit cell, thus also leads to a decrease of lattice parameters value, as presented in table 4.1. As a result of this lattice contraction, the diffraction angle (2θ) increases, shifting the (311) peak to the right in the XRD pattern.

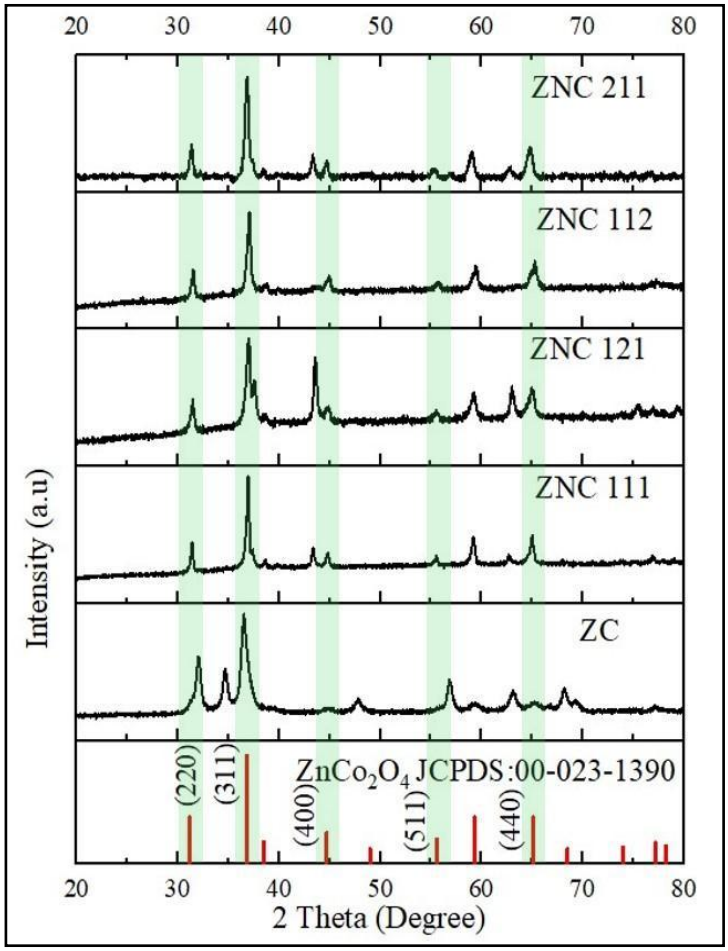

Figure 4.1 XRD patterns of ZC, and ZNC samples at various compositions

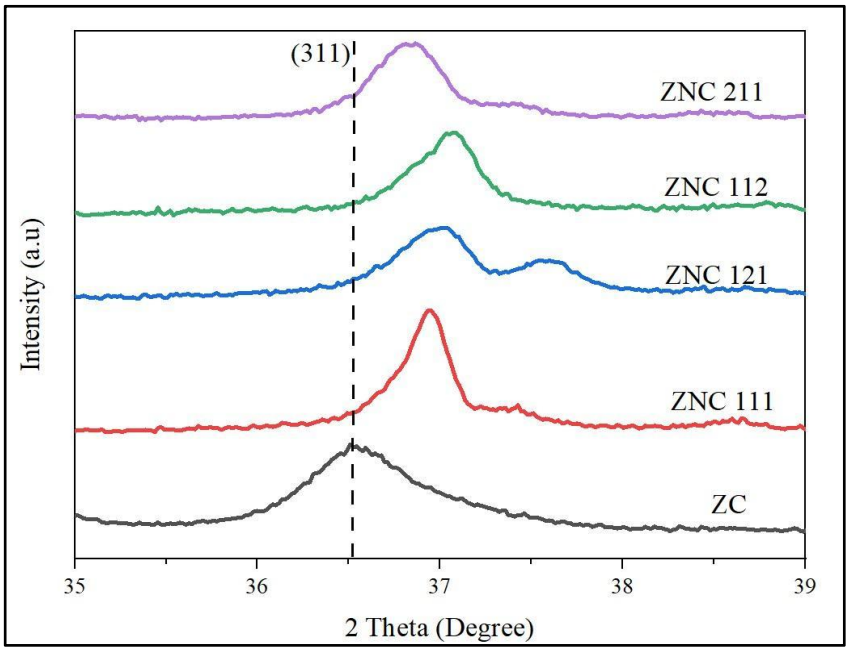

Figure 4.2 Magnified view of the (311) diffraction peaks as a function of x

Table 4.1
The peak positions in XRD patterns of ZC and various ZNC samples

Samples/Peaks	(220)	(311)	(400)	(511)	(440)
JCPDS 00-023-1390	31	36	44	55	65
ZC	32.06	36.55	44.92	56.89	65.37
ZNC 111	31.55	36.96	44.79	55.47	65.12
ZNC 121	31.55	36.96	44.92	55.60	64.98
ZNC 112	31.55	37.07	44.92	55.72	65.25
ZNC 211	31.42	36.82	44.79	55.22	64.87

Table 4.2
The FWHM, crystallite size, and cell parameter of ZC and various ZNC samples using XRD spectra

Samples	(311) Peak position, 2θ (˚)	FWHM (Deg.)	Crystallite size, d (nm)	Cell parameter a=b=c, (Å)
ZC	36	0.52	8.61	8.11
ZNC 111	36.55	0.26	16.32	8.07
ZNC 121	36.96	0.34	11.39	8.06
ZNC 112	36.96	0.82	16.05	8.07
ZNC 211	37.07	0.51	19.14	8.09

Figure 4.3 displays the XRD patterns of GNP, ZNC, and ZNC-GNP samples at various compositions. In all three ZNC-GNP samples, there are 6 apparent peaks correspond to (002), (220), (311), (400), (511), and (440) as described in Table 4.3. The peak at (002) is associated to the presence of GNP in all ZNC-GNP samples prepared in this work. It is also in good agreement with the JCPDS card 041-1487 for

graphite. The rest of the above-mentioned peaks are associated with Co_3O_4 JCPDS 03-065-3103, and $ZnCo_2O_4$ JCPDS 00-023-1390 which are the main matrix phases in the synthesized ZNC-GNP samples. It is also evident in Figure 4.3 that the (002) intensifies as the amount of GNP increases. It can also be observed that the most prominent peak (311) for all ZNC-GNP samples became broader compared to ZNC. This peak broadening indicates the formation of smaller crystallite size particles, which explains the size decrement of ZNC once GNP is introduced. The information on FWHM, crystallite size, and cell parameter of various ZNC-GNP samples in comparison to ZNC is presented in Table 4.4.

The average crystallite size reduction from 16.05 nm ZNC to 11.22 nm, 11.5 nm, and 11.66 nm for ZNC-GNP 0.1, ZNC-GNP 0.2 and ZNC-GNP 0.3, respectively can be relate to the growth suppression of metal oxides crystallites cause by the introduction of GNP, which act as a physical barrier during the synthesis process. Moreover, the two-dimensional configuration of GNP offers an expansive surface, which can inhibit the coalescence and expansion of the MTMO particles, resulting in the formation of smaller crystallites.

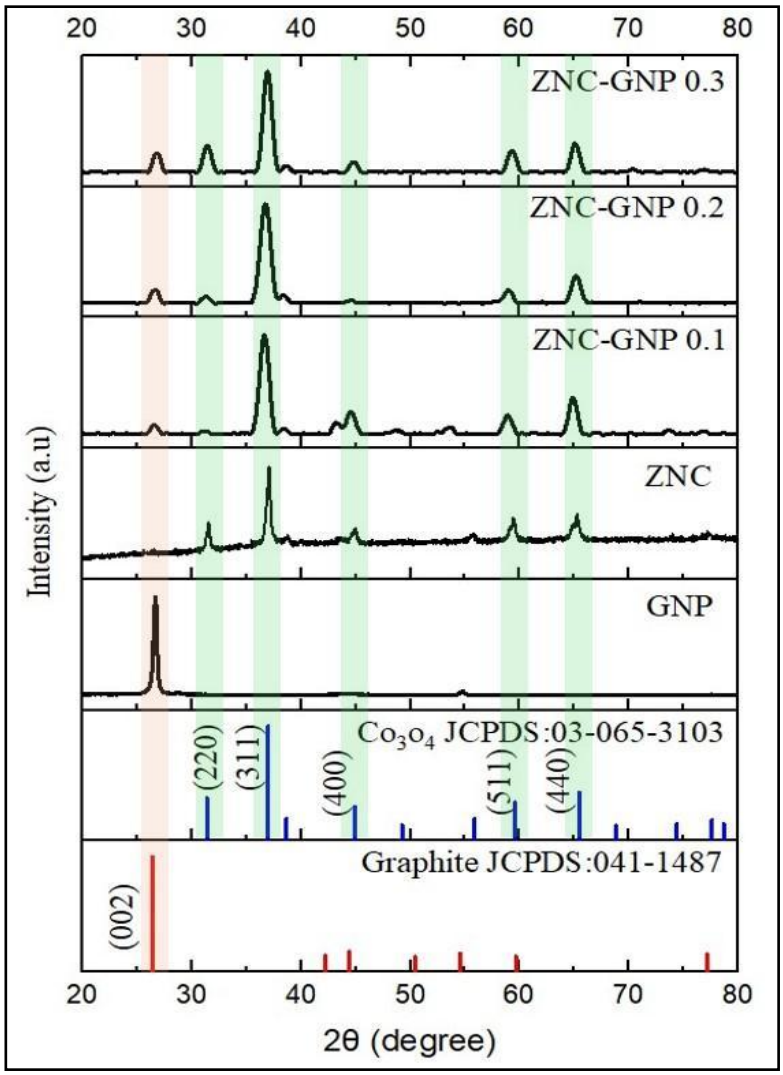

Figure 4.3 XRD patterns of GNP, ZNC, and ZNC-GNP samples at various compositions

Table 4.3
Peak positions in XRD patterns of ZNC and various ZNC-GNP samples.

Samples/Peaks	(220)	(311)	(400)	(511)	(440)	(002)
JCPDS 03-065-3103	31.42	36.96	44.92	59.58	65.50	-
JCPDS 041-1487	-	-	-	-	-	26.40
ZNC 112	31.55	37.07	44.92	55.72	65.25	-
GNP	-	-	-	-	-	26.66
ZNC-GNP 0.1	31.29	36.56	44.67	58.95	64.90	26.58
ZNC-GNP 0.2	31.29	36.69	44.53	59.06	65.25	26.66
ZNC-GNP 0.3	31.42	36.96	44.80	59.33	65.12	26.79

Table 4.4
The FWHM, crystallite size, and cell parameter of various ZNC-GNP samples using XRD spectra

Samples	(311) Peak position, 2θ (˚)	FWHM (Deg.)	Crystallite size, d (nm)	Cell parameter a=b=c, (Å)	Cell parameter a=b=c, (Å) reported from other study
ZNC 112	36.96	0.82	16.05	8.07	8.11 (Kumar *et al.*, 2021)
ZNC-GNP 0.1	36.56	0.95	11.22	8.07	This work
ZNC-GNP 0.2	36.69	1.09	11.50	8.11	
ZNC-GNP 0.3	36.96	0.93	11.66	8.07	

4.2 The Physicochemical Properties Differences of Zn-Ni-Co and Zn-Ni-Co/GNP Hybrid Composite

4.2.1 Surface Morphology

The morphology of the samples was studied by FESEM analysis. The detailed FESEM confirmed the presence of all individual Zn, Ni, Co and GNP. In this subtopic, each FESEM photomicrograph will be discussed in detailed. The morphology of zinc cobaltite (ZC) can be seen in Figure 4.4 a). ZC displays clusters of small globular particles that also agglomerated into larger clusters, forming a hierarchical structure. The individual globules exhibit a rough, uneven surface which possibly indicates a high surface area characteristic. Moreover, the arrangement of the globular particles creates visible voids and interconnected pores, forming a porous network structure which beneficial for charge storage application.

Figure 4.4 b), c), d) and e) represents the FESEM micrograph for ZNC samples with various Zn: Ni: Co ratios. The morphology of ZNC 111 as shown in Figure 4.4 b) revealed a well-defined, angular plate-like particles, like a charcoal chunk, arranged in a layered morphology with a compact but porous network. In addition to these angular features, some regions also exhibited globular structures. The interlocking nature of the plates suggests a compact but porous network, which are

favourable in facilitating ion diffusion.

ZNC 121 with higher Ni ratios compared to Zn and Co displays a similar morphology as ZNC 111, but with less layering, and a more isotropic or compact arrangement, indicating reduced anisotropic growth due to the influence of Ni, as can be seen in Figure 4.4 c). While ZNC 111 is analogous to charcoal chunk, ZNC 121 resembles ice cubes with tiny particles on it. The higher Ni ratio in ZNC 121 sample modifies the crystallization behaviour, resulting in a structure that is less layered and more isotropic or compact compared to the more balanced ZNC 111. This reflects the significant role of metal ratios in tuning material morphology.

Meanwhile, ZNC 112 shown in Figure 4.4 d) exhibits an integration of petal-like, and globular-like structures of varying sizes, clustered together, similar to the morphology reported by Prabhu *et al*., (2021). When Co content is doubled, the number of nucleation sites increase accordingly, leading to the growth of particles with varying sizes and morphologies (Jafari *et al*., 2024). This is due to the strong influence of Co elements on crystal nucleation and growth mechanisms.

In the case of ZNC 211 which can be seen in Figure 4.4 e), where the Zn content is doubled, transitions in morphology to spherical particles are evident, resembling irregular shaped cubes, consistent with the morphology reported by Jian *et al*., (2021) The formation of spherical particles can be associated with the nature of Zn ions which favour isotropic growth (Okeil *et al*., 2024). With higher Zn ratio, the relative concentrations of Ni and Co decrease concurrently. This reduced influence minimizes the tendency for anisotropic growth and formation of layered or petal-like structures which normally driven by Co and Ni. Moreover, larger cluster aggregation in ZNC 211 sample is caused by the characteristic of Zn-rich systems which are prone to form a dense, aggregated structures rather than dispersing as discrete particles.

Table 4.5
Summary of morphological comparison between various ZNC ratios

Sample	*Morphology*
ZNC 111	Layered or globular structures due to the equilibrium content between Zn, Ni, and Co ions.
ZNC 121	Compact or less-layered structures as nickel suppresses anisotropic growth.
ZNC 112	Integration of petal-like and globular-like structures, with more pronounced clustering

ZNC 211	Isotropic spherical particles with chunk-like aggregation due to the dominance of zinc in growth.

The FESEM micrograph of GNP is shown in Figure 4.5 a), which exhibit a morphology of cabbage-like layered structure. The cabbage-like morphology arises due to the unique arrangement of these layers, which grow outward in a radial or curved manner during synthesis. These layers are found to be highly stacked and compact, displaying sheet-like features. This structure is very common for GNP due to its graphitic nature (Vigneshwaran *et al*., 2020). This feature provides low surface area governed by the highly stacking and limited porosity nature, thus reduced the supercapacitive performance of standalone GNP. In Figure 4.5 b), the ZNC-GNP 0.1 sample shows a more fragmented feature compared to pure GNP. The micrograph partially retained the cabbage-like structure of GNP but starts breaking down due to the integration with ZNC matrix. Agglomeration of particles can also be observed in the figure. Apparently, GNP addition enhances the composite structure by incorporating conductive pathways within the ZNC matrix. However, the low GNP content leads to incomplete dispersion, resulting in small clusters of agglomerated GNPs within the matrix. This structure offers a slightly increased surface area compared to pure GNP, but the agglomeration limits uniformity and accessible active sites (Fu *et al*., 2022). The incomplete dispersion limits the effective surface area for charge storage, resulting to a suboptimal performance at this loading. Next, the ZNC-GNP 0.2 is shown in Figure 4.5 c), with a more crumpled, less layered, and less agglomerated compared to the ZNC-GNP 0.1 sample. Herein, the cabbage-like feature is no longer dominant, and globular particles with fine crumpled attributes are visible. In ZNC-GNP 0.2 sample, the intermediate amount of GNP added allows better dispersion within the ZNC network. Furthermore, it reduces the likelihood of particle clustering thus ensure effective integration between GNP and the ZNC matrix. The crumpled morphology implies that the calcination at 350 °C enables partial breakdown of the initial layered structure of GNP, hence improving porosity and surface roughness. This structure reflects an increased specific surface area and electroactive sites that is favourable for charge storage application. Meanwhile, Figure 4.5 d) shows the FESEM micrograph of ZNC-

GNP 0.3 sample with more aggregated and disordered structure. While fragments of crumpled attributes remain, greater amount of GNP addition causes clumping of particles and reduces uniformity. GNP overloading prompted particle agglomeration which then hinder the formation of a well-integrated composite structure and lower amount of accessible active sites for electrochemical reaction to occur (Low *et al*., 2019). Hence, from morphology point of view, ZNC-GNP 0.2 with less agglomeration, improved dispersion, and crumpled feature exhibit the most favourable structure suitable for energy storage application.

Table 4.6
Summary of morphological comparison between GNP and various ZNC-GNP ratios

Sample	*Morphology*
GNP	Cabbage-like layered structures, compact and stacked with low surface area
ZNC-GNP 0.1	Partially broken layered structures with some agglomeration which also analogous to incomplete dispersion in the ZNC matrix
ZNC-GNP 0.2	Crumpled and globular structures with improved dispersion and less agglomeration, offering higher surface area and improved morphology
ZNC-GNP 0.3	Aggregated and disordered structures with significant agglomeration, reducing SSA and the uniformity of pore distribution

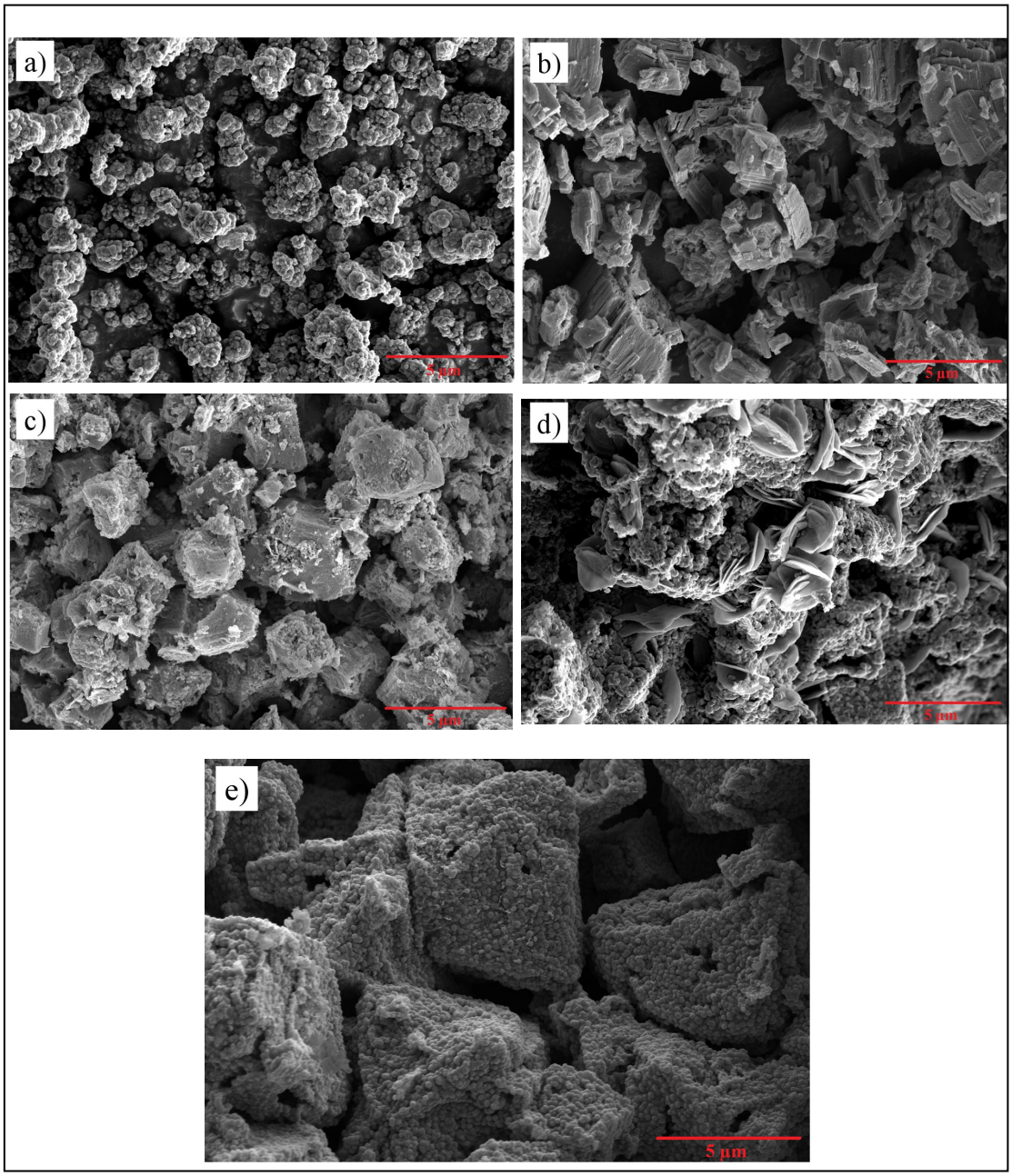

Figure 4.4 FESEM micrograph of a) ZC, b) ZNC 111, c) ZNC 121, d) ZNC 112, e) ZNC 211

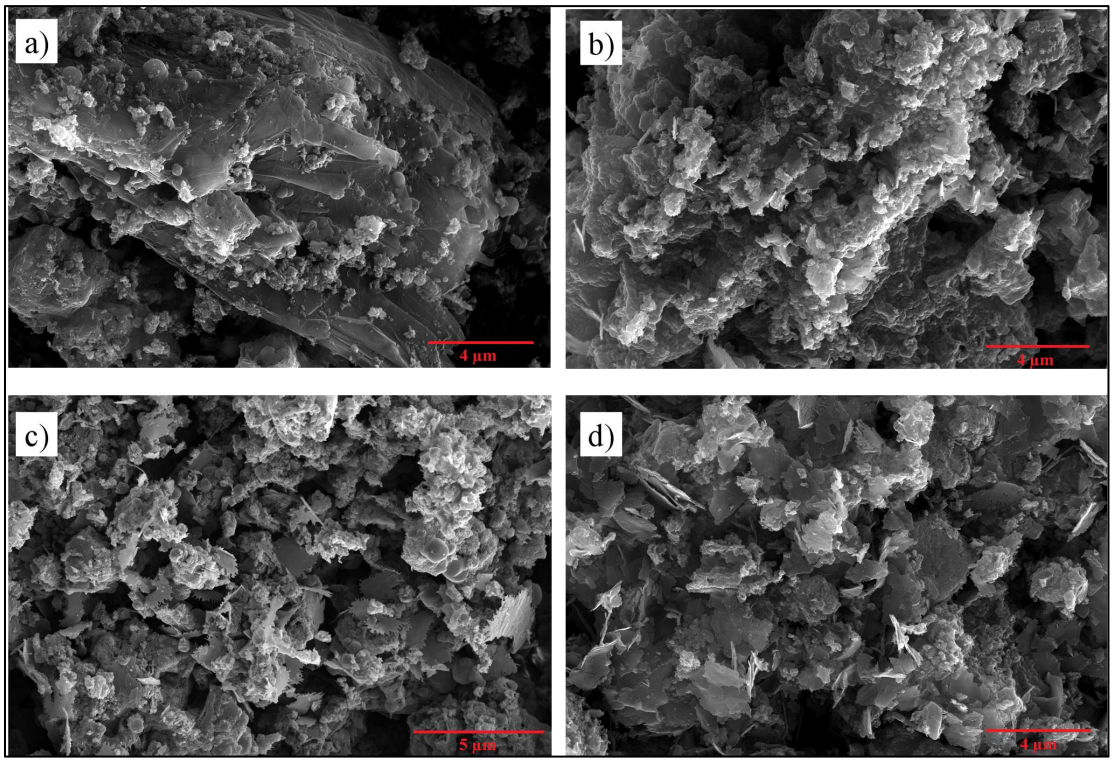

Figure 4.5 a) GNP, b) ZNC-GNP 0.1, c) ZNC-GNP 0.2, and d) ZNC-GNP 0.3 at 20000x magnification

The EDX spectra of various ZNC ratios and ZNC-GNP samples are presented in figure 4.6 a) to g). The spectra shown in 4.6 a) is intended for Zn: Ni: Co ratio of 1:1:1, and the calculated relative-to-smallest ratio from atomic percentages is calculated to be 1.156:1.957:1.000 (Co = 1). This shows that Ni content is noticeably higher than Zn and Co, suggesting a deviation from the target stoichiometry. Nevertheless, Zn, Ni, and Co remain the dominant elements, with oxygen originating from the oxide matrix and residual nitrates decomposed during calcination. The slight imbalanced composition may still support isotropic growth, producing morphologies such as globular or interconnected structures, consistent with the FESEM observations. Mass percentages in the EDX composition table are influenced by differences in atomic masses, hence some discrepancy from ideal ratios is expected.

The composition of ZNC 121 shown in Figure 4.5 b) reflects higher Ni content and comparable Zn and Co content, but lower percentage compared to Ni. the intended Zn: Ni: Co ratio was 1:2:1, and the calculated value is 1.038:2.031:1.000 (Co = 1), which closely matches the design. The higher Ni ratio supports structural densification, reducing the layered or globular features observed in ZNC 111. Instead, ZNC 121 displays a denser, more compact morphology, consistent with the FESEM

micrograph as shown on Figure 4.4 c).

In ZNC 112 sample as seen in Figure 4.6 c), the expected composition outcome shown by the EDX spectrum is mainly dominated by Co, with twice the amount of Co compared to Zn and Ni. Evident from the result, the calculated ratio is found to be 1.000:1.133:2.386 (Zn = 1). While Co is indeed the dominant element as intended, the measured content suggests a slightly deviation of Co fraction. Herein, the higher Co content promotes anisotropic growth, leading to a unique morphology combining petal-like and globular structures. The petal-like morphology is comparably to the morphology obtained by Prabhu *et al*., (2021). The flower-like morphology facilitates ion transport pathways and exposes abundant electrochemically active sites, which can contribute to the high Cs value measured for this sample.

The final composition for the synthesized Zn-Ni-Co MTMOs in this work is ZNC 211 sample, with doubled Zn content and similar Ni and Co composition. The expected outcome of Zn dominating the EDX spectrum is visible in Figure 4.6 d). The calculated ratio is 1.891:1.156:1.000 (Co = 1), which is acceptably close to the intended composition. The increased Zn content leads to the formation of spherical particles that clustered together in chunk-like morphologies. This behaviour aligns with the preference of Zn for isotropic growth. While the specific surface area may be slightly reduced due to the clustering, the uniform distribution still permits good electrochemical performance.

The EDX spectrum of ZNC-GNP 0.1, ZNC-GNP 0.2, and ZNC-GNP 0.3 is presented in Figure 4.6 e), 4.6 f), and 4.6 g), respectively. In all ZNC-GNP samples, the weight percentage for ZNC matrix is according to the precursor weight prepared for ZNC 112 sample. Hence, it is expected that the Zn: Ni: Co ratio resembles the ZNC 112 sample shown in Figure 4.6 c). Zn: Ni: Co molar ratio of 1:1:2, which was identified during the preliminary screening stage as the composition yielding the highest specific Cs value among the other Zn-Ni-Co TMOs ratios. This cobalt-enriched ratio was therefore selected for all subsequent sample with GNP addition to ensure consistent comparison while maximizing electrochemical performance potential.

It is also evident that the ZNC matrix remains dominant, even after the

incorporation of GNP. As depicted from the EDX spectra, the atomic percentage of carbon increased as GNP addition increased from Figure 4.6 e) to g) and maintain the optimal metal oxide stoichiometry. This approach ensured that any observed differences in elemental composition and subsequent electrochemical behaviour could be attributed primarily to the GNP content, rather than variations in the underlying TMO ratios. In summary, EDX analysis confirmed the presence of Zn, Ni, and Co in all samples, with atomic compositions closely matching the targeted stoichiometry. Slight deviations from the theoretical ratio were observed, which are likely due to localized compositional heterogeneity arising from nanoscale dispersion effects and interactions between GNP and TMO particles during synthesis. Interestingly, increasing GNP loading did not significantly alter the overall Zn: Ni: Co ratio, indicating that the synthesis protocol preserved the bulk composition effectively, despite the carbon incorporation. Such minor variations in surface elemental distribution are consistent with literature reports for TMO–carbon composites, where they can positively influence electrochemical performance by providing enriched active sites and facilitating electron transport pathways (Mandal *et al*. 2025). Thus, the stability of the elemental ratio across all samples demonstrates the robustness of the synthesis process while enabling the intended evaluation of GNP's role in the composite system.

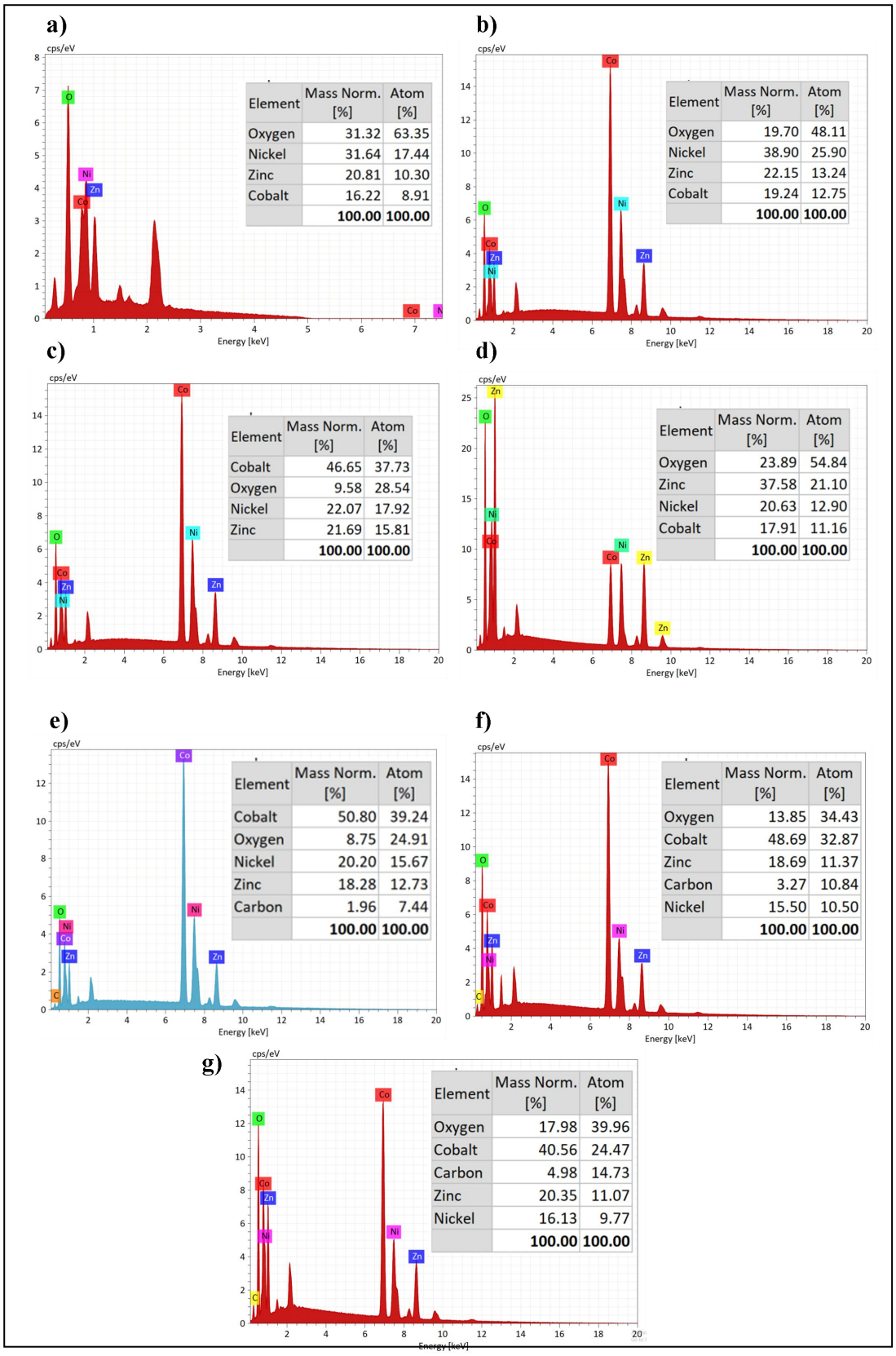

Figure 4.6 EDX spectra of a) ZNC 111, b) ZNC 121, c) ZNC 112, d) ZNC 211, e) ZNC-GNP 0.1, f) ZNC-GNP 0.2, and g) ZNC-GNP 0.3

4.2.2 Functional Group

FTIR provides an efficient way to determine the presence of functional groups in a synthesized compound. Figure 4.7 displays the FTIR spectra of various ZNC samples while figure 4.8 corresponds to FTIR spectra for ZNC-GNP samples with three different GNP loading.

In a typical ZNC-GNP matrix which integrates metal-carbon composites, the key FTIR peaks and functional groups are absorption near 3400 cm^{-1}, the bands around 1600 cm^{-1}, and the peaks between 500–800 cm^{-1}. The broad absorption appeared near 3400 cm^{-1} is associated to O-H stretching vibration, implying the presence of adsorbed water on the surface of the material (Vigneshwaran *et al*., 2020). It appears that as the GNP addition increased, the intensity of the band reduced. This is an indication of reduced surface hydroxylation as a result of GNP addition. Furthermore, the band presents at around 1600 cm^{-1} is associated to the aromatic C=C stretching vibrations, owing to the sp^2 hybridization (Babu *et al*., 2023). The peaks appeared between 500-800 cm^{-1} can be assigned to metal-oxygen (M-O) stretching vibration arising from the Zn-O, Ni-O or Co-O interactions. The varying intensity of these peaks suggested changes in the crystalline structure or interaction between GNPs and the MTMOs.

From a supercapacitor application perspective, FTIR analysis is significant as it provides insight into the nature and stability of surface functional groups, which directly influence electrochemical behaviour. Surface hydroxyl groups, for instance, can enhance pseudocapacitive reactions through faradaic redox processes, while aromatic C=C structures in the carbon matrix facilitate high electrical conductivity, essential for fast charge–discharge cycles (Ramli *et al*. 2024). Additionally, the presence and bonding nature of metal–oxygen frameworks can indicate potential active sites for redox reactions, contributing to higher specific capacitance. Therefore, the observed reduction in surface hydroxylation with increasing GNP content, along with the retained conductive carbon structures and M–O bonding, implies a potential optimization balance between conductivity and active site availability for supercapacitor performance.

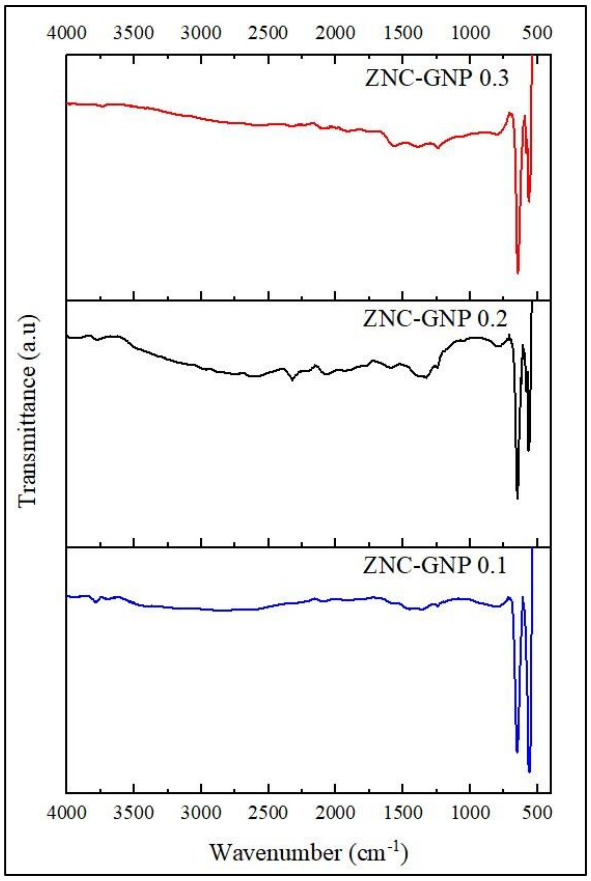

Figure 4.7 FTIR spectra of ZNC-GNP at three different GNP loading

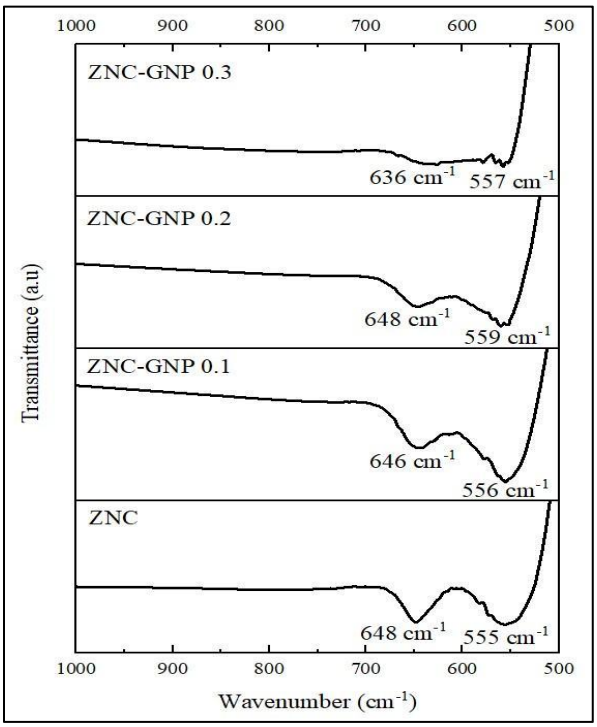

Figure 4.8 FTIR spectra of ZNC and ZNC-GNP samples

4.2.3 Specific Surface Area and Pore Size Analysis

BET analysis through N_2 adsorption/ desorption isotherm experiment was performed to elucidate the specific surface area (SSA) and pore size distribution of ZNC with and without GNP addition. These properties play a crucial role in enhancing the overall electrochemical performance of the material. The ZNC samples with four different Zn: Ni: Co ratios are shown in Figure 4.9. From the experiment, it has been deduced that the SSA value of ZNC 111, ZNC 121, ZNC 112, and ZNC 211 are found to be 51.68, 84.55, 31.76, and 67.60 m^2/g, respectively as shown in table 4.6 Of all four ratios, the SSA value of ZNC 121 is the highest followed by ZNC 211, ZNC 111 and finally the ZNC 112 sample. These values are comparable to the surface area reported by Kumar *et al*., (2021), in which the synthesized Zn-Ni-Co-O nanorods possessed an approximately 56 m^2/g of SSA value.

ZNC 121 sample has higher Ni^{2+} ion content incorporated into the MTMO matrix. Higher nickel content is probable of creating lattice strain hence resulted in more defects or dislocations in the crystal structure due to its smaller ionic radii nature. This will then contribute to a greater available SSA by creating small and porous grains. Moreover, NiO can resist sintering especially when it is combined with other metal oxides thus preventing the particles from coalescing into larger grains, hence producing small particle size sample. Apart from that, a reduction in grain size leads to the formation of nanostructured materials with a significantly larger SSA, which increases the number of accessible electroactive sites for charge storage. This enhances both EDLC and pseudocapacitive activity. This result is also congruent with the crystallite size data presented in Table 4.2. Minimal agglomeration is also evident from the FESEM data, also contributed to the higher SSA value. In a typical MTMO systems, NiO can act as a stabilizer that prevents excessive grain growth of both ZnO and Co_3O_4 hence contributed to a greater SSA. On the other hand, Zn^{2+}, Co^{2+} with larger ionic radii can promote lattice relaxation which then resulted to the formation of larger particle sizes and less compact structure. This also increased the chances for the formation of more open structures, thus enhancing the grain growth and reduce the SSA.

The pore size distributions were calculated from N_2 desorption isotherm data with BJH model, as shown in Figure 4.10. The maxima for ZNC 111, ZNC 121, ZNC

112, and ZNC 211 are found to be approximately at 10.71, 7.42, 3.34, and 10.71 nm, respectively. Both ZNC 111 and 211 shows similar pore distribution maxima. This suggests that the largest amount of pore volume distributed in ZNC 111 samples stays the same even after the ratio of Zn is doubled in the composites. It is likely that both samples have similar pore formation mechanisms due to the stabilizing effect of zinc, which leads to the same pore size maxima. On the other hand, ZNC 121 with richer nickel content and ZNC 112 sample with more cobalt content may have denser structures smaller pores, thus resulted to a lower maxima value. Overall, the results indicates that the pore size distribution is paramount in ensuring effective ion diffusion during charge-discharge cycles. Combination of both mesopores and macropores are proven to be beneficial in boosting the capacitance value of a material. Also, micropores alone may hinder ion movement and resulted to a lower capacitance, despite having high SSA (Abdul *et al*., 2021). The relationship between specific surface area (SSA), pore structure, and capacitance is complex. Despite having lower SSA and smaller pore size distribution maxima, the cobalt-rich samples exhibit higher Cs values. Xie *et al*. (2020) justifies that variations in material morphology can significantly influence electrochemical performance, even when the corresponding SSA values are not the highest. This is due to faradaic reactions originating from their redox-active properties, which will be discussed in detail in the cyclic voltammetry analysis.

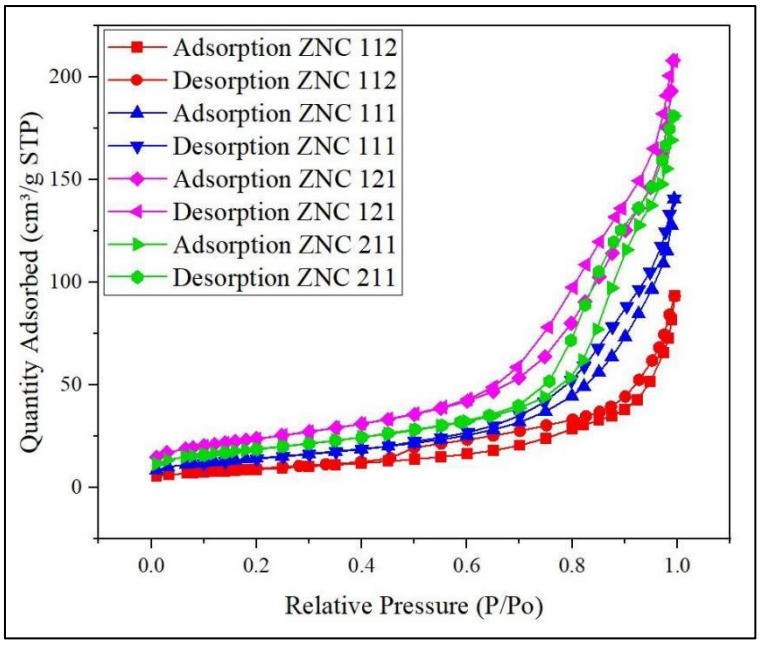

Figure 4.9 N_2 adsorption/desorption isotherm of various ZNC samples

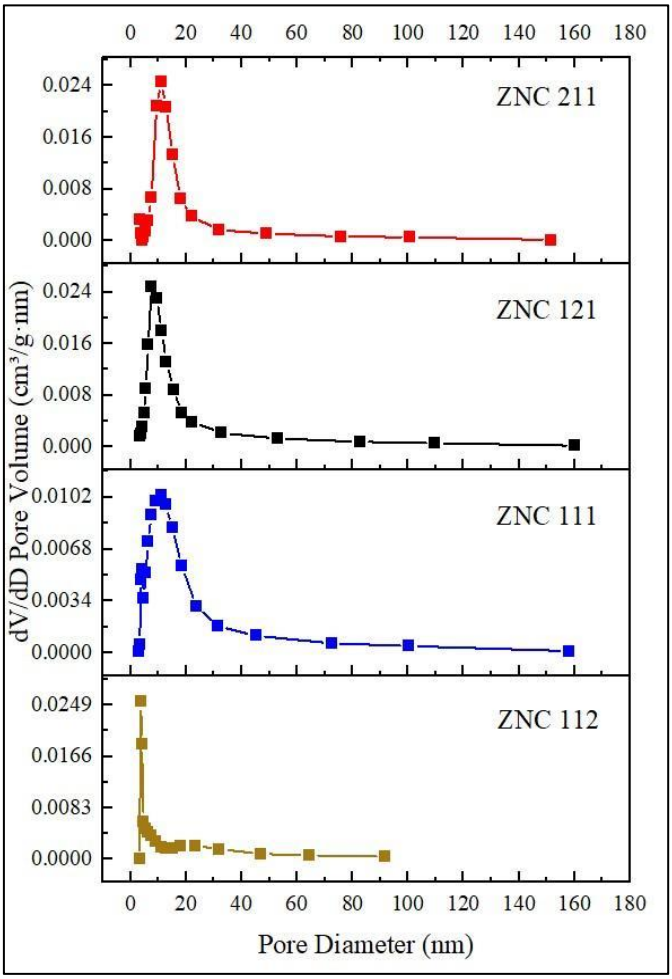

Figure 4.10 Pore distribution desorption data of various ZNC samples using the BJH model

Table 4.7
The specific surface area and pore diameter of various ZNC and ZNC-GNP samples

Sample	Specific surface area (m^2/g)	BJH desorption pore diameter (nm)
ZNC 111	51.68	14.03
ZNC 121	85.55	10.93
ZNC 112	31.76	12.64
ZNC 211	67.60	14.02
ZNC-GNP 0.1	50.67	14.10
ZNC-GNP 0.2	64.84	13.36
ZNC-GNP 0.3	55.53	14.02

Figure 4.11 displays the N_2 adsorption/desorption isotherm of ZNC and various ZNC-GNP samples. Evident from the graphs, the ZNC and ZNC-GNP samples exhibits a Type IV isotherm with a H3 hysteresis loop, which according to IUPAC is the characteristic feature of mesoporous materials with a pore size between 2 and 50 nm (Polat & Faris, 2022). The SSA values calculated from the isotherms were 50.67, 64.84, and 55.53 m^2/g, respectively as displayed in Table 4.6 Polat & Faris (2022) reported SSA values for GNP-based composites ranging from 38.4 m^2/g to 76.7 m^2/g, which is in agreement with the values obtained in this work. Compared to ZNC 112 sample, all three ZNC-GNP samples show an improved SSA values when GNP was incorporated into the bare ZNC matrices. When only a small amount of GNP is added, the overall contribution of the GNP to the surface area will be minimal. GNP typically have a very high SSA (~2630 m^2/g for single-layer graphene), but if only a small fraction of the total material consists of GNPs, their effect on the total SSA will be limited.

The corresponding pore size distribution of the materials measured from the adsorption branches based on the BJH model in Figure 4.12 is centred at about 10– 25 nm, further indicating that the porosity mainly composed of mesopores. ZNC-GNP 0.1 and ZNC-GNP 0.3 samples exhibits two maxima, describing a multimodal pore size distribution. The average pore diameter was 14.10, 13.36, and 14.02 nm for ZNC-

GNP 0.1, ZNC-GNP 0.2, and ZNC-GNP 0.3 samples, respectively. It was determined that the average pore diameter of the ZNC-GNP samples was increased by 6-12% compared to the ZNC 112 sample (ZNC composite with highest Cs value). Apparently, increased porosity enables more efficient transport of ionic and molecular species through the material (Cochran *et al*., 2019). This ion mobility will help in boosting the Cs value of samples. Expanding pore size promotes ion transport but potentially compromises the SSA value of a material. As the pore size expands, the density of smaller pores diminishes, limiting the surface area that is accessible for adsorption processes and redox chemistry. Therefore, it is safe to say that a balance between porosity and SSA is paramount, particularly for materials used in energy storage, where a high surface area is needed to store more charge (Rosaiah *et al*., 2022).

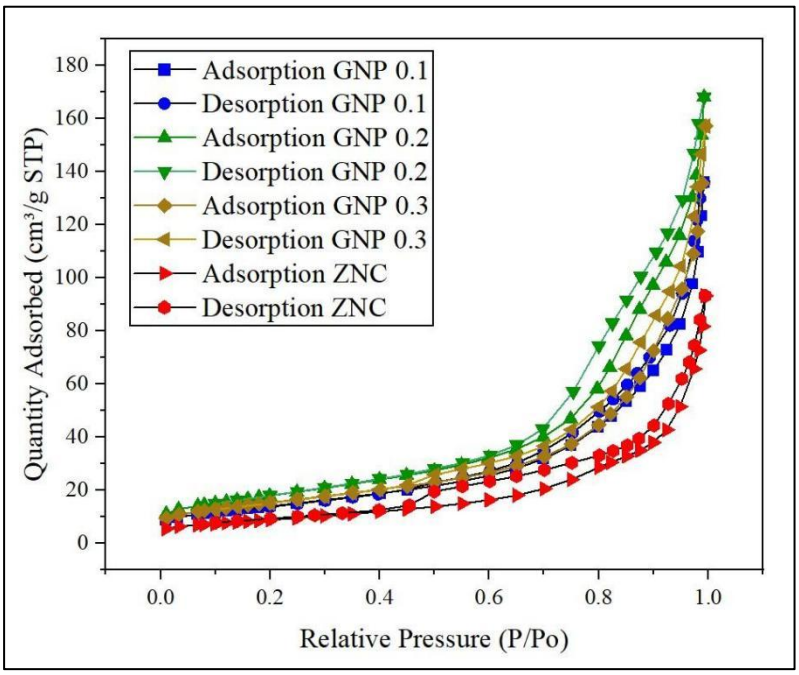

Figure 4.11 N_2 adsorption/desorption isotherm of ZNC and various ZNC-GNP samples

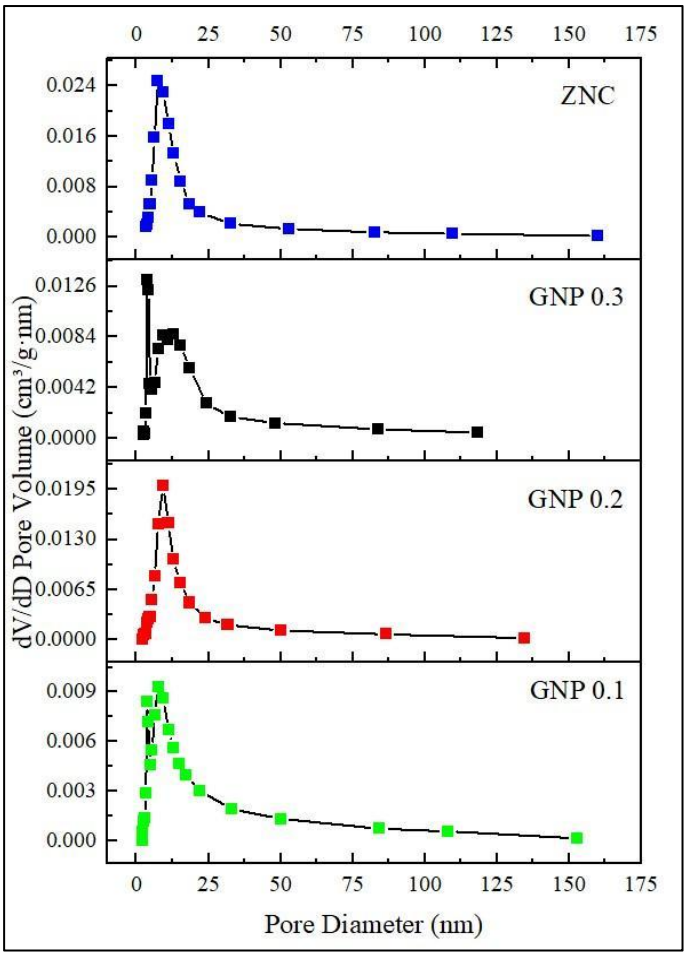

Figure 4.12 Pore distribution desorption data of ZNC and various ZNC-GNP samples using the BJH model

4.2.4 Band Gap Analysis

The characteristic bands of ZNC and ZNC-GNP sample, which correspond to absorption, are examined by UV-visible spectroscopy. Figure 4.13 and Figure 4.14 shows the Tauc plots of ZNC 112 and ZNC–GNP 0.2, obtained by converting the reflectance data into absorption values via the Kubelka–Munk (K–M) function as expressed in Equation (4.3)

$$F\,(R) = \frac{(1-R)^2}{2R} \tag{4.3}$$

where R represents the absolute reflectance value of a sample and F(R) is the Kubelka-Munk function which in proportionality with the absorption coefficient, α (Shubha & Manohara, 2020). Further, the modified Kubelka-Munk function can be

acquired by multiplying F(R) with photon energy, hv. The Tauc relation $\alpha hv = B(hv - E_g{}^{opt})^n$ then expressed in Equation (4.4) as:

$$F(R)hv \approx \alpha hv = B(hv - E_g{}^{opt})^n \quad (4.4)$$

In which B is a constant that depends on the transition probability, $E_g{}^{opt}$ represent the optical bandgap (n = ½ for direct allowed, 3/2 for direct forbidden, 2 for indirect allowed, and 3 for indirect forbidden transitions) (Shubha & Manohara, 2020). In this work, $[F(R)hv]^2$ versus hv plots were used, corresponding to a direct allowed transition (n = ½), which gave the best linear fit for both ZNC 112 and ZNC-GNP 0.2 samples.

Interpreted from the plot of $[F(R)hv]^2$ versus the photon energy (hv), there are two E_g values obtained for each graph corresponds to 1.63 and 1.7 eV for ZNC 112, while 1.58 and 1.79 eV for ZNC-GNP 0.2. The higher-energy intercept represented by the red dashed line is attributed to the fundamental band-to-band transition of the Zn-Ni-Co matrix, while the lower-energy intercept shown by the blue dashed line is assigned to the sub-bandgap absorption arising from localized states or defect levels within the bandgap. Such defect-related states can originate from oxygen vacancies, cation disorder, or interfacial electronic states at ZNC–GNP contacts (Ilyas *et al*., 2024; Majeed *et al*., 2024). Similar dual-slope behaviour has been reported for other TMOs composite and mixed-metal oxide/graphene nanocomposites, where one slope corresponds to the intrinsic transition and the other to defect or impurity-related transitions (Guo *et al*. 2014; Belkessam *et al*. 2019).

Evident from the graph, the incorporation of GNPs has reduced the lower-energy gap from 1.63 to 1.58 eV but increased the higher-energy gap from 1.70 to 1.79 eV. The bandgap narrowing is likely due to the introduction of localized electronic states near the band edges, facilitated by ZNC–GNP interactions. This also promote charge transfer and suppress electron–hole recombination (Seetharaman *et al*. 2021). The increase in the higher-energy bandgap may be associated with quantum confinement effects in smaller ZNC–GNP crystallites or strain induced by GNP incorporation, which can modify the electronic band structure. This is consistent with XRD results showing reduced crystallite size, supporting the possibility of size-induced bandgap widening.

For comparison, the bandgap value of single Co, Ni, and Zn metal oxides constituent and materials with impregnation of GNPs are presented in Table 4.8. Kate *et al*., (2018) revealed that the theoretical bandgap of CoO is 2.0 eV, higher compared to the value reported by Kaewmaraya *et al*., (2015). ZnO has slightly higher bandgap with theoretical bandgap of 3.4 eV, and the value obtained from experiment are ranging from 3.1 to 3.37 eV (Davis *et al*., 2019). The hybrid form of either two of the three metal oxides show narrower bandgap in which zinc cobaltite (2.9 eV) and nickel cobaltite (0.9 eV). Apparently, ZNC and ZNC-GNP in our work are closer to nickel cobaltite in terms of their bandgap, suggesting a similar contribution of cobalt and nickel components. On the other hand, mixed metals such as Ni-Zn O and Co-Zn-O reported to have wider bandgap, corresponds to 5.19 eV and 5.05 eV, respectively. Despite having the same type of metal contribution, the value varied based on the differences in their crystal structure, electronic interactions, and bonding environments (Saleem *et al*., 2022). Hybrid compositions such as Zn–Ni–Co oxides exhibit intermediate gaps; for example, Zn–Ni–Co thin films have been reported at 1.8 eV (Zakutayev *et al*., 2011), comparable to the value obtained in this work. The dual-gap behaviour observed here suggests that the ZNC–GNP system simultaneously exhibits intrinsic Zn–Ni–Co oxide transitions and defect-mediated transitions introduced by structural disorder and graphene incorporation.

In this work, the bandgap reduction from 1.63 eV to 1.58 eV can also be associated to structural properties of ZNC-GNP 0.2 sample which has a good dispersion, less particle clustering, and crumpled morphology as discussed in the previous sub-chapter. The integration between ZNC matrix and GNPs enhances the charge transfer and reduce the recombination rates. Hence, localized electronic states near the band gap edges is introduced, which then caused bandgap narrowing (Shubha & Manohara, 2020). Besides, more active sites are available due to the crumpled morphology of ZNC-GNP 0.2. In accordance to the crumpled morphology, higher surface interactions and defect states are evident thus contributing to the bandgap narrowing.

It is highly possible that the variation in bandgap is due to the interaction between the carbon content and the resulting structural characteristics such as the role of layer stacking and edge chirality (Ilyas *et al*., 2024). For instance, Ilyas *et al*., (2024)

presented that the bandgap energy of their Cd-Zn-Cr ferrites/GNPs nanocomposites was lowered from 4.29 eV to 4.20 eV as the GNPs content was increased from 0 wt% to 1.25 wt%. In contrast, increment beyond 1.25 wt% resulted to a wider bandgap up to 4.95 eV. In another work, Majeed *et al*., (2024) also reported a non-linear trend of bandgap values for Cu-Co-Sm ferrite sample with varying impregnation percentage of GNPs. It was found that the bandgap initially increases (from 1.45 eV to 1.87 eV) due to improved crystallinity, quantum confinement effects, and optimized structural integration of GNPs. Further GNPs addition expected to cause structural distortion and agglomeration, hence resulting to a lowered bandgap value of 1.58 eV.

Table 4.8
Bandgap energy of various reported materials

Material	*Bandgap energy (eV)*	*Reported by*
Cobalt oxide (theoretical bandgap)	1.8	(Kaewmaraya *et al.*, 2015)
Cobalt oxide	2.0	(Kate *et al*., 2018)
Zinc oxide (theoretical)	3.4	(Lacivita *et al*., 2013)
Zinc oxide	3.1 to 3.37	(Davis *et al*., 2019)
Zinc cobaltite	2.95	(Abo-Dief *et al*., 2022)
Nickel cobaltite (theoretical bandgap)	0.9	(Chang *et al*., 2021)
Ni-Zn-O	5.19	(Saleem *et al*., 2022)
Co-Zn-O	5.05	(Saleem *et al*., 2022)
Zn-Ni-Co thin film	1.8	(Zakutayev *et al*., 2011)
Ni-Zn Ferrites	1.9 to 2.8	(Thokoane *et al*., 2024)
Cu-Co-Sm ferrite impregnated with GNPs	1.45 to 1.87	(Majeed *et al*., 2024)
ZCCHF/GNPs	1.57 to 1.62	(Ur Rehman *et al*., 2024)
PEOX–PVP–GNPs	1.2	(Shubha & Manohara, 2020)
BLFMO/GNPs	1.4	(Fatima *et al*., 2017)

ZCCHF/GNPs – Zn-Co-Cu-Ho-FeO (ZCCHF)/Graphene nanoplatelets (GNPs)
PEOX–PVP–GNPs - poly(2-ethyl-2-oxazoline)– polyvinylpyrrolidone–graphene nanoplatelets
BLFMO/GNPs - lanthanum (La) and manganese (Mn) co-doped $BiFeO_3$ (BLFMO)/graphene nanoplatelets (GNPs)

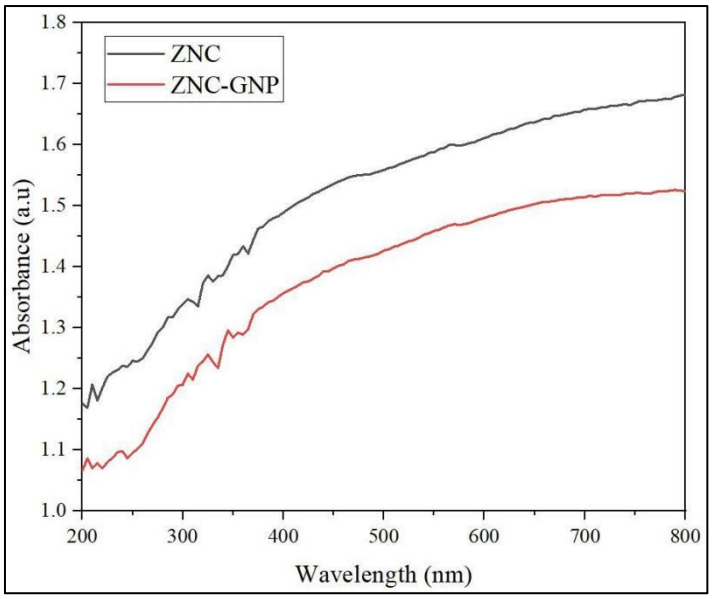

Figure 4.13 UV-Vis. spectra of ZNC and ZNC-GNP

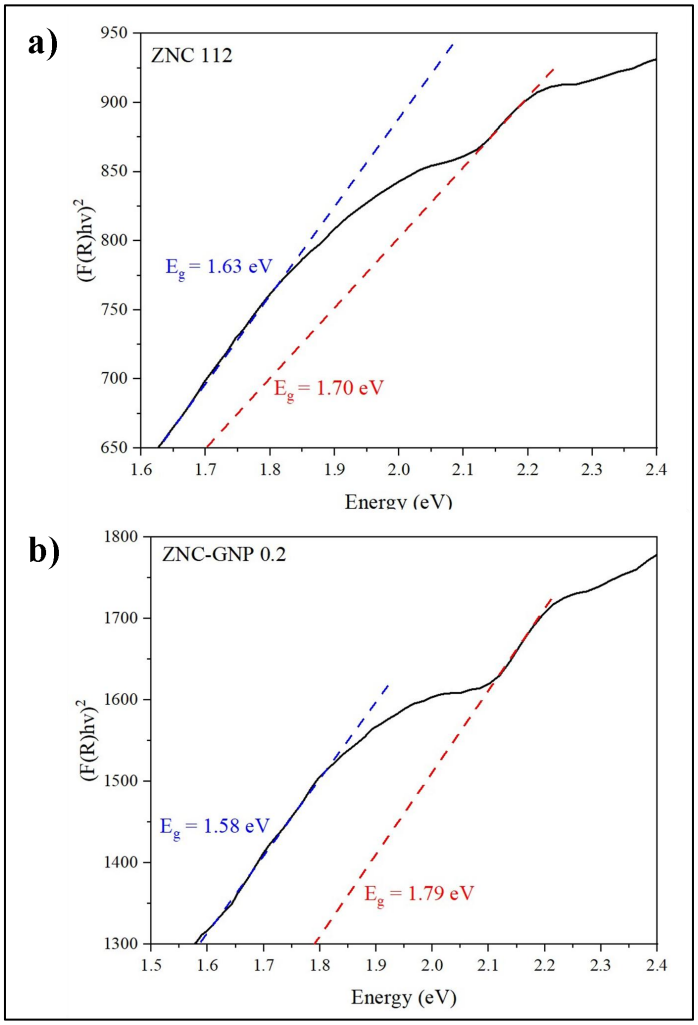

Figure 4.14 Band gap determination of a) ZNC112, and b) ZNC-GNP 0.2

4.2.5 Raman spectroscopy

Raman spectroscopy was carried out to assess the structural characteristics of ZNC-GNP samples with varying amount of incorporated GNP (0.1 g, 0.2 g, and 0.3 g). The Raman spectra of ZNC-GNP 0.1, ZNC-GNP 0.2 and ZNC-GNP 0.3 is presented in Figure 4.15. Evident from the graph, it can be seen that all samples exhibited three distinct peaks corresponding to the D band (~1350 cm^{-1}), the G band (~1580 cm^{-1}), and the 2D band (~2700 cm^{-1}), which are typical signatures of carbon-based materials (Zheling Li *et al.*, 2023). The G band originates from the in-plane vibrations of sp^2-hybridized carbon atoms. An intense peak often signifies the presence of a well-ordered graphitic structure. On the contrary, the appearance of D band is associated with the breathing modes of sp^2 atoms in rings, which caused by the presence of defects, edge sites, and disorders in the carbon lattice.

It is notable that the intensity of G band is higher compared to the D band in all three tested samples, resulting in a low I_D/I_G ration. I_D/I_G ration is often employed as an indicator of disorder (Shu *et al.*, 2020). The D/G intensity ratio for ZNC-GNP 0.1, ZNC-GNP 0.2, and ZNC-GNP 0.3 are calculated to be 0.878, 0.458, and 0.409, respectively. The values obtained are slightly higher compared to the value of previously reported well-defined pure GNP which found to be 0.18 (Albetran, 2020). Minimum I_D/I_G ration implies that the samples have low defect density and GNP retain its structural order after being incorporated into the ZNC structures. The value obtained are relatively low compared to many conventional metal-carbon composites, which often exhibit higher I_D/I_G ($\geq$1.0) due to the introduction of defect during the synthesis process or harsh processing conditions. The significantly low I_D/I_G values in this system can be explained by the unique interaction between the GNPs and the Zn-Ni-Co ternary MTMO matrix. Firstly, the starting matrix of Zn-Ni-Co is inherently a non-carbon-based structure with no intrinsic Raman-active carbon bands thus causing the introduction of GNP serves as the primary source of Raman-active carbon features.

In this work, the increasing intensity of the G and 2D bands with higher GNP content confirms the successful integration of graphitic carbon. The 2D band, a second-order two-phonon process sensitive to the stacking order and number of graphene layers, became more pronounced in the 0.2 g and 0.3 g samples. This suggests that multilayered graphene-like structures were well preserved and

contributed to the electronic conductivity network within the composite.

From an electrochemical standpoint, the low I_D/I_G ratio indicates minimal disruption to the sp^2 domains of the GNPs, which is advantageous for supercapacitor applications (Wang *et al.*, 2019). The intact graphitic structure facilitates rapid electron transport and enhances the electrical conductivity of the electrode material. Simultaneously, the ZNC matrix provides pseudocapacitive behaviour through Faradaic redox reactions, while the GNP contribute to double-layer capacitance and act as a conductive backbone, forming a synergistic hybrid system. Collectively, the Raman spectra indicate that the structural quality of GNP remained high despite their incorporation into a metal oxide matrix. The consistently low I_D/I_G ratio across all samples reflects minimal defect formation and confirms that the processing conditions were favourable to maintaining graphitic order. This structural integrity is expected to positively influence electrochemical performance by enabling efficient charge transport and ensuring stable capacitive behaviour, making the ZNC-GNP composites promising candidates for high-performance supercapacitor electrodes.

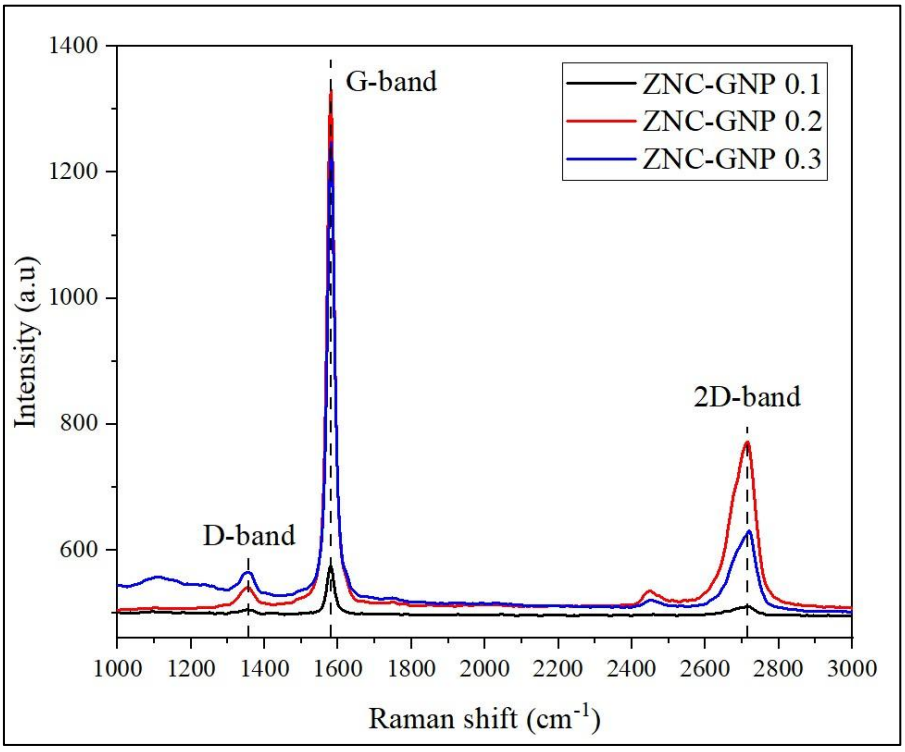

Figure 4.15 Raman spectra of ZNC-GNP 0.1, ZNC-GNP 0.2, and ZNC-GNP 0.3

4.3 Determining the Supercapacitor Performance of Zn-Ni-Co MTMOs at Various Compositing Ratios

One of the crucial outputs from cyclic voltammetry (CV) analysis is the leaf-shaped curve, a hallmark of faradaic and capacitive behaviour in electrode materials. The Cs value of ZNC materials computed from such CV data, plays a vital role in discovering whether the materials are acceptable for energy storage applications. The key factors that affecting the Cs values are inclusive of scan rate, electrolyte type, and the morphology of the electrode material (Ahmad *et al.*, 2024). In this work, the study was performed via three electrode system at 5 to 100 mVs^{-1} in 2 M KOH electrolyte. In this work, the three electrodes configuration was employed due to its reliability in providing more accurate measurements of electrode properties, as it isolates the behaviour of the working electrode from the influence of the counter and reference electrodes. Moreover, the use of 2 M KOH as the electrolyte is expected to have a pivotal contribution in enhancing the ionic conductivity and rapid charge transfer, which is essential for achieving a good electrochemical performance, as mentioned in literature review section 2.3. The alkaline environment also supports fast redox reactions, especially for electrode materials that exhibit pseudocapacitive behaviour.

4.3.1 Specific Capacitance of Zn-Ni-Co MTMOs at different stoichiometric ratio

The CV curves of ZNC at 50 mVs^{-1} with various composition ratio is presented in Figure 4.16. The screening process in determining the best ZNC ratio was done by employing the CV analysis at 20 mVs^{-1}. Evident from the CV profiles shown, it reveals that ZNC 112 sample exhibits the largest enclosed area under the curve, which analogous to the highest charge storage performance, followed by ZNC 211, ZNC 111 and ZNC 121 which displays the smallest area, congruent to the lowest Cs value out of the four samples. Despite having the same metal oxides (Zn, Ni, and Co) in the composites, the varying amounts of each metal type unveil a different redox activity and ion accessibility (Shehzad & Abdul Karim, 2023). The synergistic effects of Zn, Ni, and Co affect the number of available active sites, electron conductivity, and electrolyte diffusion within the composite. This variability explains the differences in

Cs value obtained among the samples. The synergy arises from the complementary roles of each metal oxide in contributing to charge storage (Zhongchun Li *et al*., 2021). The calculated Cs value of each ZNC compositions is presented in Table 4.9.

Compared with the literature data stated in Table 4.9, Zn–Ni bimetallic MOF reported by Zhu *et al*. (2022) shows a higher Cs value of 466.50 F g^{-1} at 0.5 A g^{-1} in 3 M KOH, while NiAl-LDH (368.00 F g^{-1}) also surpasses most of this work's samples. In contrast, CoAl-LDH (243.00 F g^{-1}) and ZnAl-LDH (132.00 F g^{-1}) reported by Parsapour *et al*. (2023) show lower values than all ZNC samples in this study. It is important to note, however, that a higher reported Cs value does not necessarily imply superior material performance, as the values are obtained under different measurement conditions and techniques. In this work, the specific capacitance values were derived from CV measurements at a scan rate of 20 mV s^{-1}, whereas Zhu *et al.* (2022) obtained their values from GCD tests at 0.5 A g^{-1}. Since CV and GCD techniques involve distinct electrochemical processes, scan rates or current densities, and calculation approaches, direct numerical comparison may not accurately reflect the intrinsic material superiority.

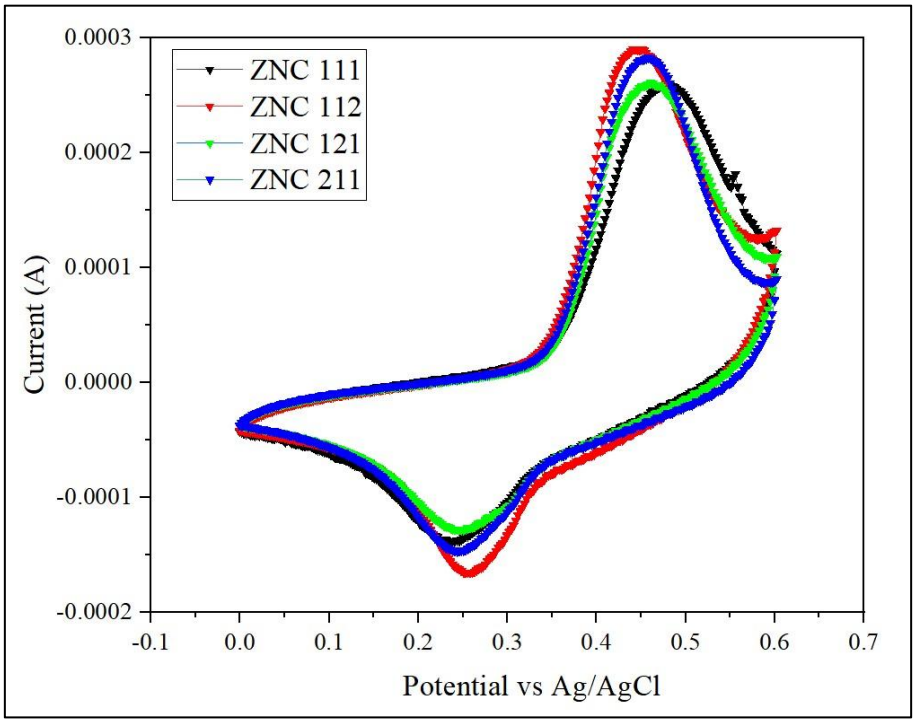

Figure 4.16 CV curves of ZNC 111, ZNC 121, ZNC 112, and ZNC 211

Table 4.9
Specific capacitance of various ZNC samples obtained in this work and comparison with other reported works

Samples	Specific capacitance, Cs (Fg^{-1})	Scan rate or Current density	Electrolyte	Reported by
ZNC 111	318.41	20 mVs^{-1}	2 M KOH	This work
ZNC 121	306.69			
ZNC 112	345.47			
ZNC 211	324.57			
Zn-Ni bimetallic MOF	466.50	0.5 Ag^{-1}	3 M KOH	(Zhu *et al*. 2022)
NiAl-LDH	368.00	2.5 Ag^{-1}		(Parsapour *et al*. 2023)
CoAl-LDH	243.00			
ZnAl-LDH	132.00			

Figure 4.17 shows the CV profiles of ZNC 112 samples at varying scan rates ranging from 5 mVs^{-1} to 100 mVs^{-1}. From the figure, a more distinct redox peak can be seen at lower scan rates. As the scan rates increases, the peaks become less prominent and broader. The reasoning behind these trends is because ions have ample time to diffuse into the material at lower scan rates, allowing for better utilization of the electrode's active sites. At higher scan rates, the rapid reactions limit ion diffusion, causing the ions to interact primarily at the surface. As a result, the redox peaks become less obvious at higher scan rates. This also explains the Cs trends, which is higher at lower scan rates with 429.04 Fg^{-1} at 5 mVs^{-1} and the lowest at 100 mVs^{-1} (165.57 Fg^{-1}). This also reflects the same reasoning of why redox peaks are more apparent at lower scan rates. It clarifies that better utilization of active sites and extensive pore accessibility are likely to happen at lower scan rates compared to higher scan rates (Hsu & Hu, 2013). This emphasizes that ion diffusion and redox activity are very crucial in controlling the supercapacitive performance of a material (Sahoo *et al*., 2023).

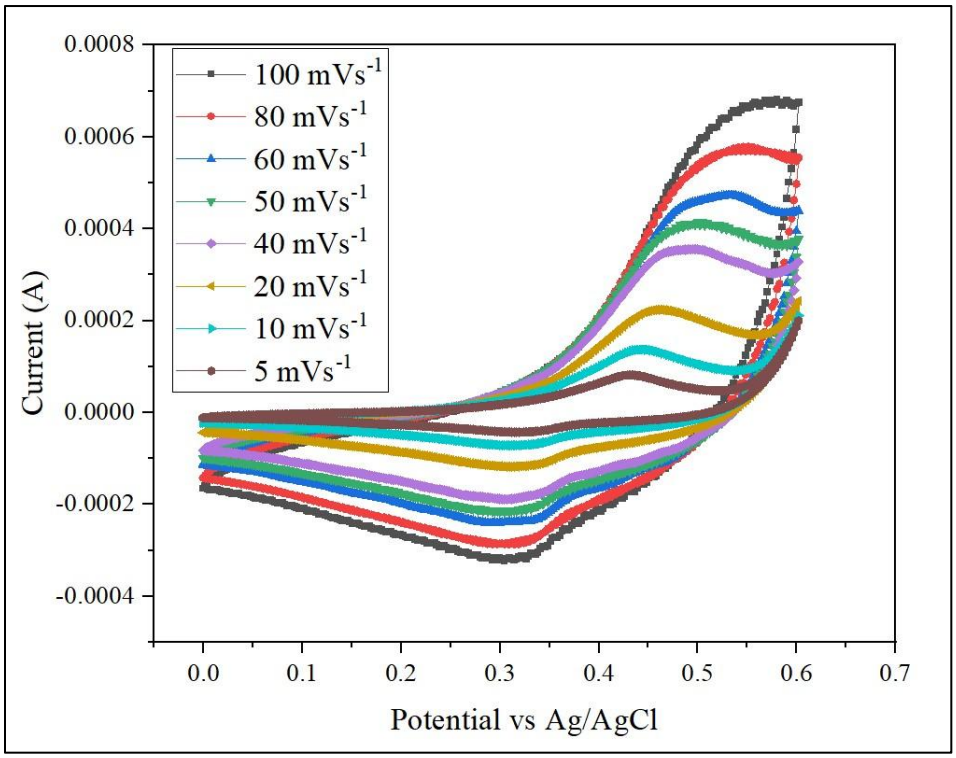

Figure 4.17 CV curves of ZNC 112 at various scan rates ranging from 5 mVs^{-1} to 100 mVs^{-1}

Table 4.10
Specific capacitance of ZNC 112 sample at varying scan rates ranging from 5 to 100 mVs^{-1}

Scan rate (mVs^{-1})	Specific capacitance, Cs (Fg^{-1})
5	429.04
10	380.27
20	345.47
40	265.63
50	243.25
60	221.96
80	192.38
100	165.57

4.4 Determining the Supercapacitor Performance of Zn-Ni-Co -GNP Hybrid Composite at Various GNP wt.% Addition

With the addition of GNP, it is expected to see an advancement in terms of electrochemical behaviour of the ZNC, owing to the change in morphological feature of ZNC-GNP discussed in section 4.2. For reference, it is validated in section 4.2 that there is an improved morphology of the combined ZNC-GNP samples, especially ZNC-GNP 0.2 sample. This section will unravel the electrochemical behaviour of ZNC-GNP through three different analyses: CC, GCD, and EIS.

4.4.1 Specific Capacitance of Zn-Ni-Co/GNP at Various GNP wt.%

Figure 4.18 represents the relative CV profiles of ZNC and ZNC-GNP at three different compositions at 50 mVs^{-1}. It is evident from the graph that the CV profiles of the electrodes exhibit a comparable shape, deviating from the ideal rectangular profile characteristic of an EDLC. This deviation suggests that the overall capacitive performance of the electrodes is predominantly governed by pseudocapacitive behaviour, rather than pure double-layer capacitance.

The superior capacitive performance exhibited by the ZNC-GNP composite can be attributed to the synergistic interplay between its two constituent components, as elucidated below:

i. The capacitive behaviour of the ZNC-GNP composite arises from the combined contributions of the pseudocapacitive effect exhibited by the ternary ZNC MTMOs and the electrical double-layer capacitance (EDLC) effect associated with the GNP (Bera *et al*., 2022).

ii. The incorporation of GNP in these ZNC MTMOs composites not only promotes efficient electron transport and enhances the kinetics of ion diffusion, but it also mitigates structural changes within the composite during electrochemical reactions (Rosaiah *et al*., 2022).

iii. The outstanding performance of TMOs composite can be attributed to its mesoporous structure, which facilitates the formation of conducting pathways through the incorporation of carbonaceous material (Abdul Karim & Shehzad, 2023).

To further assess the capacitive performance of the electrodes, CV measurements for the best sample (ZNC-GNP 0.2) were conducted at various scan rates, ranging from low to high values. The obtained results are presented in Fig 4.19. As observed, the CV curves for each individual electrode maintain a consistent shape as the scan rate increases from 5 to 100 mV/s, demonstrating their excellent capacitive behaviour. This behaviour originates from the rapid diffusion of electrolyte ions into and out of the working electrodes (Khalaj *et al.*, 2021). When the scan rate increases, the redox peaks shift toward the positive and negative potentials, indicating significant resistance at the electrolyte/electrode heterojunction area. The notably enhanced performance of ZNC-GNP composite material is ascribable to the collective contribution arising from ZNC with the presence of GNP structure. The area under the CV loop indicates the Cs value, equivalent to the material's ability to store charges. It is worth noting that the hybrid ZNC-GNP possesses greater area under the loop and higher current response compared to ZNC alone. In general, the value of Cs can be estimated by employing Equation (4.5).

$$C_s = \frac{\int_{v_a}^{v_c} I\,V(dV)}{vm\,(V_c - V_a)} \tag{4.5}$$

Where Cs is the specific capacitance presented in the unit of Fg^{-1}. The numerator signifies the total area under the CV curve, V_c and V_a indicate the potential window in volts, I(V) demonstrate the response current (A), v is the potential scan rates (Vs^{-1}), and m is the mass of sample drop-casted on the tip of the electrode (g).

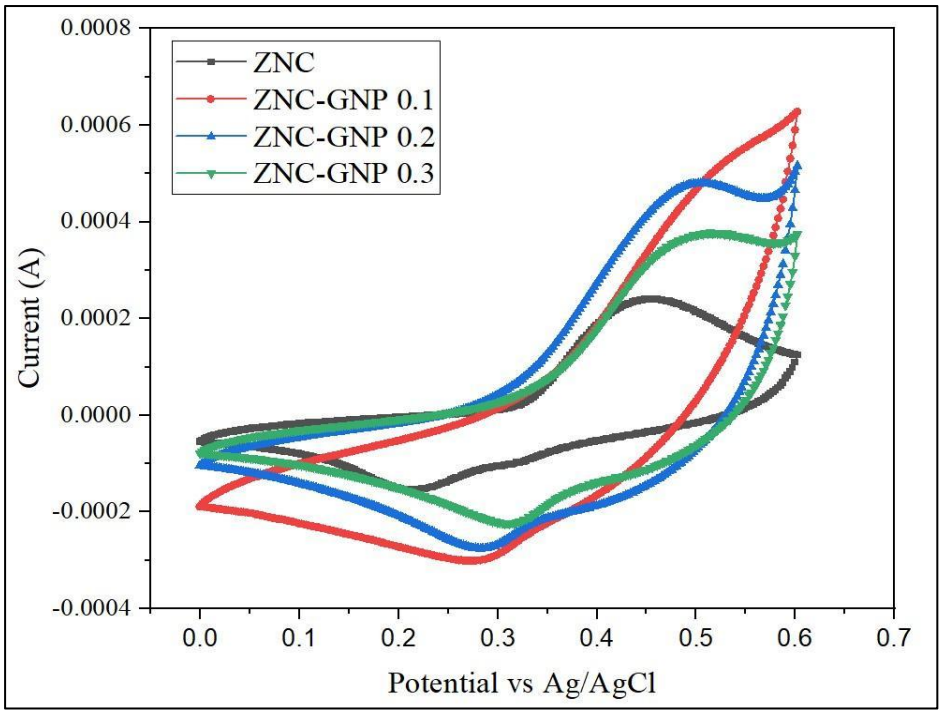

Figure 4.18 CV curves of ZNC and various ZNC-GNP samples at 50 mVs^{-1}

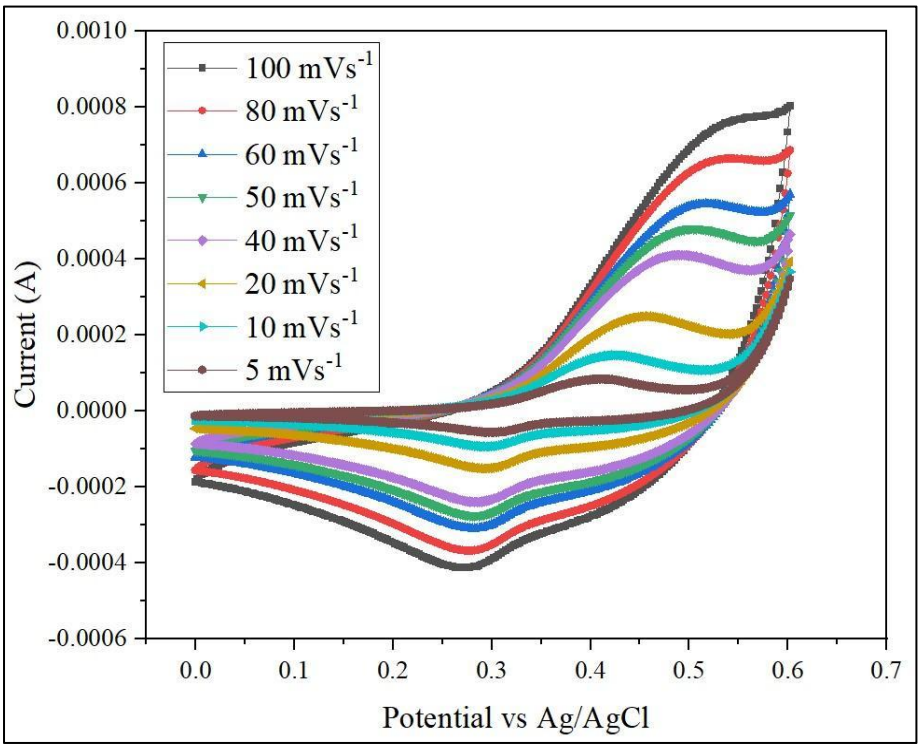

Figure 4.19 CV curves of ZNC-GNP 0.2 at various scan rates (5 to 100 mVs^{-1})

Table 4.11
Specific capacitance of various ZNC-GNP samples obtained in this work and comparison with other reported works

Samples	Specific capacitance, Cs (Fg^{-1})	San rate or Current density	Electrolyte	Reported by
ZNC-GNP 0.1	258.35	50 mVs^{-1}	2 M KOH	This work
ZNC-GNP 0.2	478.10	5 mVs^{-1}		
ZNC-GNP 0.2	428.41	10 mVs^{-1}		
ZNC-GNP 0.2	372.51	20 mVs^{-1}		
ZNC-GNP 0.2	308.60	40 mVs^{-1}		
ZNC-GNP 0.2	285.47	50 mVs^{-1}		
ZNC-GNP 0.2	266.48	60 mVs^{-1}		
ZNC-GNP 0.2	235.58	80 mVs^{-1}		
ZNC-GNP 0.2	209.13	100 mVs^{-1}		
ZNC-GNP 0.3	220.87	50 mVs^{-1}		
Nitrogen/Phosphorus co-doped mesoporous carbon	392.00	-	6 M KOH	(Xin *et al.*, 2020)
Hierarchical order porous carbon	289	0.5 Ag^{-1}	6 M KOH	(Bai *et al.*, 2020)
ZnCoO-Graphene	711	1 Ag^{-1}	2 M KOH	(Yu *et al.*, 2020)

4.4.2 Energy and Power Density of Zn-Ni-Co/GNP at Various GNP wt%

Apart from CV, GCD analysis is another essential test to unveil the supercapacitive ability of material. The GCD curves for ZNC, and ZNC-GNP at various GNP ratios is displayed in Figure 4.20, whilst the curves of ZNC-GNP 0.2 at

various current densities is presented in the next graph, Figure 4.21. During the charging process, ideal SCs will show a linear increase in voltage with time, with no voltage drop during charge or discharge, resulting in a perfectly symmetrical and linear charge-discharge cycle. Consequently, the voltage decreases linearly during the discharging process and the discharge curve is expected to mirror the charge curve, forming another sloped line on the voltage-time graph. However, in real-world SCs, there are factors such as internal resistance and undesired capacitance that may cause deviations from its ideal form, resulting in some nonlinearity and voltage drops. The Cs values calculated from GCD are estimated via the following equation presented in Equation (4.6):

$$C_s = \frac{I \times \Delta t}{m \times \Delta V} \tag{4.6}$$

In which, I (A) signify the charging current, the discharge time represented by Δt in the unit of seconds (s), the drop casted-sample's mass denotes as m (g), whilst ΔV symbolizes the potential range.

By employing Equation 4.5, the calculated Cs values for ZNC, ZNC-GNP 0.1, ZNC-GNP 0.2, and ZNC-GNP 0.3 are 52.73, 104.55, 243.64, and 147.27 Fg^{-1}, respectively at current density of 1 Ag^{-1}. Although the Cs values obtained from GCD and CV measurements are not identical, their trends closely resemble each other. ZNC-GNP 0.2 shows the highest capability in storing energy which analogous to higher Cs values, compared to the other two samples (ZNC-GNP 0.1 and ZNC-GNP 0.3).

Apart from Cs value, another vital parameter to determine the practical performance of supercapacitor material are energy density, E (Wh/kg) and power density, P (W/kg). Equation (4.7) and (4.8) indicates the equation for energy density and power density, respectively:

$$E = \frac{1}{2} CV^2 \tag{4.7}$$

$$P = \frac{E}{\Delta t} \tag{4.8}$$

Equation 4.7 demonstrates that energy density is directly proportional to the

square of the voltage window and the capacitance. Therefore, increasing the operating potential range or enhancing the specific capacitance of the electrode materials can effectually improve the value of E. This work uses 0.6 V potential window to ensure long term electrode stability. Choosing a greater potential window can effectively increase the capacitance, but it has also higher potentiality for irreversible capacity loss due to side reactions. A narrow potential window reduces the risk of material degradation, improving the electrode's cycling stability and lifespan. By applying Equations (4.7) and (4.8), the highest energy density achieved in this work is 24.06 Wh kg^{-1}, corresponding to a power density of 1375 W kg^{-1}. In comparison, Parsapour *et al*. (2023) reported a maximum energy density of 8.65 Wh kg^{-1} at a power density of 155.58 W kg^{-1} for nickel–aluminium layered double hydroxides (NiAl-LDH). Apart from that, compared to ternary transition metal phosphide composite, NiCoP@C reported by Mandal *et al*., (2025), they achieved an energy density of 48.30 Wh kg^{-1} at a power density of 800 W kg^{-1}. Although the NiCoP@C electrode exhibits a higher energy density, the material developed in this study demonstrates a superior balance between energy and power density, indicating its strong potential for high-rate energy storage applications.

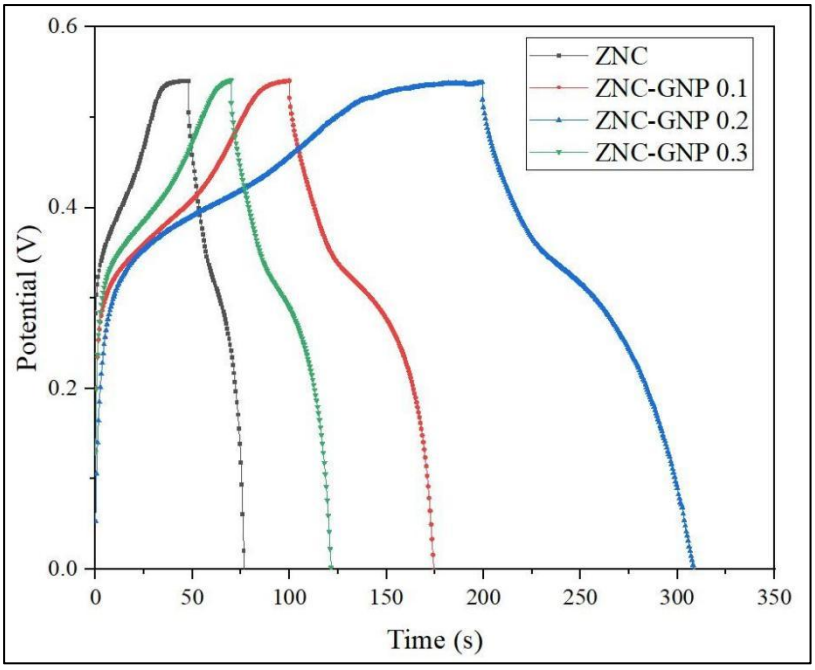

Figure 4.20 GCD curves of ZNC and various ZNC-GNP samples at 1 Ag^{-1}

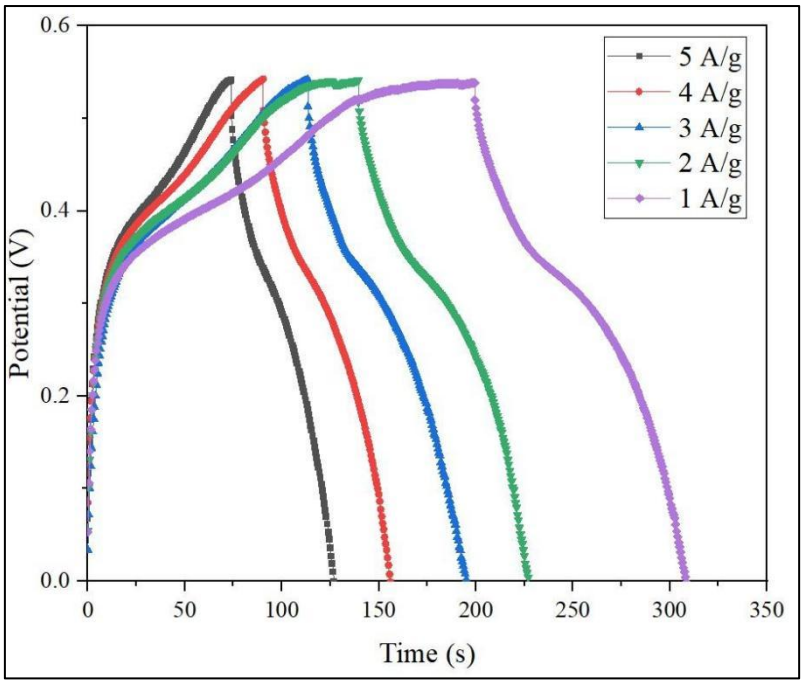

Figure 4.21 GCD curves of ZNC-GNP 0.2 at various current densities (1 to 5 Ag^{-1})

Table 4.12
Cs values obtain from GCD analysis

Current density (Ag^{-1})	*Specific capacitance, Cs (Fg^{-1})*
1	243.6364
2	369.0909
3	526.3636
4	560
5	572.7273

4.4.3 Cyclic Stability Test

Figure 4.22 a) shows the CV curves of ZNC-GNP 0.2 sample over various cycles extending up to the 1000th cycle. It is evident from the graph that the curve variation shows a minimal change in terms of shape and sizing, as the number of cycles increases. As illustrated in Figure 4.22 b), the Cs value retained 97.05% of its original value indicating robust cyclic stability. The obtained cyclic stability exhibits comparable performance to the zinc-activated carbon sample which retained 98% of its capacity upon 2000 subsequent cycles (Tekin & Topcu, 2024). Das *et al.*, (2015) reported a 92.4% of original Cs retention upon 1000 cycles for a ternary composite PANI/MoO_3/GNP. Aside from that, Xu *et al.*, (2020) reported 90.1% capacity

retention after 5000th cycles for a CoO-ZnO/rGO samples. Moreover, another work reported by Shi *et al*., (2022) discover that Ni-Co metal organic framework (MOF) hybridized with rGO has a comparable electrochemical stability with 92.51% retention after 5000 cycles. These findings highlight the potential of ZNC-GNP hybrid for long-term energy storage applications.

One of the factors that has a significant impact towards the capacity retention is the surface area of a material. Material with a higher surface area is expected to have more active sites for electrochemical reactions thus facilitates efficient ion adsorption. This contributes to improved electrochemical performance, as the electrode is capable of accommodating a greater number of charge carriers during charging/discharging process. Furthermore, optimized pore size will allow rapid charge transport and retention, reduce the ion diffusion resistance and prevent capacity degradation over prolonged cycling (Imran *et al*., 2024).

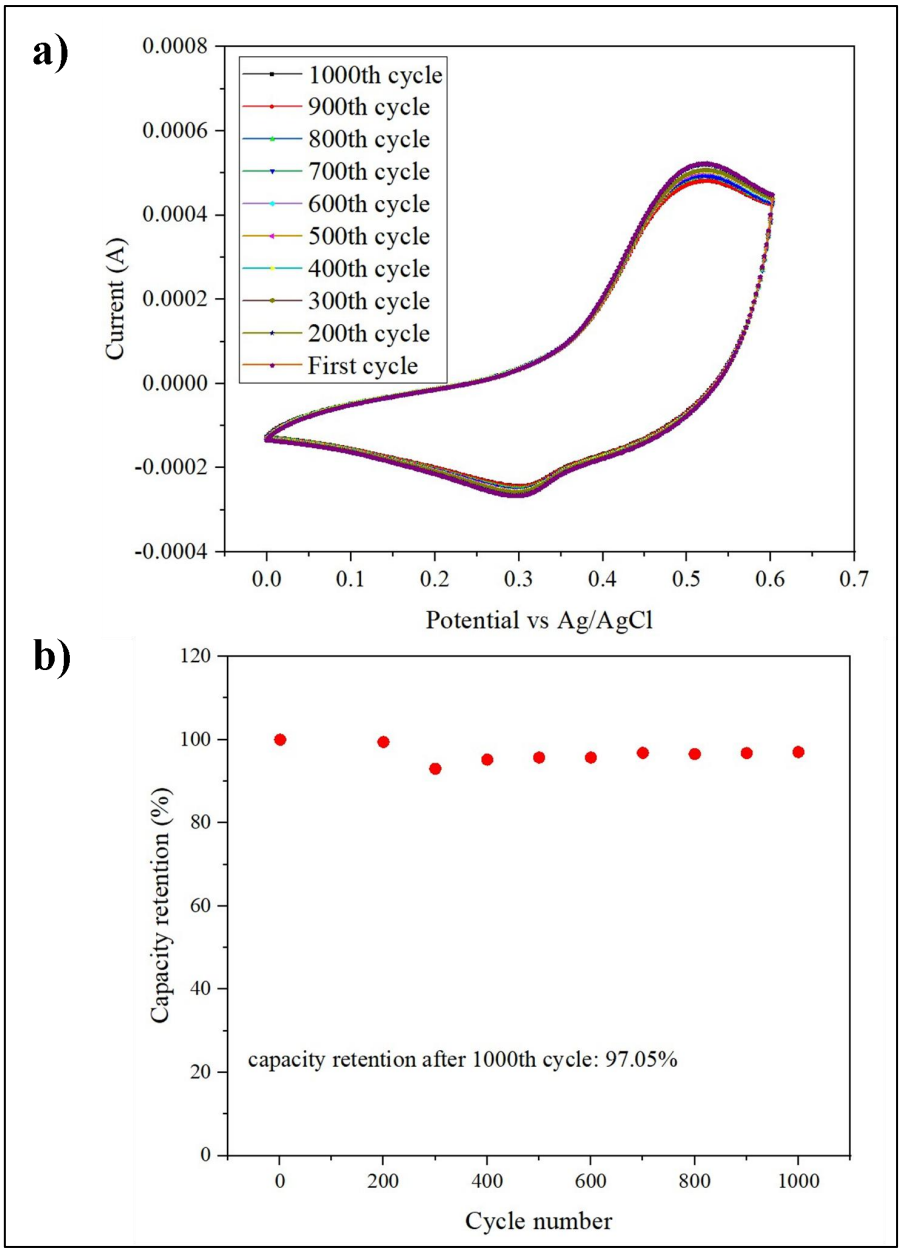

Figure 4.22 a) CV curves of ZNC-GNP 0.2 at various cycles and b) Capacity retention of ZNC-GNP 0.2 sample

4.4.4 Impedance Analysis of Zn-Ni-Co/GNP at Various GNP wt%

The internal and diffusion resistances of ZNC-GNP samples with three different GNP loading was examined via EIS across a range of 100 kHz to 0.1 Hz frequency. In a typical Nyquist plot, the higher frequency region often exhibits a semicircular pattern whilst the lower frequency regions display a straight-line spike. The intercept on the real axis (Z') corresponds to the solution resistance (R_s) that associated to the resistance of the electrolyte and intrinsic resistance of the electrode

material. The presence of semicircle is mainly associated to the charge transfer resistance (R_{ct}) (Ramli *et al*., 2018). The value of R_{ct} is represented by the diameter of the semicircle, which also related to the electrolyte resistance in the pores of the electrodes. Material with higher porosity has the tendency to improve the ion and electron transport, hence reducing the internal resistance (Mei *et al.*, 2018). The low frequency region typically shows a straight line at a 45° angle, or a vertical line which known as Warburg impedance (W), corresponds to the material's capacitive potential and their ability for ion transportation at the electrode/electrolyte interface (Suganya *et al*., 2022). In a scenario involving an ideal capacitor, the Nyquist plot is expected to show a perfectly vertical 90˚ straight line that signifies purely capacitive charge storage with negligible resistance. Hence, deviation from the vertical straight line suggests the existence of resistive behaviour which limits the efficiency of ion diffusion.

As can be seen on Figure 4.23, the x-axis intercepts for ZNC-GNP 0.2 shows the lowest R_s of 5.43 Ω, followed by ZNC-GNP 0.1 with 8.14 Ω resistance and the highest can be seen on ZNC-GNP 0.3 with 9.87 Ω R_s value. Lower R_s value is analogous to superior electrical conductivity and lower internal resistance. Among the samples, ZNC-GNP 0.2 exhibits the smallest overall impedance and steepest low-frequency slope, signifying improved ion transport and higher capacitive response. Conversely, ZNC-GNP 0.3 shows the highest impedance and R_s, which may result from excessive GNP content leading to agglomeration, blocking ion diffusion pathways and increasing overall resistance. ZNC-GNP 0.1, with a moderate R_s, lacks sufficient graphene to fully establish conductive networks, resulting in intermediate performance.

The capacitive trends observed in CV correlate well with the EIS findings in which the highest Cs value is obtained in ZNC-GNP 0.2 sample, followed by ZNC-GNP 0.1, and the lowest for ZNC-GNP 0.3. These results highlight the importance of optimizing the GNP content to balance electrical conductivity, porosity, and electrochemical activity. Overall, the deviation of your Nyquist plots from the typical semicircular profile reinforces the capacitive nature of the system and the dominance of ion diffusion and electrode porosity in determining performance.

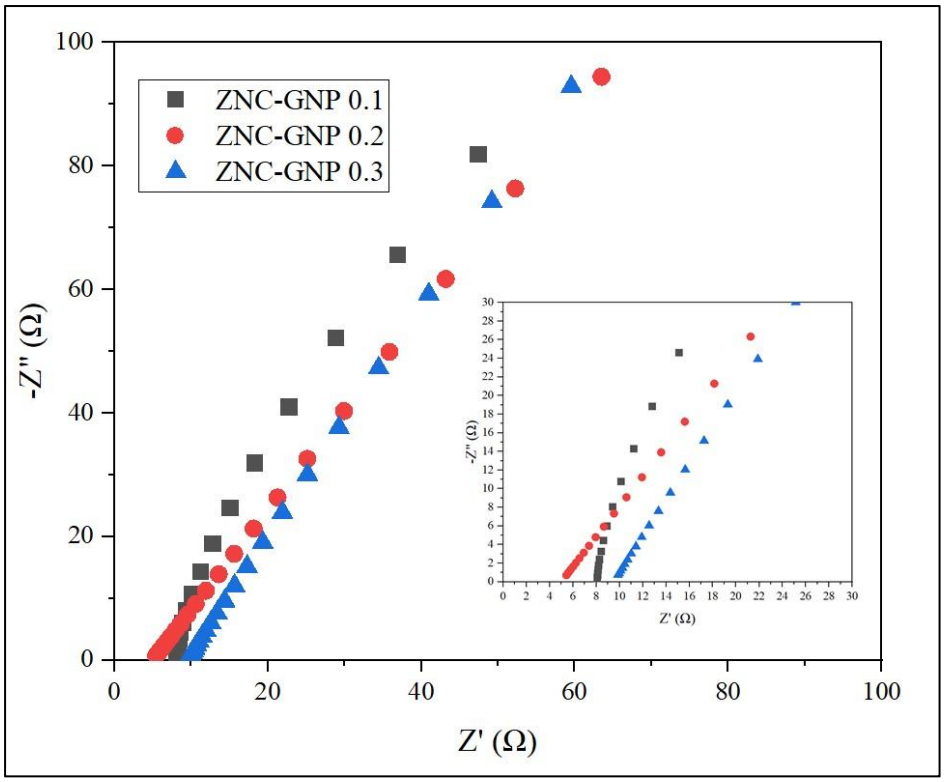

Figure 4.23 EIS spectra of ZNC-GNP 0.1, ZNC-GNP 0.2, and ZNC-GNP 0.3

4.4.5 Dunn Analysis of Zn-Ni-Co/GNP

To elucidate the charge storage mechanism of the synthesized Zn/Co/Ni-GNP electrode, Dunn's analysis was performed by plotting the peak current against the square root of the scan rate ($v^{1/2}$), as depicted in Figure 4.24. The linear relationship observed for both anodic and cathodic peak currents suggests that the redox processes are primarily diffusion-controlled. Specifically, the anodic peak current exhibited a linear fit with a coefficient of determination (R^2) of 0.96175, while the cathodic peak current demonstrated an even stronger linearity with an R^2 value of 0.99942. These findings imply that the redox activity during both oxidation and reduction predominantly involves ion diffusion into the bulk of the active material, a characteristic commonly associated with battery-type behaviour. The slightly lower R^2 value in the anodic region may indicate minor capacitive contributions or slight kinetic limitations, yet the overall trend confirms that diffusion-controlled processes dominate the electrochemical response of the Zn/Co/Ni-GNP electrode (Guo *et al.*, 2018).

To further quantify the capacitive and diffusion-controlled contributions, a

kinetic analysis was conducted across various scan rates ranging from 5 to 100 mV s^{-1}, and the results are summarized in Figure 4.25. At a low scan rate of 5 mV s^{-1}, the diffusion-controlled process accounted for 85% of the total current, while the capacitive contribution was only 15%. This high diffusion dominance at low scan rates is consistent with the intercalation and redox processes that require longer time scales for ion penetration into the bulk of the electrode material. As the scan rate increased, a gradual shift in the contribution dynamics was observed. At 20 mV s^{-1}, the capacitive portion rose to 26%, and it continued to increase with scan rate, reaching 44% at 100 mV s^{-1}. This trend reflects the increasing prominence of surface-controlled or pseudocapacitive processes at higher scan rates, where limited time for ion diffusion results in more superficial redox reactions at or near the electrode surface.

The observed transition from diffusion-dominated to mixed charge storage behaviour with increasing scan rates highlights the hybrid nature of the Zn/Co/Ni-GNP system. Such behaviour is highly desirable in advanced energy storage devices, as it enables the material to simultaneously offer high energy density at lower scan rates and enhanced power capability at higher scan rates. The gradual rise in capacitive contribution further suggests that the presence GNPs effectively enhances the electrode's electronic conductivity and surface area, thereby facilitating faster charge transfer processes. The incorporation of multiple transition metals (Zn, Co, and Ni) likely contributes to the synergistic redox activity and structural stability of the electrode, promoting both capacitive and diffusion-controlled storage.

When compared with existing studies on similar ternary metal-based or graphene-supported systems, the Zn/Co/Ni-GNP electrode shows comparable or improved electrochemical activity. Previous works have similarly reported dominant diffusion-controlled characteristics in bimetallic and trimetallic oxide systems, with increasing capacitive performance upon integration with conductive carbon substrates. The consistent linearity in the Dunn's plot and the balanced contribution profile over a wide scan rate range underscore the excellent reversibility and kinetics of the ZNC-GNP electrode, positioning it as a promising candidate for high-performance supercapacitors or hybrid energy storage devices.

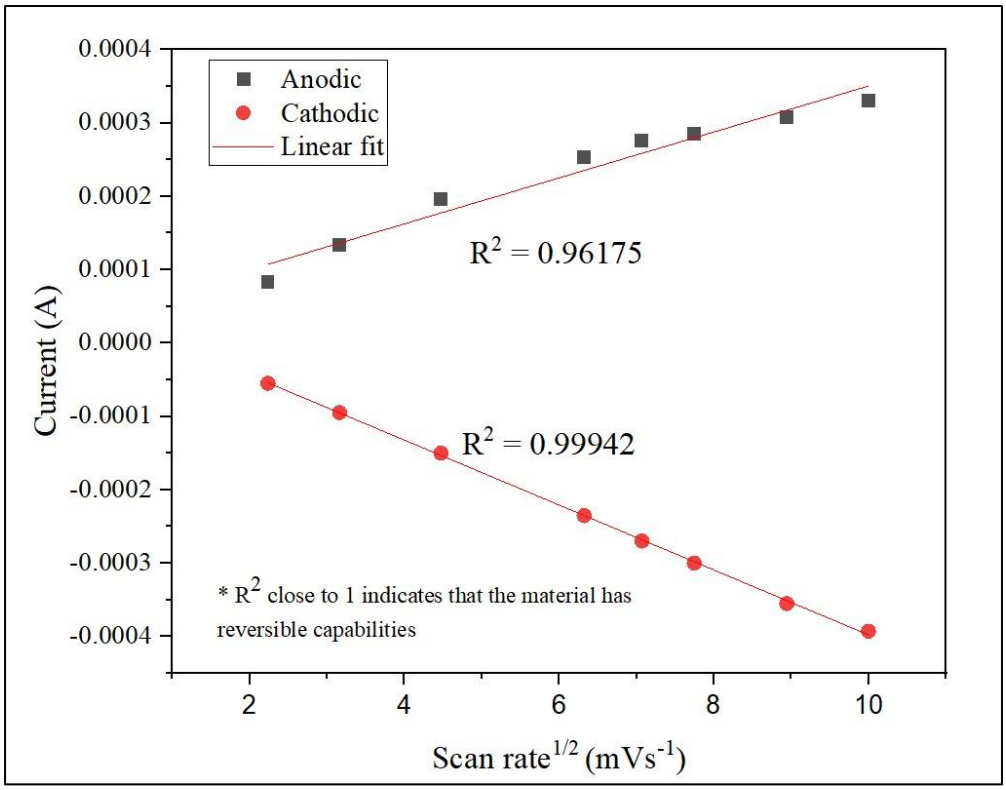

Figure 4.24 Peak current against the square root of the scan rate ($\nu^{1/2}$)

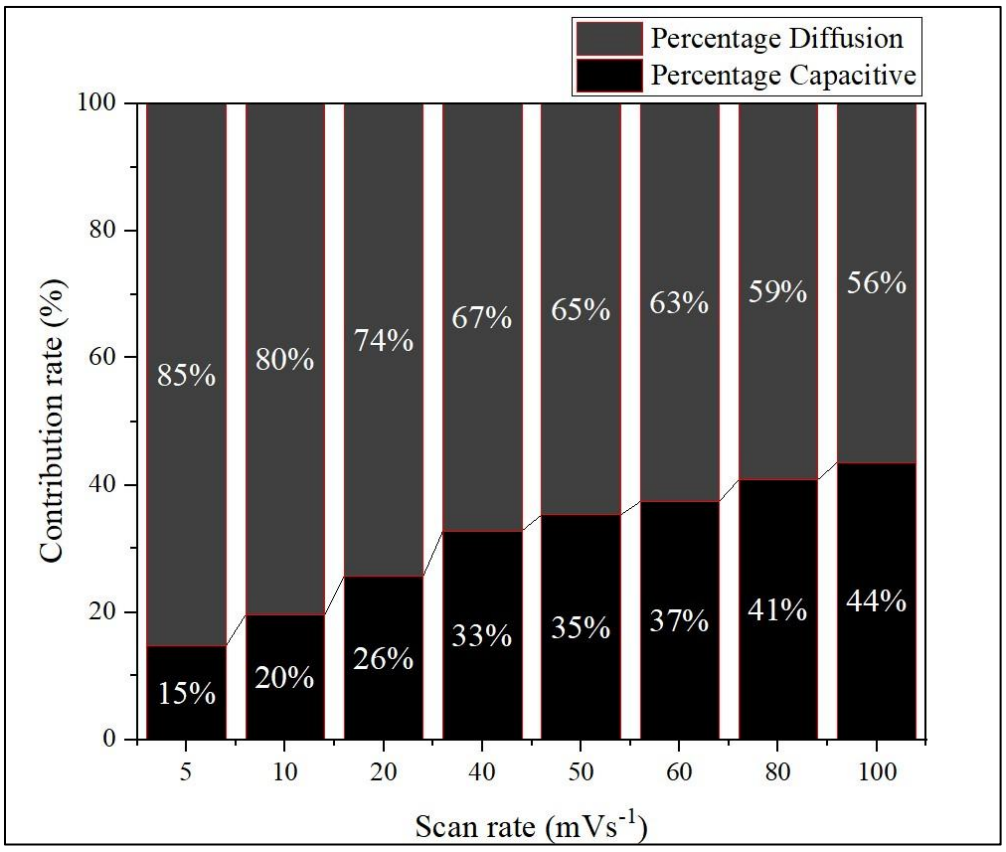

Figure 4.25 Capacitive and diffusive percentage bar graph by using Dunn's model

CHAPTER 5
CONCLUSION AND RECOMMENDATION

5.1 Conclusion

Throughout this work, synthesis and characterization of ZNC MTMOs, and their composites with GNP were successfully conducted. The physicochemical and electrochemical behaviours of the synthesized composites were analysed and discussed in relation to their potential for supercapacitor applications. This work has addressed the key gaps in understanding the effects of varying Zn: Ni: Co ratios to the morphological, structural, and electrochemical properties of the material. A comprehensive analysis of four different Zn-Ni-Co compositions namely 111, 121, 112, and 211 prepared via sol-gel method were done via XRD, FESEM, EDX, BET and FTIR spectroscopy. Morphologically, it was revealed that ZNC sample displayed a petal-like and globular structure with apparent clustering, while ZNC-GNP exhibited a crumpled and globular structure with enhanced distribution and less agglomeration, leading to a higher SSA, thus also enhanced the charge storage capability. The pore size distribution was calculated to be around 10-25 nm, ascribing to mesopores types of porosity. It was also determined that the average pore diameter of the ZNC-GNP samples was increased by 6-12% compared to the ZNC 112 sample, which possess the highest Cs value. This set of properties leads to a more efficient ionic and molecular species transport, hence boosting the supercapacitive performance of the material. Raman spectroscopy analysis confirmed the successful incorporation and structural integrity of GNP within the ZNC-GNP composites. All samples exhibited characteristic D, G, and 2D bands of graphitic carbon, with low ID/IG ratios indicating minimal defect formation and good preservation of sp^2 domains. Among the samples, ZNC-GNP 0.3 displayed the lowest ID/IG value, suggesting enhanced graphitic ordering with increased GNP content. The progressive intensification of the G and 2D bands further supported the presence of multilayered graphene structures, which contribute to improved electrical conductivity. Overall, the low defect density and well-retained graphitic structure highlight the beneficial processing conditions and the strong potential of these composites for high-performance supercapacitor

applications, owing to their synergistic combination of conductivity, structural stability, and electrochemical activity. The supercapacitive behaviour of the synthesized ZNC and ZNC-GNP samples were evaluated using a three-electrode system setup, with electrodes submerged into a 2M KOH electrolyte. All three electrochemical analysis inclusive of CV, GCD and EIS analysis are conducted in the same setup. The ZNC-GNP composite achieved a maximum Cs value of 478 Fg^{-1} at 5 mVs^{-1}, attributed to the synergistic effect of EDLC from GNP and pseudocapacitive behaviour from The ZNC counterpart. Through EIS analysis, it was evident that ZNC-GNP 0.2 demonstrated the most favourable impedance characteristics, including the lowest Rs and Rct values, along with a steep low-frequency slope which indicates enhanced ion transport and capacitive behaviour. In contrast, ZNC-GNP 0.3 exhibited the highest resistance values, likely due to agglomeration effects that hindered ion diffusion. Meanwhile, ZNC-GNP 0.1 showed moderate performance, reflecting insufficient graphene content for optimal conductivity. These findings underscore the importance of tuning GNP content to achieve a balanced synergy between electrical conductivity, porosity, and electrochemical activity. Overall, the EIS results reinforced the capacitive nature of the system and aligned well with the trends observed in cyclic voltammetry, further supporting the superior electrochemical performance of the ZNC-GNP 0.2 electrode. Based on the combined electrochemical evaluation, ZNC-GNP 0.2 is identified as the most suitable candidate for supercapacitor applications, exhibiting the highest Cs, improved energy density of 24.06 Wh kg^{-1}, excellent power density of 1375 W kg^{-1}, and good cycling stability. Additionally, Dunn's analysis confirmed revealed that the charge storage mechanism of the Zn-Co-Ni/GNP electrode is predominantly governed by diffusion-controlled processes, as indicated by the strong linear correlation between peak current and the square root of the scan rate. The kinetic analysis further confirmed a high diffusion contribution at low scan rates, with an increasing capacitive response observed as the scan rate increased. This transition from diffusion-dominated to mixed charge storage behaviour highlights the hybrid nature of the electrode, combining battery-type and pseudocapacitive characteristics. The enhanced capacitive contribution at higher scan rates also suggests improved surface conductivity and ion accessibility, attributed to the presence of GNPs and the synergistic effect of the Zn, Co, and Ni components.

These findings affirm the potential of the Zn-Co-Ni/GNP system for high-performance energy storage applications, offering a favourable balance between energy and power density.

5.2 Recommendations

In general, the Zn: Ni: Co ratios employed in this work are sufficient for screening the best-performing sample because the variation of each metal proportion is strategically done while maintaining a balanced ternary system. However, to further improve the findings of this study, it is equally important to venture into a broader range of ratios for deeper insights into the optimal composition for high performance material for energy storage device. Moreover, this can also be achieved by incorporating computational modelling techniques such as Density Functional Theory (DFT) to predict the electronic and structural properties of different Zn-Ni-Co compositions.

Furthermore, it is also worth to consider using other types of electrolytes apart from 2M KOH. The use of different types of electrolytes has different effects towards the electrochemical conditions. For instance, despite it's high-cost nature, ionic liquid-based or neutral electrolytes could improve the operational voltage windows and enhance the energy density of the tested material. Comparative study between alkaline and non-alkaline electrolytes can also be efficacious in providing deeper insights into the stability and redox activity of ZNC-based electrodes.

The electrochemical stability test is a vital evaluation method to unravel the supercapacitive behaviour of a material. It reflects the ability of a material to withstand repeated charging and discharging cycles. Moreover, stability tests assess the material's resistance towards degradation, inclusive of material's dissolution and electrolyte's decomposition. In this study, the stability was assessed over 1,000 charge-discharge cycles, providing preliminary insight into the cyclic behaviour and stability of the material. Hence, it is important to conduct the stability test over an extended number of charge-discharge cycles.

Incorporation of additional sample's characterization method such as X-ray Photoelectron Spectroscopy (XPS) is also crucial with the aim to get a clearer understanding of the physicochemical properties of the synthesized material,

especially in terms of surface chemistry and defects within the sample.

Overall, this work imparts an adequate amount scientific foundation to be used for further studies on Zn-Ni-Co- based supercapacitor materials contributing to Malaysia's progress in sustainable energy technologies. By optimizing composition, improving long-term stability, and exploring more scientific investigations, future studies can unlock the full potential of ternary metal oxide-based nanocomposites for next-generation energy storage applications.

REFERENCES

Abdul Karim, M. R., & Shehzad, W. (2023). Transition metal compounds and their hybrids with carbonaceous materials for electrochemical energy storage applications. Journal of Energy Storage, 72, 108288.

Abdul, A. H., Ramli, N., Nordin, A. N., & Abd. Wahab, M. F. (2021). Supercapacitor performance with activated carbon and graphene nanoplatelets composite electrodes, and insights from the equivalent circuit model. Carbon Trends, 5, 4917-4922.

Abo-Dief, H. M., El-Bahy, S. M., Hussein, O. K., El-Bahy, Z. M., Shahid, M., & Shakir, I. (2022). Synthesis and characterization of rGO supported silver doped bimetallic $ZnCo_2O_4$ spinel oxides for enhanced photocatalytic degradation of industrial effluents. Journal of Alloys and Compounds, 913, 165164.

Acharya, J., Pant, B., Ojha, G. P., Kong, H. S., & Park, M. (2021). Engineering triangular bimetallic metal-organic-frameworks derived hierarchical zinc-nickel-cobalt oxide nanosheet arrays@reduced graphene oxide-Ni foam as a binder-free electrode for ultra-high rate performance supercapacitors and methanol electro-oxidat. Journal of Colloid and Interface Science, 602, 573–589.

Aftab, J., Ali, A., Mehmood, S., Aftab, A., Ahmad, I., Bhopal, M. F., Hussain, M., Shah, Z. U., Shah, A. U., Padhiar, M. A., Wang, M., & Bhatti, A. S. (2023). Facile synthesis of synergetic MoO_2/MoS_2@GO nanohybrid as energy-efficient electrode material for high-performance asymmetric supercapacitor applications. Journal of Energy Storage, 74, 109324.

Ahmad, F., Shahzad, A., Danish, M., Fatima, M., Adnan, M., Atiq, S., Asim, M., Khan, M. A., Ain, Q. U., & Perveen, R. (2024). Recent developments in transition metal oxide-based electrode composites for supercapacitor applications. Journal of Energy Storage, 81, 110430.

Albetran, H. M. (2020). Structural Characterization of Graphite Nanoplatelets Synthesized from Graphite Flakes. Preprints, August, 1–8.

Ali, A., Hameed, I., Ammar, M., Mujahid, R., & Mirza, S. (2021). Enhanced rate capability for asymmetric supercapacitors by binder-free Zn-Ni-Co oxide nanoflakes on Ni foam. Journal of Energy Storage, 37, 102472-102482.

Andreas, H. A. (2015). Self-Discharge in Electrochemical Capacitors: A Perspective Article. Journal of The Electrochemical Society, 162(5), 5047–5053.

Anwer, A. H., Ansari, M. Z., Mashkoor, F., Zhu, S., Shoeb, M., & Jeong, C. (2023). Synergistic effect of carbon nanotube and tri-metallic MOF nanoarchitecture for electrochemical high-performance asymmetric supercapacitor applications and their charge storage mechanism. Journal of Alloys and Compounds, 955, 170038-170050.

Arunpandiyan, S., Bharathi, S., Pandikumar, A., Ezhil Arasi, S., & Arivarasan, A. (2020). Structural analysis and redox additive electrolyte based supercapacitor performance of ZnO/CeO_2 nanocomposite. Materials Science in Semiconductor Processing, 106, 104765-104773.

Asghar, A., Rashid, M. S., Javed, Y., Hussain, S., Shad, N. A., Hamza, M., & Chen, Z. (2023). Facile hydrothermal synthesis of MoS_2 nano-worms-based aggregate as electrode material for high energy density asymmetric supercapacitor. Electrochimica Acta, 465, 143011.

Babu, A., Somesh, T. E., Ani Dechamma, C. D., Hemavathi, A. B., Kakarla, R. R., Kulkarni, R. V., & Raghu, A. V. (2023). Ternary structured magnesium cobalt oxide/graphene/polycarbazole nanohybrids for high performance electrochemical supercapacitors. Materials Science for Energy Technologies, 6, 399–408.

Bai, X., Wang, Z., Luo, J., Wu, W., Liang, Y., Tong, X., & Zhao, Z. (2020). Hierarchical Porous Carbon with Interconnected Ordered Pores from Biowaste for High-Performance Supercapacitor Electrodes. Nanoscale Research Letters, 15(1).

Banavath, R., Nemala, S. S., Kim, S. H., Bohm, S., Ansari, M. Z., Mohapatra, D., & Bhargava, P. (2022). Industrially scalable exfoliated graphene nanoplatelets by high-pressure airless spray technique for high-performance supercapacitors. FlatChem, 33, 100373.

Belkessam, Célia, Mourad Mechouet, Naima Idiri, Abdel Aziz Kadri, and Necer Eddine Djelali. 2019. Synthesis and Characterization of $Ni_{0.3}Co_{2.7}O_4$ Oxide Nanoparticles Immobilized in Teflon Cavity Electrode for Organic Pollutants Degradation. Materials Research Express 6 (10), 1–14.

Bera, S., Miah, M., Mondal, T. K., Debnath, A., & Saha, S. K. (2022). Synthesis of new mixed metal oxide RuNi2O4 phase decorated on reduced graphene oxide for supercapacitor applications. Electrochimica Acta, 424, 140666.

Bernardi, Johannes. 2021. Energy-Dispersive X-Ray Spectroscopy. In Imaging Modalities for Biological and Preclinical Research: A Compendium, Volume 1: Part I: Ex Vivo Biological Imaging. IOP Publishing.

Bhargava, R., Khan, S., Ahmad, N., & Ansari, M. M. N. (2018). Investigation of structural, optical and electrical properties of Co_3O_4 nanoparticles. AIP Conference Proceedings, 1953, 1–5.

Bharti, Ahmed, G., Kumar, Y., & Sharma, S. (2021). DFT computation of quantum capacitance of pure and doped niobium nitrides for supercapacitor applications. Ceramics International, 47(13), 18948–18955.

Bianchini, M., Fauth, F., Hartmann, P., Brezesinski, T., & Janek, J. (2020). An in situ structural study on the synthesis and decomposition of $LiNiO_2$. Journal of Materials Chemistry A, 8, 1808–1820.

Bokov, D., Turki Jalil, A., Chupradit, S., Suksatan, W., Javed Ansari, M., Shewael, I. H., Valiev, G. H., & Kianfar, E. (2021). Nanomaterial by Sol-Gel Method: Synthesis and Application. Advances in Materials Science and Engineering, 2021.

Borges, R. S., Reddy, A. L. M., Rodrigues, M. T. F., Gullapalli, H., Balakrishnan, K., Silva, G. G., & Ajayan, P. M. (2013). Supercapacitor Operating at 200 Degrees Celsius. Scientific Reports, 3, 1–6.

Chang, T. C., Lu, Y. T., Lee, C. H., Gupta, J. K., Hardwick, L. J., Hu, C. C., & Chen, H. Y. T. (2021). The Effect of Degrees of Inversion on the Electronic Structure of Spinel $NiCo_2O_4$: A Density Functional Theory Study. ACS Omega, 6(14), 9692–9699.

Chen, H., Wang, J., Han, X., Liao, F., Zhang, Y., Gao, L., & Xu, C. (2019). Facile synthesis of mesoporous $ZnCo_2O_4$ hierarchical microspheres and their

excellent supercapacitor performance. CeramiCs International, 45(7), 8577–8584.

Chen, Jia, Wu, X., & Selloni, A. (2011). Electronic structure and bonding properties of cobalt oxide in the spinel structure. Physical Review B - Condensed Matter and Materials Physics, 83(24), 1–7.

Chen, Junchen, Song, X., Yang, F., Li, Y., Yang, S., Liao, L., Shen, Y., Guo, B., Ma, Z., Yu, B., Wang, M., Li, X., & Zhang, X. (2023). Electrochemically exfoliated graphene oxide enhanced hybrid fibers with high rate performance for fibrous supercapacitors. Surfaces and Interfaces, 43(November), 3604-3616.

Chen, X., Song, L., Zeng, M., Tong, L., Zhang, C., Xie, K., & Wang, Y. (2022). Regulation of morphology and electronic configuration of $NiCo_2O_4$ by aluminum doping for high performance supercapacitors. Journal of Colloid and Interface Science, 610, 70–79.

Cheng, J., Jiao, R., & Sun, Q. (2024). Free-standing N, S co-doped graphene aerogels coupled with Eucalyptus wood tar-based activated carbon and cellulose nanofibers for high-performance supercapacitor and removal of Cr(VI). International Journal of Biological Macromolecules, 254(P1), 127542.

Chinnalagu, D. kumar, Murugesan, B., Arumugam, M., Chinniah, K., Ganesan, S., Cai, Y., & Mahalingam, S. (2023). Fabrication of 2D-Borophene nanosheets anchored S, N-mesoporous carbon nanocomposite (SNC-Bp//SNC-Bp) symmetric device for high-performance supercapacitor application. Journal of Energy Storage, 74, 9328-9333.

Citra, A., Chertihin, G. V., Andrews, L., & Neurock, M. (1997). Reactions of laser-ablated nickel atoms with dioxygen. Infrared spectra and density functional calculations of nickel oxides NiO, ONiO, Ni_2O_2, and Ni_2O_3, superoxide NiOO, peroxide $Ni(O_2)$, and higher complexes in solid argon. Journal of Physical Chemistry A, 101(17), 3109–3118.

Cochran, E. A., Woods, K. N., Johnson, D. W., Page, C. J., & Boettcher, S. W. (2019). Unique chemistries of metal-nitrate precursors to form metal-oxide thin films from solution: Materials for electronic and energy applications. Journal of Materials Chemistry A, 7(42), 24124–24149.

Da Silva, E. P., Rubira, A. F., Ferreira, O. P., Silva, R., & Muniz, E. C. (2019). In situ growth of manganese oxide nanosheets over titanium dioxide nanofibers and their performance as active material for supercapacitor. Journal of Colloid and Interface Science, 555, 373–382.

Das, Amit Kumar, Sumanta Kumar Karan, and B. B. Khatua. 2015. High Energy Density Ternary Composite Electrode Material Based on Polyaniline (PANI), Molybdenum Trioxide (MoO_3) and Graphene Nanoplatelets (GNP) Prepared by Sono-Chemical Method and Their Synergistic Contributions in Superior Supercapacitive Performance. Electrochimica Acta 180, 1–15.

Davis, K., Yarbrough, R., Froeschle, M., White, J., & Rathnayake, H. (2019). Band gap engineered zinc oxide nanostructures: Via a sol-gel synthesis of solvent driven shape-controlled crystal growth. RSC Advances, 9(26), 14638–14648.

Dhas, S. D., Maldar, P. S., Patil, M. D., Hubali, K. M., Shembade, U. V., Abitkar, S. B., Waikar, M. R., Sonkawade, R. G., Agawane, G. L., & Moholkar, A. V. (2021). Hydrothermal synthesis of mesoporous $NiMnO_3$ nanostructures for supercapacitor application: Effect of electrolyte. Journal of Energy Storage, 35.

Ding, Z., Trouillet, V., & Dsoke, S. (2019). Are Functional Groups Beneficial or Harmful on the Electrochemical Performance of Activated Carbon Electrodes. Journal of The Electrochemical Society, 166(6), A1004–A1014.

Dos Santos Costa, M. J., dos Santos Costa, G., & da Silva Santos, R. (2023). Investigation of supercapacitor properties using iron tungsten porous electrode in neutral aqueous electrolyte. Nano-Structures and Nano-Objects, 36, 101060.

Dubey, P., Kaurav, N., Devan, R. S., Okram, G. S., & Kuo, Y. K. (2018). The effect of stoichiometry on the structural, thermal and electronic properties of thermally decomposed nickel oxide. RSC Advances, 8(11), 5882–5890.

Escobar, C. A., & Martín-Ruiz, A. (2020). On the four-body problem in the Born–Oppenheimer approximation. Annals of Physics, 422, 168311-168323.

Ezeigwe, E. R., Khiew, P. S., Siong, C. W., & Tan, M. T. T. (2020). Mesoporous Zinc–Nickel–Cobalt nanocomposites anchored on graphene as electrodes for electrochemical capacitors. Journal of Alloys and Compounds, 816, 1–8.

Faid, A. Y., & Ismail, H. (2019). Ternary mixed nickel cobalt iron oxide nanorods as a high-performance asymmetric supercapacitor electrode. Materials Today Energy, 13, 285–292.

Faras, M. M., Patil, S. S., Patil, P. S., & Torane, A. P. (2023). Unleashing the Potential of Binder-Free Hydrothermally Synthesized Marigold-Like $ZnCo_2O_4$ for Supercapacitors. Journal of Energy Storage, 74, 9490-9503.

Farkaš, B., Santos-Carballal, D., Cadi-Essadek, A., & de Leeuw, N. H. (2019). A DFT+U study of the oxidation of cobalt nanoparticles: Implications for biomedical applications. Materialia, 7(January), 381-395.

Fatima, S., Ali, S. I., Iqbal, M. Z., & Rizwan, S. (2017). The high photocatalytic activity and reduced band gap energy of la and Mn co-doped $BiFeO_3$/graphene nanoplatelet (GNP) nanohybrids. RSC Advances, 7(57), 35928–35937.

Fleischmann, S., Mitchell, J. B., Wang, R., Zhan, C., Jiang, D., Presser, V., & Augustyn, V. (2020). Pseudocapacitance : From Fundamental Understanding to High Power Energy Storage Materials. Chemical Reviews, 120(14, 6738-6782

Fong, K. D., Wang, T., & Smoukov, S. K. (2017). Multidimensional performance optimization of conducting polymer-based supercapacitor electrodes. Sustainable Energy & Fuels, 1(9), 1857–1874.

Fu, H., Zhang, A., Guo, H., Zong, H., Jin, F., Zhao, K., & Liu, J. (2022). Rose-like Zn-Ni-Co layered double hydroxide grown on Co_3O_4 nanowire arrays for high energy density flexible supercapacitors. Journal of Energy Storage, 56, 106056.

Gedi, S., Manne, R., Manjula, G., Reddy, L. V., Reddy, C. P., Marraiki, N., Kim, W. K., Mallikarjuna, K., & Pratap Reddy, M. S. (2022). Tunability of the self-assemblies of porous polygon-like zinc cobaltite architectures using mixed solvents for high-performance supercapacitors. Journal of Physics and Chemistry of Solids, 163, 587-593.

Gnanamoorthy, G., Ramar, K., Ali, D., Yadav, V. K., Sureshbabu, K., & Narayanan, V. (2020). A series of $ZnCo_2O_4$/rGO/Pt nanocubes with excellent photocatalytic activity towards visible light. Chemical PhysiCs Letters, 759, 137988-137995.

Goclon, J. (2020). Manipulation of structural and electronic properties of B-doped carbon nano–onions based on DFT modelling. Applied Surface Science, 532, 147267.

González-Banciella, Andrés, David Martinez-Diaz, Adrián de Hita, María Sánchez, and Alejandro Ureña. 2024. M-Doped (M = Zn, Mn, Ni) Co-MOF-Derived Transition Metal Oxide Nanosheets on Carbon Fibers for Energy Storage Applications. Nanomaterials 14 (22), 1–16.

Graydon, J. W., Panjehshahi, M., & Kirk, D. W. (2014). Charge redistribution and ionic mobility in the micropores of supercapacitors. Journal of Power Sources, 245, 822–829.

Grover, S., Sahu, V., Singh, G., & Sharma, R. K. (2020). High specific energy ternary nanocmposite polyaniline:Manganeese dioxide@ MWCNT electrode for asymmetric supercapacitor. Journal of Energy Storage, 29, 121-130.

Gu, H., Yu, L., Wang, J., Yao, J., & Chen, F. (2017). A sol-gel preparation of ZnO/graphene composite with enhanced electronic properties. Materials Letters, 196, 168–171.

Guo, F., Gupta, N., & Teng, X. (2018). Enhancing Pseudocapacitive Process for Energy Storage Devices: Analyzing the Charge Transport Using Electro-kinetic Study and Numerical Modeling. Supercapacitors - Theoretical and Practical Solutions.

Guo, Hongxu, Jianhua Chen, Wen Weng, Qingxiang Wang, and Shunxing Li. 2014. Facile Template-Free One-Pot Fabrication of $ZnCo_2O_4$ Microspheres with Enhanced Photocatalytic Activities under Visible-Light Illumination. Chemical Engineering Journal 239, 192–99.

Guo, X., Chen, C., Zhang, Y., Xu, Y., & Pang, H. (2019). The application of transition metal cobaltites in electrochemistry. Energy Storage Materials, 23, 439–465.

Hadizadeh, R., & Faraji, M. (2023). Introducing of leached supercapacitor coin-devices with excellent performance based on tungsten oxide-carbon nanotubes-graphite nanocomposite. International Journal of Hydrogen Energy, 48(97), 38223–38236.

Haldar, P. (2021). Achieving wide potential window and high capacitance for supercapacitors using different metal oxides (viz.: ZrO_2, WO_3 and V_2O_5) and

their PANI/graphene composites with Na_2SO_4 electrolyte. Electrochimica Acta, 381.

Han, X., Liao, F., Zhang, Y., Han, X., Xu, C., & Chen, H. (2019). Solvothermal preparation of zinc cobaltite mesoporous microspheres for high-performance electrochemical supercapacitors. Journal of Alloys and Compounds, 781, 425–432.

Han, Xingrong, Liao, F., Zhang, Y., Han, X., Xu, C., & Chen, H. (2019). Solvothermal preparation of zinc cobaltite mesoporous microspheres for high-performance electrochemical supercapacitors. Journal of Alloys and Compounds, 781, 425–432.

Han, Xuanxuan, Song, L., Ding, J., Hu, L., Xu, C., & Wang, Y. (2020). Design and preparation of Cu-doped $NiCo_2O4$ nanosheets with intrinsic porosities for symmetric supercapacitors. Materials Letters, 278, 128400-128411.

Harun, K., Azmira, N., Deghfel, B., Kamil, M., & Azmin, A. (2020). DFT + U calculations for electronic , structural , and optical properties of ZnO wurtzite structure : A review. Results in Physics, 16, 2829-2836.

Helseth, L. E. (2021). The self-discharging of supercapacitors interpreted in terms of a distribution of rate constants. Journal of Energy Storage, 34, 102199.

Hepel, M. (2022). Advances in micro-supercapacitors (MSCs) with high energy density and fast charge-discharge capabilities for flexible bioelectronic devices—A review. Electrochemical Science Advances, 1–33.

Hohenberg, P., & W. Kohn. (1964). Inhomogenous Electron Gas. Physical Review, 136(3B), B 864.

Hsu, C. T., & Hu, C. C. (2013). Synthesis and characterization of mesoporous spinel $NiCo_2O_4$ using surfactant-assembled dispersion for asymmetric supercapacitors. Journal of Power Sources, 242, 662–671.

Hu, R., & Shang, J. (2019). Quantum capacitance of transition metal and nitrogen co-doped graphenes as supercapacitors electrodes: A DFT study. Applied Surface Science, 496.

Hu, W., Wei, H., She, Y., Tang, X., Zhou, M., Zang, Z., Du, J., Gao, C., Guo, Y., & Bao, D. (2017). Flower-like nickel-zinc-cobalt mixed metal oxide nanowire

arrays for electrochemical capacitor applications. Journal of Alloys and Compounds, 708, 146–153.

Huang, B., Tang, Q., Liang, C., Liu, N., & Wang, Y. (2021). Facile synthesis of multilayer graphene nanoplatelets/$ZnCo_2O_4$ microspheres with enhanced performance for asymmetric supercapacitors. Materials Letters, 298, 130022.

Huang, J., Li, Y., Xie, R., Li, J., Tian, Z., Chai, G., Zhang, Y., Lai, F., He, G., Liu, C., Liu, T., & Brett, D. J. L. (2021). Structural engineering of cathodes for improved Zn-ion batteries. Journal of Energy Chemistry, 58, 147–155.

Huang, L., Huang, H., Guo, W., & Wang, S. (2022). 3D urchin-like of Zn-Ni-Co ternary oxide microspheres as high-performance electrodes for supercapacitors. Electrochimica Acta, 434(October), 141317.

Huang, T., Qiu, Z., Hu, Z., & Lu, X. (2021). Novel method of preparing hierarchical porous $CoFe_2O_4$ by the citric acid-assisted sol-gel auto-combustion for supercapacitors. Journal of Energy Storage, 35, 102286.

Ilyas, M. M., Manzoor, A., Khan, M. A., Shahzad, A., Afzal, A. M., Rasul, M. N., & Saleem, M. R. (2024). Synthesis, microstructure, and electromagnetic behavior of graphene nanoplatelets/CZCF ferrite nanocomposites. Synthetic Metals, 307,117664.

Imran, M., Afzal, A. M., Iqbal, M. W., Mumtaz, S., & Alqarni, A. S. (2024). Superior Electrochemical Performance and Cyclic Stability of WS_2@CoMgS//AC Composite on the Nickel-Foam for Asymmetric Supercapacitor Devices. Energies, 17(14).

Iqbal, J., Li, L., Numan, A., Rafique, S., Jafer, R., Mohamad, S., Khalid, M., Ramesh, K., & Ramesh, S. (2019). Density functional theory simulation of cobalt oxide aggregation and facile synthesis of a cobalt oxide, gold and multiwalled carbon nanotube based ternary composite for a high performance supercapattery. New Journal of Chemistry, 43(33), 13183–13195.

Iqbal, M. Z., Aziz, U., Amjad, N., Aftab, S., & Wabaidur, S. M. (2023). Porous activated carbon and highly redox active transition metal sulfide by employing multi-synthesis approaches for battery-supercapacitor applications. Diamond and Related Materials, 136, 110019.

Isacfranklin, M., Daphine, S., Yuvakkumar, R., Kungumadevi, L., Ravi, G., Al-Sehemi, A. G., & Velauthapillai, D. (2022). $ZnCo_2O_4$/CNT composite for efficient supercapacitor electrodes. Ceramics International, 48(17), 24745–24750.

Jabeen, S., Aadil, M., Williams, J., Awan, M. S., Iqbal, J., Zulfiqar, S., & Nazar, N. (2021). Synthesis of In_2O_3/GNPs nanocomposites with integrated approaches to tune overall performance of electrochemical devices. Ceramics International, 47(16), 22345–22355.

Jafari, M., Ganjali, F., Eivazzadeh-Keihan, R., Maleki, A., & Geranmayeh, S. (2024). Recent advances in applications of graphene-layered double hydroxide nanocomposites in supercapacitors and batteries. FlatChem, 45, 100658.

Jayasooriya, U. A., & Jenkins, R. D. (2002). Introduction to Raman Spectroscopy. An Introduction to Laser Spectroscopy, 77–104.

Jian, Y., Tian, M., He, C., Xiong, J., Jiang, Z., Jin, H., Zheng, L., Albilali, R., & Shi, J. W. (2021). Efficient propane low-temperature destruction by Co_3O_4 crystal facets engineering: Unveiling the decisive role of lattice and oxygen defects and surface acid-base pairs. Applied Catalysis B: Environmental, 283, 119657.

Jin, J., Wang, N., Wang, Y., Wang, Y., & Sun, T. (2023). Synergistic effect of bimetal (Zn/Ni)–organic framework/reduced graphene oxide for high-performance supercapacitor. Applied Surface Science, 615, 156435.

Jittiarporn, P., Badilescu, S., Al Sawafta, M. N., Sikong, L., & Truong, V. Van. (2017). Electrochromic properties of sol–gel prepared hybrid transition metal oxides – A short review. Journal of Science: Advanced Materials and Devices, 2(3), 286–300.

Julieta, L., Angela, C., Raba, M., & Rincón-joya, M. (2020). Synthesis and evaluation of nickel doped Co_3O_4 produced through hydrothermal technique. 87(213), 184–191.

Kaewmaraya, T., Luo, W., Yang, X., Panigrahi, P., & Ahuja, R. (2015). A new, layered monoclinic phase of Co_3O_4 at high pressure. Physical Chemistry Chemical PhysiCs, 17(30), 19957–19961.

Karuppaiah, M., Akilan, R., Sakthivel, P., Asaithambi, S., Shankar, R., Yuvakkumar, R., Hayakawa, Y., & Ravi, G. (2020). Synthesis of self-assembled micro/nano

structured manganese carbonate for high performance, long lifespan asymmetric supercapacitors and investigation of atomic-level intercalation properties of OH− ions via first principle calculation. Journal of Energy Storage, 27, 101138.

Kate, R. S., Khalate, S. A., & Deokate, R. J. (2018). Overview of nanostructured metal oxides and pure nickel oxide (NiO) electrodes for supercapacitors: A review. Journal of Alloys and Compounds, 734, 89–111.

Kathalingam, A., Ramesh, S., Yadav, H. M., Choi, J. H., Kim, H. S., & Kim, H. S. (2020). Nanosheet-like $ZnCo_2O_4$@nitrogen doped graphene oxide/polyaniline composite for supercapacitor application: Effect of polyaniline incorporation. Journal of Alloys and Compounds, 830, 154734.

Khalaj, M., Golkhatmi, S. Z., & Sedghi, A. (2021). High-performance supercapacitor electrode materials based on chemical co-precipitation synthesis of nickel oxide (NiO)/cobalt oxide (Co_3O_4)-intercalated graphene nanosheets binary nanocomposites. Diamond and Related Materials, 114, 108313.

Khalid, M., Riaz, S., & Naseem, S. (2014). First Principle calculation of Indium doped ZnO using LDA and GGA approximation. The 2014 World Congress on Advances in Civil, Environmental, and Materials Research, 24–28.

Khan, S. A., Khan, S. B., Khan, L. U., Farooq, A., Akhtar, K., & M.Asiri, A. (2018). Fourier Transform Infrared Spectroscopy: Fundamentals and Application in Functional Groups and Nanomaterials Characterizations. Handbook of Materials Characterization, 2020, 317–343.

Kharangarh, P. R., Ravindra, N. M., Rawal, R., Singh, A., & Gupta, V. (2021). Graphene quantum dots decorated on spinel nickel cobaltite nanocomposites for boosting supercapacitor electrode material performance. Journal of Alloys and Compounds, 876, 159990.

Kiaeerad, P., & Naji, L. (2021). Synergistic effect of two complexing agents on the hydrothermal synthesis of self-supported Zn-Ni-Co oxide as electrode material in supercapacitors. Journal of Electroanalytical Chemistry, 901, 115779.

Kim, H., Surendran, S., Chae, Y., Lee, H. Y., An, T. Y., Han, H. S., Park, W., Kim, J. K., & Sim, U. (2020). Fabrication of an ingenious metallic asymmetric

supercapacitor by the integration of anodic iron oxide and cathodic nickel phosphide. Applied Surface Science, 511, 145424.

Kim, T. H., Veerasubramani, G. K., & Kim, S. J. (2018). Hierarchical porous flower-like nickel cobaltite nanosheets as a binder-less electrode for supercapacitor application with ultra-high capacitance. Journal of Industrial and Engineering Chemistry, 61, 181–187.

Krüger, E. (2020). Structural distortion stabilizing the antiferromagnetic and insulating ground state of NiO. Symmetry, 12(1), 1–20.

Kumar, S., Saeed, G., Hoon, N., & Hee, J. (2019). Fabrication of Co-Ni-Zn ternary Oxide @$NiWO_4$ core-shell nanowire arrays and Fe_2O_3-CNTs @GF for ultra-high performance asymmetric supercapacitor. Composites Part B, 176, 107223.

Kumar, V., Gajraj, V., Gnanasekar, K. I., Dsoke, S., Indris, S., Ehrenberg, H., Roling, B., & Mariappan, C. R. (2021). Hybrid aqueous supercapacitors based on mesoporous spinel-analogous Zn-Ni-Co-O nanorods: Effect of Ni content on the structure and energy storage. Journal of Alloys and Compounds, 882, 160712.

Lacivita, V., Erba, A., Noël, Y., Orlando, R., D'Arco, P., & Dovesi, R. (2013). Zinc oxide nanotubes: An ab initio investigation of their structural, vibrational, elastic, and dielectric properties. Journal of Chemical Physics, 138(21).

Lakehal, A., Bedhiaf, B., Bouaza, A., Benhebal, H., Ammari, A., & Dalache, C. (2018). Structural, optical and electrical properties of Ni-doped Co_3O_4 prepared via Sol-Gel technique. Materials Research, 21(3).

Lal, M. S., Lavanya, T., & Ramaprabhu, S. (2019). An efficient electrode material for high performance solid-state hybrid supercapacitors based on a Cu / CuO / porous carbon nanofiber / TiO_2 hybrid composite. 781–793.

Ledwaba, R. S., Womack, J. C., Skylaris, C. K., & Ngoepe, P. E. (2021). Intercalation voltages for spinel $LixMn_2O_4$ ($0 \leq x \leq 2$) cathode materials: Calibration of calculations with the ONETEP linear-scaling DFT code. Materials Today Communications, 27, 102380.

Li, H., Shi, F., An, Q., Zhai, S., Wang, K., & Tong, Y. (2021). Three-dimensional hierarchical porous carbon derived from lignin for supercapacitors: Insight into

the hydrothermal carbonization and activation. International Journal of Biological Macromolecules, 166, 923–933.

Li, S., Tian, Q., Chen, J., Chen, Y., Guo, P., Wei, C., Cui, P., Jiang, J., Li, X., & Xu, Q. (2023). An intrinsically non-flammable organic electrolyte for wide temperature range supercapacitors. Chemical Engineering Journal, 457, 141265.

Li, X., Tang, Y., Song, J., Yang, W., Wang, M., Zhu, C., Zhao, W., Zheng, J., & Lin, Y. (2018). Self-supporting activated carbon/carbon nanotube/reduced graphene oxide flexible electrode for high performance supercapacitor. Carbon, 129, 236–244.

Li, Y., Yang, Y., Shang, X., Song, C., Chen, J., Li, Y., Huang, M., & Meng, F. (2020). Design of a novel 3D hierarchical network porous CNS@$Ag_{0.5}$@Co_{180-10}/GNPs hetero-nanostructure hybrid as an excellent electrode for supercapacitor. Electrochimica Acta, 363, 137244.

Li, Z., Yu, J., Hu, M., Cai, X., Chen, Y., Cai, Y., & Wei, W. (2021). Construction of Zn–Co–Ni–Se nanosheet arrays on nickel foam for hybrid supercapacitors. CeramiCs International, 47(21), 29730–29738.

Li, Zheling, Deng, L., Kinloch, I. A., & Young, R. J. (2023). Raman spectroscopy of carbon materials and their composites: Graphene, nanotubes and fibres. Progress in Materials Science, 13, 101089.

Li, Zhongchun, Yu, J., Hu, M., Cai, X., Chen, Y., Cai, Y., & Wei, W. (2021). Construction of Zn–Co–Ni–Se nanosheet arrays on nickel foam for hybrid supercapacitors. Ceramics International, 47(21), 29730–29738.

Liang, Y., Luo, X., Zhang, Y., Yang, L., Hu, Z., & Zhu, M. (2023). Nickel cobaltite nanowire arrays grown on nitrogen-doped carbon nanotube fiber fabric for high-performance flexible supercapacitors. Journal of Colloid and Interface Science, 645, 391–399.

Liu, B., Wang, X., Chen, Y., Xie, H., Zhao, X., Nassr, A. B., & Li, Y. (2023). Honeycomb carbon obtained from coal liquefaction residual asphaltene for high-performance supercapacitors in ionic and organic liquid-based electrolytes. Journal of Energy Storage, 68, 107826.

Liu, C., Chen, B. H., Liu, W. R., & Duh, J. G. (2019). Synthesis and theoretical calculations of N-doped $ZnCo_2O_4$ anode for lithium-ion anode via gradient pressure-induced processes and theoretical calculations. Journal of Alloys and Compounds, 797, 978–985.

Liu, H., Wang, M., Zhai, D. D., Chen, X. Y., & Zhang, Z. J. (2019). Design and theoretical study of carbon-based supercapacitors especially exhibiting superior rate capability by the synergistic effect of nitrogen and phosphor dopants. Carbon, 155, 223–232.

Liu, K., Yu, C., Guo, W., Ni, L., Yu, J., Xie, Y., Wang, Z., Ren, Y., & Qiu, J. (2021). Recent research advances of self-discharge in supercapacitors: Mechanisms and suppressing strategies. Journal of Energy Chemistry, 58, 94–109.

Liu, Q., Liu, J., Xu, D., Liu, C., Lu, Z., Xuan, D., Wang, Z., Ye, Y., Wang, D., Li, S., Wang, D., & Zheng, Z. (2022). $NiCo_2O_4$ with unique 3D miniature sea urchins as binder-free electrode for high performance asymmetric supercapacitor. Journal of Electroanalytical Chemistry, 908, 116068.

Liu, R., Zhou, A., Zhang, X., Mu, J., & Che, H. (2021). Fundamentals, Advances and Challenges of Transition Metal Compounds-based Supercapacitors. Chemical Engineering Journal, 412, 128611.

Lobo, L. S., & Ruban Kumar, A. (2019). Structural and electrical properties of $ZnCo_2O_4$ spinel synthesized by sol-gel combustion method. Journal of Non-Crystalline Solids, 505, 301–309.

Low, W. H., Khiew, P. S., Lim, S. S., Siong, C. W., & Ezeigwe, E. R. (2019). Recent development of mixed transition metal oxide and graphene/mixed transition metal oxide based hybrid nanostructures for advanced supercapacitors. Journal of Alloys and Compounds, 775, 1324–1356.

Majeed, M., Akhtar, M., Khatoon, R., Amin, N., Morley, N., Tung, L. D., Amami, M., Abbas, W., Siddeeg, S. M., Thi Kim Thanh, N., Sajjad, M. T., & Arshad, M. I. (2024). Dielectric and magnetic response of Cu-Co-Sm ferrite impregnated with graphene nanoplatelets for high-frequency device applications. Journal of Alloys and Compounds, 986, 173770.

Makuła, P., Pacia, M., & Macyk, W. (2018). How To Correctly Determine the Band Gap Energy of Modified Semiconductor Photocatalysts Based on UV-Vis Spectra. Journal of Physical Chemistry Letters, 9(23), 6814–6817.

Malik, S., Gul, I. H., & Baig, M. M. (2021). Hierarchical MnNiCo ternary metal oxide/graphene nanoplatelets composites as high rated electrode material for supercapacitors. Ceramics International, 47(12), 17008–17014.

Mandal, B., Roy, R., & Mitra, P. (2021). Fabrication of different rare earth incorporated $ZnCo_2O_4$ matrix via chemical-mechanical hybrid mechanism and study their charge carrier dynamiCs by Motts VRH model. Journal of Alloys and Compounds, 879, 160432.

Mandal, Soumen, Arpit B. Mendhe, Hitesh M. Rakhade, Neha S. Barse, Mayna Roy, P. Rosaiah, Taejoon Park, Han Seung Lee, Avinash C. Mendhe, and Daewon Kim. 2025. Recent Advancement and Design in Supercapacitor Hybrid Electrode Materials: Bridging the Gap between Energy and Power Density. Chemical Engineering Journal Advances, 21, 100690.

Marwat, Mohsin Ali, Shaheer Ishfaq, Kanwar Muhammad Adam, Bilal Tahir, Muhammad Hamza Shaikh, Muhammad Fawad Khan, Muhammad Ramzan Abdul Karim, Zia Ud Din, Syed Abdullah, and Esha Ghazanfar. 2024. Enhancing Supercapacitor Performance of Ni-Co-Mn Metal-Organic Frameworks by Compositing It with Polyaniline and Reduced Graphene Oxide. RSC Advances 14 (3), 2102–15.

Mashrah, M., & Polat, S. (2023). Hydrothermal synthesis and electrochemical performance of GNPs-doped $MgFe_2O_4$ electrodes for supercapacitors. Solid State Ionics, 391, 116107.

Meena, D., Kumar, R., Gupta, S., Khan, O., Gupta, D., & Singh, M. (2023). Energy storage in the 21st century: A comprehensive review on factors enhancing the next generation supercapacitor mechanism. Journal of Energy Storage, 72 (C), 109323.

Mei, B. A., Munteshari, O., Lau, J., Dunn, B., & Pilon, L. (2018). Physical Interpretations of Nyquist Plots for EDLC Electrodes and Devices. Journal of Physical Chemistry C, 122(1), 194–206.

Mevada, C., & Mukhopadhyay, M. (2020). High mass loading tin oxide-ruthenium oxide-based nanocomposite electrode for supercapacitor application. Journal of Energy Storage, 31, 101587.

Mohamad, A. A., Hassan, M. S., Yaakob, M. K., Taib, M. F. M., Badrudin, F. W., Hassan, O. H., & Yahya, M. Z. A. (2017). First-principles calculation on electronic properties of zinc oxide by zinc–air system. Journal of King Saud University - Engineering Sciences, 29(3), 278–283.

Mohamed, S. G., Attia, S. Y., & Allam, N. K. (2017a). One-step, calcination-free synthesis of zinc cobaltite nanospheres for high-performance supercapacitors. Materials Today Energy, 4, 97–108.

Mohd Abdah, M. A. A., Azman, N. H. N., Kulandaivalu, S., & Sulaiman, Y. (2020). Review of the use of transition-metal-oxide and conducting polymer-based fibres for high-performance supercapacitors. Materials and Design, 186, 108199.

Moreno-Fernández, G., Boulanger, N., Nordenström, A., Iakunkov, A., Talyzin, A., Carriazo, D., & Mysyk, R. (2021). Ball-milling-enhanced capacitive charge storage of activated graphene in aqueous, organic and ionic liquid electrolytes. Electrochimica Acta, 370, 137738.

Murali, S., Dammala, P. K., Rani, B., Santhosh, R., Jadhao, C., & Sahu, N. K. (2020). Polyol mediated synthesis of anisotropic ZnO nanomaterials and composite with rGO: Application towards hybrid supercapacitor. Journal of Alloys and Compounds, 844, 156149.

Muzaffar, A., Ahamed, M. B., Deshmukh, K., & Thirumalai, J. (2019). A review on recent advances in hybrid supercapacitors: Design, fabrication and applications. Renewable and Sustainable Energy Reviews, 101, 123–145.

Naeem, F., Naeem, S., Zhao, Z., Shu, G. qiang, Zhang, J., Mei, Y., & Huang, G. S. (2020). Atomic layer deposition synthesized ZnO nanomembranes: A facile route towards stable supercapacitor electrode for high capacitance. Journal of Power Sources, 451, 227740.

Najib, S., & Erdem, E. (2019). Current progress achieved in novel materials for supercapacitor electrodes: Mini review. Nanoscale Advances, 1(8), 2817–2827.

Nare, R. K., Ramesh, S., Kakani, V., Haldorai, Y., Karthikeyan, C., Kumar, B. P., Siva Kumar, N., Asif, M., Kumar, S. N., Babu, D. P., Reddy, K. R., & Pasupuleti, V. R. (2024). CNTs supported $NiCo_2O_4$ nanostructures as advanced composite for high performance supercapacitors. Diamond and Related Materials, 141, 110660.

Naresh, B., Kuchi, C., Kummara, S. K., Ankinapalli, O. R., & Reddy, P. S. (2023). Solvothermal synthesis of $ZnCo_2O_4$ @rGO nanostructures for high-performance supercapacitor applications. Synthetic Metals, 293, 117283.

Naseri, F., Karimi, S., Farjah, E., & Schaltz, E. (2022). Supercapacitor management system: A comprehensive review of modeling, estimation, balancing, and protection techniques. Renewable and Sustainable Energy Reviews, 155, 111913.

Naveen, A. N., & Selladurai, S. (2015). Tailoring structural, optical and magnetic properties of spinel type cobalt oxide (Co_3O_4) by manganese doping. Physica B: Condensed Matter, 457, 251–262.

Nayak, P., Sahoo, M., & Nayak, S. K. (2020). Urchin-like $NiCo_2O_4$ microsphere by hydrothermal route: Structural, electrochemical, optical and magnetic properties. Ceramics International, 46(3), 3818–3826.

Nkeng, P., Poillerat, G., Koenig, J. F., Chartier, P., Lefez, B., Lopitaux, J., & Lenglet, M. (1995). Characterization of Spinel-Type Cobalt and Nickel Oxide Thin Films by X-Ray Near Grazing Diffraction, Transmission and Reflectance Spectroscopies, and Cyclic Voltammetry. Journal of The Electrochemical Society, 142(6), 1777–1783.

Obodo, R. M., Shinde, N. M., Chime, U. K., Ezugwu, S., Nwanya, A. C., Ahmad, I., Maaza, M., Ejikeme, P. M., & Ezema, F. I. (2020). Recent advances in metal oxide/hydroxide on three-dimensional nickel foam substrate for high performance pseudocapacitive electrodes. Current Opinion in Electrochemistry, 21, 242–249.

Okeil, S., Ungerer, J., Nirschl, H., & Garnweitner, G. (2024). Synthesis of Anisotropic Metal Oxide Nanoparticles via Non-Aqueous and Non-Hydrolytic Routes. KONA Powder and Particle Journal, 41(41), 197–220.

Olabi, A. G., Abbas, Q., Al Makky, A., & Abdelkareem, M. A. (2022). Supercapacitors as next generation energy storage devices: Properties and applications. Energy, 248, 123617.

Parsapour, F., Pooriraj, M., Moradi, M., Safarifard, V., & Hajati, S. (2023). Synthesis of M/Al (M = Co, Ni, Zn) layered double hydroxide derived from aluminum fumarate-based MOF as advanced materials for supercapacitor. Synthetic Metals, 292, 117234.

Parsapour, Fateme, Mehdi Pooriraj, Morteza Moradi, Vahid Safarifard, and Shaaker Hajati. 2023. Synthesis of M/Al (M = Co, Ni, Zn) Layered Double Hydroxide Derived from Aluminum Fumarate-Based MOF as Advanced Materials for Supercapacitor. Synthetic Metals 292, 117234.

Patel, K. K., Singhal, T., Pandey, V., Sumangala, T. P., & Sreekanth, M. S. (2021). Evolution and recent developments of high performance electrode material for supercapacitors: A review. Journal of Energy Storage, 44, 103366.

Petkov, V. (2008). Nanostructure by high-energy X-ray diffraction. Materials Today, 11(11), 28–38.

Polat, S. & Faris, D. (2022). Fabrication of $CuFe_2O_4$@g-C_3N_4@GNPs nanocomposites as anode material for supercapacitor applications. Ceramics International, 48(17), 24609–24618.

Poonam, Sharma, K., Arora, A., & Tripathi, S. K. (2019). Review of supercapacitors: Materials and devices. Journal of Energy Storage, 21, 801–825.

Prabhu, S., Gowdhaman, A., Harish, S., Navaneetham, M., & Ramesh, R. (2021). Synthesis of petal-like $CoMoO_4$/r-GO composites for high performances hybrid supercapacitor. Materials Letters, 295, 129821.

Pramitha, A., & Raviprakash, Y. (2022). Recent developments and viable approaches for high-performance supercapacitors using transition metal-based electrode materials. Journal of Energy Storage, 49, 104120.

Priya, M., Premkumar, V. K., Vasantharani, P., & Sivakumar, G. (2019). Structural and electrochemical properties of $ZnCo_2O_4$ nanoparticles synthesized by hydrothermal method. Vacuum, 167, 307–312.

Pu, X., Ren, X., Yin, H., Tang, Y., & Yuan, H. (2021). One-step electrodeposition strategy for growing nickel cobalt hydroxysulfide nanosheets for supercapacitor application. Journal of Alloys and Compounds, 865, 158736.

Raavi, R., Archana, S., Adinarayana Reddy, P., & Elumalai, P. (2023). Performances of dual carbon multi-ion supercapacitors in aqueous and non-aqueous electrolytes. Energy Advances, 2(3), 385–397.

Raja, K., Ramesh, P. S., & Geetha, D. (2014). Synthesis, structural and optical properties of ZnO and Ni-doped ZnO hexagonal nanorods by Co-precipitation method. Spectrochimica Acta - Part A: Molecular and Biomolecular Spectroscopy, 120, 19–24.

Ramachandran, T., Sana, S. S., Kumar, K. D., Kumar, Y. A., Hegazy, H. H., & Kim, S. C. (2023). Asymmetric supercapacitors: Unlocking the energy storage revolution. Journal of Energy Storage, 73, 109096.

Ramanathan, S., Sasikumar, M., Makarios, S. P., Obadiah, A., Angamuthu, A., Santhoshkumar, P., Durairaj, A., & Vasanthkumar, S. (2021). Low cost electrochemical composite material of paper cup waste carbon (P-carbon) and Fluorescein for supercapacitor application. Materials Today: Proceedings, 47(3), 825-536.

Ramli, N. I. T., Rashid, S. A., Mamat, M. S., Sulaiman, Y., & Krishnan, S. (2018). Incorporation of iron oxide into CNT/GNF as a high-performance supercapacitor electrode. Materials Chemistry and Physics, 212, 318–324.

Ramli, Nurul Infaza Talalah, Ab Malik Marwan Ali, Nur Hafiz Hussin, Mohamad Fariz Mohamad Taib, and Oskar Hasdinor Hassan. 2024. Unveiling Zn/Ni/Co Ternary Mixed Transition Metal Oxides Composite Anchored on Graphene Oxide As a Potential Material for Supercapacitor Electrode. Malaysian Journal of Analytical Sciences 28 (4), 886–98.

Rosaiah, P., Prakash, N. G., Divya, P., Sambasivam, S., Shkir, M., Algarni, H., & Ko, T. J. (2022). One-pot synthesis of flower-like Ni-Co/reduced graphene oxide layered double hydroxide nanocomposites as advanced electrodes for high-performance asymmetric supercapacitors. Journal of Energy Storage, 56, 106133.

Saha, S., Jana, M., Khanra, P., Samanta, P., Koo, H., Chandra Murmu, N., & Kuila, T. (2016). Band gap modified boron doped NiO/Fe_3O_4 nanostructure as the positive electrode for high energy asymmetric supercapacitors. RSC Advances, 6(2), 1380–1387.

Sahoo, B. B., Pandey, V. S., Dogonchi, A. S., Mohapatra, P. K., Thatoi, D. N., Nayak, N., & Nayak, M. K. (2023). A state-of-art review on 2D material-boosted metal oxide nanoparticle electrodes: Supercapacitor applications. Journal of Energy Storage, 65, 107335.

Saikia, B. K., Benoy, S. M., Bora, M., Tamuly, J., Pandey, M., & Bhattacharya, D. (2020). A brief review on supercapacitor energy storage devices and utilization of natural carbon resources as their electrode materials. Fuel, 282, 118796.

Saleem, S., Jameel, M. H., Akhtar, N., Nazir, N., Ali, A., Zaman, A., Rehman, A., Butt, S., Sultana, F., Mushtaq, M., Zeng, J. H., Amami, M., & Althubeiti, K. (2022). Modification in structural, optical, morphological, and electrical properties of zinc oxide (ZnO) nanoparticles (NPs) by metal (Ni, Co) dopants for electronic device applications. Arabian Journal of Chemistry, 15(1), 103518.

Scimeca, Manuel, Simone Bischetti, Harpreet Kaur Lamsira, Rita Bonfiglio, and Elena Bonanno. 2018. Energy Dispersive X-Ray (EDX) Microanalysis: A Powerful Tool in Biomedical Research and Diagnosis. European Journal of Histochemistry 62 (1), 89–99.

Seetharaman, A., Kandasamy, M., Manivannan, S., Jothivenkatachalam, K., Subramani, K., Pandikumar, A., Sathish, M., Rao Soma, V., Sivasubramanian, D., & Chakraborty, B. (2021). TiO_2/Carbon allotrope nanohybrids for supercapacitor application with theoretical insights from density functional theory. Applied Surface Science, 563, 150259.

Seetharaman, Amreetha, Manikandan Kandasamy, S. Manivannan, Kandasamy Jothivenkatachalam, Kaipannan Subramani, Alagarsamy Pandikumar, Marappan Sathish, Venugopal Rao Soma, Dhanuskodi Sivasubramanian, and Brahmananda Chakraborty. (2021). TiO_2/Carbon Allotrope Nanohybrids for Supercapacitor Application with Theoretical Insights from Density Functional Theory. Applied Surface Science 563: 150259.

Shamloofard, M., Shahrokhian, S., & Amini, M. K. (2021). Mesoporous nanostructures of NiCo-LDH/$ZnCo_2O_4$ as an efficient electrocatalyst for oxygen evolution reaction. Journal of Colloid and Interface Science, 604, 832–843.

Shehzad, W., & Abdul Karim, M. R. (2023). Improved energy storage performance of sonochemically synthesized Ni-Co-Zn ternary metal phosphate composites by incorporating PANI functionalized CNTs. Diamond and Related Materials, 137, 110050.

Shi, C., Cao, H., Li, S., Guo, L., Wang, Y., & Yang, J. (2022). Flexible nickel cobalt metal-organic frameworks/reduced graphene oxide hybrid film for high-performance supercapacitors. Journal of Energy Storage, 54, 105270.

Shi, F., Chen, C., Liu, J., Yu, T., & Wang, X. (2024). Construction of activated-CNT/carbon composite aerogel for supercapacitor electrode with ultra high cycle stability. Journal of Solid State Chemistry, 330, 124492.

Shin, S., & Shin, M. W. (2021). Nickel metal–organic framework (Ni-MOF) derived NiO/C@CNF composite for the application of high performance self-standing supercapacitor electrode. Applied Surface Science, 540.

Shu, R., Zhang, J., Guo, C., Wu, Y., Wan, Z., Shi, J., Liu, Y., & Zheng, M. (2020). Facile synthesis of nitrogen-doped reduced graphene oxide/nickel-zinc ferrite composites as high-performance microwave absorbers in the X-band. Chemical Engineering Journal, 384, 123266.

Shubha, A., & Manohara, S. R. (2020). Effect of graphene nanoplatelets concentration on optical, dielectric and electrical properties of poly(2-ethyl-2-oxazoline)–polyvinylpyrrolidone–graphene nanocomposites. Journal of Materials Science: Materials in Electronics, 31(19), 16498–16510.

Silambarasan, M., Ramesh, P. S., Geetha, D., Ravikumar, K., Ali, H. E., Algarni, H., Soundhirarajan, P., Chandekar, K. V., & Shkir, M. (2021). A Facile Preparation of Zinc Cobaltite ($ZnCo_2O_4$) Nanostructures for Promising Supercapacitor Applications. Journal of Inorganic and Organometallic Polymers and Materials, 31(10), 3905–3920.

Singh, V., Kosa, M., Majhi, K., & Major, D. T. (2015). Putting DFT to the test: A first-principles study of electronic, magnetic, and optical properties of Co_3O_4. Journal of Chemical Theory and Computation, 11(1), 64–72.

Soundarya, D., Sandhiya, M., Sampathkumar, P., Suresh, C., Sathish, M., & Mathiyarasu, J. (2023). Doable high energy density supercapacitors using rice husk-derived carbon in dihydroxybenzenes as redox-additive electrolytes. Journal of Energy Storage, 74, 109407.

Subhiksha, V., Alatar, A. A., Okla, M. K., Alaraidh, I. A., Mohebaldin, A., Aufy, M., Abdel-Maksoud, M. A., Raju, L. L., Thomas, A. M., & Khan, S. S. (2022). Double Z-Scheme $ZnCo_2O_4/MnO_2/FeS_2$ photocatalyst with enhanced photodegradation of organic compound: Insights into mechanisms, kinetiCs, pathway and toxicity studies. Chemosphere, 303(P3), 135177.

Suganya, S., Alam, M. M., Kousi, F., Ramalingam, G., Prabhu, M. R., & Sudhahar, S. (2023). Facile one-pot synthesis of ternary Ni-Mn-Zn oxide nanocomposites for high-performance hybrid supercapacitors. Journal of Energy Storage, 71, 108176.

Suganya, S., Balaji, G., & Vadivel, S. (2023). Hybridization of graphene into $NiCo_2S_4$ hybrid composites as electrode materials for high performance supercapacitors. Chemical Physics, 573, 112000.

Suganya, S., Maheshwaran, G., Ramesh Prabhu, M., Devendran, P., Krishna Kumar, M., & Sudhahar, S. (2022). Enhanced electrochemical activity of ternary Co-Mn-Zn oxide for the fabrication of hybrid supercapacitor applications. Journal of Energy Storage, 56, 106057.

Tekin, B., & Topcu, Y. (2024). Novel hemp biomass-derived activated carbon as cathode material for aqueous zinc-ion hybrid supercapacitors: Synthesis, characterization, and electrochemical performance. Journal of Energy Storage, 77, 109879.

Thejas Prasannakumar, A., Rohith, R., Manju, V., R. Mohan, R., & J. Varma, S. (2024). Graphene nanoflake-self stabilized dispersion polymerized PANI hybrids as efficient, binder-free electrode materials for high-performance flexible symmetric supercapacitors. Journal of Electroanalytical Chemistry, 952, 117952.

Thokoane, T. L., Nhlapo, T. A., Adoons, V. N., Kotsedi, L., Mokoena, T. P., Mahule, T. S., Mokhena, T. C., & Moyo, T. (2024). Structural, magnetic and photoluminescence properties of Zn-Ni ferrites synthesized by hydrothermal method. Journal of Molecular Structure, 1315, 138906.

Tiwari, N., Kadam, S., & Kulkarni, S. (2021). Synthesis and characterization of $ZnCo_2O_4$ electrode for high-performance supercapacitor application. Materials Letters, 298, 130039.

Uke, S. J., Mardikar, S. P., Bambole, D. R., Kumar, Y., & Chaudhari, G. N. (2020). Sol-gel citrate synthesized Zn doped $MgFe_2O_4$ nanocrystals: A promising supercapacitor electrode material. Materials Science for Energy Technologies, 3, 446–455.

Uma Sudharshini, A., Bououdina, M., Venkateshwarlu, M., Manoharan, C., & Dhamodharan, P. (2020). Low temperature solvothermal synthesis of pristine Co_3O_4 nanoparticles as potential supercapacitor. Surfaces and Interfaces, 19, 100535.

Umeshbabu, E., Rajeshkhanna, G., & Rao, G. R. (2014). Urchin and sheaf-like $NiCo_2O_4$ nanostructures: Synthesis and electrochemical energy storage application. International Journal of Hydrogen Energy, 39(28), 15627–15638.

Ur Rehman, A., Arshad, M. I., & Amin, N. (2024). Transport and magnetic properties of $Zn_{0.5}$ $Co_{0.25}Cu_{0.25}Ho_{0.037}Fe_{1.963}O_4$/Graphene nanoplatelets nanocomposites. Ceramics International, 50 (24), 55940-55952.

Vázquez-Lizardi, G. A., Ruiz-Casanova, L. A., Cruz-Sánchez, R. M., & Santana, J. A. (2021). Simulation of metal-supported metal-Nanoislands: A comparison of DFT methods. Surface Science, 712, 1–8.

Vigneshwaran, S., Preethi, J., & Meenakshi, S. (2020). Interface engineering of ultrathin multi-functional 2D draped chitosan for efficient charge separation on degradation of paraquat â' A mechanistic study. Journal of Environmental Chemical Engineering, 8(5), 104446.

W. Kohn, & L.J. Sham. (1965). Self-Consistent Equations Including Exchange and Correlation Effects. Physical Review, 140(4A), A 1133.

Wang, D., Liang, Z., Gao, S., Qu, C., & Zou, R. (2020). Metal-organic framework-based materials for hybrid supercapacitor application. Coordination Chemistry Reviews, 404, 213093.

Wang, J., Tu, J., Lei, H., & Zhu, H. (2019). The effect of graphitization degree of carbonaceous material on the electrochemical performance for aluminum-ion batteries. RSC Advances, 9(67), 38990–38997.

Wang, L., Wu, J., & Fu, S. (2023). A mini review of recent progress in Mo-based electrode materials for supercapacitors. Inorganic Chemistry Communications, 148, 110329.

Wang, L., Xu, J. C., Han, Y. B., Jin, H. X., Hong, B., Jin, D. F., Gong, J., Peng, X. L., Ge, H. L., & Wang, X. Q. (2022). Nanocasting synthesis and highly-improved toluene gas-sensing performance of Co_3O_4 nanowires with high-valence Sn-doping. Chemical Physics, 560, 6587-6596.

Wang, Lina, Wu, J., & Fu, S. (2023). A mini review of recent progress in Mo-based electrode materials for supercapacitors. Inorganic Chemistry Communications, 148, 110329.

Wang, X., Liu, B., Wang, S., Xie, H., Zha, Y., Huang, X., Santos, D. M. F., & Li, Y. (2023). Oxygen self-doped hierarchical porous carbons derived from coal liquefaction residue for high-performance supercapacitors in organic and ionic liquid-based electrolytes. Colloids and Surfaces A: Physicochemical and Engineering Aspects, 669, 131552.

Wang, Y., Yi, J., & Xia, Y. (2012). Recent progress in aqueous lithium-ion batteries. Advanced Energy Materials, 2(7), 830–840.

Wei, X., Zhou, Y., Shen, X., Di, J., Wang, X., & Li, Q. (2021). Facile synthesis of ultrathin $ZnCo_2O_4$ nanosheets/carbon cloth composite electrode for hybrid supercapacitors with high-rate and excellent reversibility. Materials Letters, 293, 129636.

Wu, L., Sun, L., Li, X., Zhang, Q., Si, H., Zhang, Y., Wang, K., & Zhang, Y. (2020). Mesoporous $ZnCo_2O_4$-CNT microflowers as bifunctional material for supercapacitive and lithium energy storage. Applied Surface Science, 506, 144964–144975.

Wu, M. S., Zheng, Z. Bin, Lai, Y. S., & Jow, J. J. (2015). Nickel cobaltite nanograss grown around porous carbon nanotube-wrapped stainless steel wire mesh as a flexible electrode for high-performance supercapacitor application. Electrochimica Acta, 182, 31–38.

Xiang, J., Xiang, B., & Cui, X. (2018). NiO nanoparticle surface energy studies using first principles calculations. New Journal of Chemistry, 42(13), 10791–10797.

Xiang, K., Wu, D., Fan, Y., You, W., Zhang, D., Luo, J. L., & Fu, X. Z. (2021). Enhancing bifunctional electrodes of oxygen vacancy abundant $ZnCo_2O_4$ nanosheets for supercapacitor and oxygen evolution. Chemical Engineering Journal, 425, 130583.

Xie, Lei, Kai Yuan, Jianxiong Xu, Yirong Zhu, Lijian Xu, Na Li, and Jingjing Du. (2020). Comparative Study on Supercapacitive Performances of Hierarchically Nanoporous Carbon Materials With Morphologies From Submicrosphere to Hexagonal Microprism. Frontiers in Chemistry, 8, 1–13.

Xin, X., Kang, H., Feng, J., Sui, L., Dong, H., Zhao, P., Pang, B., Chen, Y., Sun, Q., Ma, S., Zhang, R., Dong, L., & Yu, L. (2020). A novel sol-gel strategy for N, P dual-doped mesoporous carbon with high specific capacitance and energy density for advanced supercapacitors. Chemical Engineering Journal, 393, 124710.

Xu, M., Sun, M., Rehman, S. ur, Ge, K., Hu, X., Ding, H., Liu, J., & Bi, H. (2020). One-pot synthesis of CoO-ZnO/rGO supported on Ni foam for high-performance hybrid supercapacitor with greatly enhanced cycling stability. Chinese Chemical Letters.

Xu, Y., Xiao, M., Liu, T., Lin, R., Meng, Y., Zhang, Y., & Zhu, F. (2023). Nitrogen, boron and fluorine tri-doped carbon nanotubes on carbon cloth as the electrode materials for supercapacitors. Journal of Electroanalytical Chemistry, 948, 117812.

Yang, Y., Li, Z., Zhao, J., & Qu, S. (2023). Structural engineering of pitch-based porous carbon and its application in supercapacitors: A review. Journal of Energy Storage, 74, 109334.

Yi, C. qi, Zou, J. peng, Yang, H. zhi, & Leng, X. (2018). Recent advances in pseudocapacitor electrode materials: Transition metal oxides and nitrides.

Transactions of Nonferrous Metals Society of China (English Edition), 28(10), 1980–2001.

Yu, J., Cui, Z., Li, X., Chen, D., Ji, J., Zhang, Q., Sui, J., Yu, L., & Dong, L. (2020). Facile fabrication of ZIF-derived graphene-based 2D Zn/Co oxide hybrid for high-performance supercapacitors. Journal of Energy Storage, 27, 101165.

Zaki, N. H. M., Ali, A. M. M., Yaakob, M. K., Taib, M. F. M., Hassan, O. H., Lepit, A., & Yahya, M. Z. A. (2021). Structural and electronic properties of nickel doped cobalt oxide electrode for supercapacitors: A first principle study. IOP Conference Series: Earth and Environmental Science, 685(1), 012029.

Zakutayev, A., Perkins, J. D., Parilla, P. A., Widjonarko, N. E., Sigdel, A. K., Berry, J. J., & Ginley, D. S. (2011). Zn–Ni–Co–O wide-band-gap p-type conductive oxides with high work functions. MRS Communications, 1(1), 23–26.

Zhang, Wei, Du, X., Tan, Y., Hu, J., Li, Z., & Tang, B. (2017). Amorphous Cobalt Boron Alloy@Graphene Oxide Nanocomposites for Pseudocapacitor Applications. Journal of Materials Science and Technology, 33(5), 438–443.

Zhang, Wenjuan, Xu, C., Liu, E., Fan, J., & Hu, X. (2020). Facile strategy to construction Z-scheme $ZnCo_2O_4$/g-C_3N_4 photocatalyst with efficient H_2 evolution activity. Applied Surface Science, 515, 146039.

Zhang, Y., Wang, J., Ye, J., Wan, P., Wei, H., Zhao, S., Li, T., & Hussain, S. (2016). $NiCo_2O_4$ arrays nanostructures on nickel foam: Morphology control and application for pseudocapacitors. Ceramics International, 42(13), 14976–14983.

Zhang, Yan, Lianjie Huang, Xiaxin Lei, Hao Huang, Wei Guo, and Shuang Wang. 2023. Hierarchical Ternary Zn-Ni-Co Sulfide/Oxide Heterostructure for High Specific Energy Hybrid Supercapacitor. Journal of Alloys and Compounds, 962, 171201.

Zhao, X., Wei, H., Zhao, H., Wang, Y., & Tang, N. (2020). Electrode materials for capacitive deionization: A review. Journal of Electroanalytical Chemistry, 873, 114416.

Zhao, Y., Wang, Z., Yuan, R., Lin, Y., Yan, J., Zhang, J., Lu, Z., Luo, D., Pietrasik, J., Bockstaller, M. R., & Matyjaszewski, K. (2018). ZnO/carbon hybrids derived

from polymer nanocomposite precursor materials for pseudocapacitor electrodes with high cycling stability. Polymer, 137, 370–377.

Zhao, Y., Wang, Z., Yuan, R., Lin, Y., Yan, J., Zhang, J., Lu, Z., Luo, D., Pietrasik, J., Bockstaller, M. R., & Matyjaszewski, K. (2018). ZnO/carbon hybrids derived from polymer nanocomposite precursor materials for pseudocapacitor electrodes with high cycling stability. Polymer, 137, 370–377.

Zhu, F., She, X., Zhang, Z., Yu, X., Ji, J., Li, L., & Li, S. (2024). Flexible reduced graphene oxide/polypyrrole films for supercapacitors. Diamond and Related Materials, 141, 110581.

Zhu, Y., Ji, X., Wu, Z., Song, W., Hou, H., Wu, Z., He, X., Chen, Q., & Banks, C. E. (2014). Spinel $NiCo_2O_4$ for use as a high-performance supercapacitor electrode material: Understanding of its electrochemical properties. Journal of Power Sources, 267, 888–900.

Zhu, Yuanfei, Zengren Tao, Chengyan Cai, Yuanming Tan, Anding Wang, and Yangyi Yang. (2022). Facile Synthesis Zn-Ni Bimetallic MOF with Enhanced Crystallinity for High Power Density Supercapacitor Applications. Inorganic Chemistry Communications, 139, 109391.

Zikirina, A., Kadyrzhanov, K. K., Kenzhina, I. E., Kozlovskiy, A. L., & Zdorovets, M. V. (2021). Study of defect formation processes under heavy ion irradiation of $ZnCo_2O_4$ nanowires. Optical Materials, 118, 111282.

APPENDICES

Chemical calculation of Zn/Ni/Co MTMOs system

1. 1:1:1

Precursor masses

$Zn(NO_3)_2 \cdot 6H_2O$: 5.687 mmol = 1.692 g

$Ni(NO_3)_2 \cdot 6H_2O$: 5.687 mmol = 1.654 g

$Co(NO_3)_2 \cdot 6H_2O$: 5.687 mmol = 1.655 g

2. 1:2:1

Precursor masses

$Zn(NO_3)_2 \cdot 6H_2O$: 3.338 mmol = 0.993 g

$Ni(NO_3)_2 \cdot 6H_2O$: 6.677 mmol = 1.942 g

$Co(NO_3)_2 \cdot 6H_2O$: 3.338 mmol = 0.972 g

3. 1:1:2

Precursor masses

$Zn(NO_3)_2 \cdot 6H_2O$: 3.338 mmol = 0.993 g

$Ni(NO_3)_2 \cdot 6H_2O$: 3.338 mmol = 0.971 g

$Co(NO_3)_2 \cdot 6H_2O$: 6.677 mmol = 1.943 g

4. 2:1:1

Precursor masses

$Zn(NO_3)_2 \cdot 6H_2O$: 2.293 mmol = 0.682 g

$Ni(NO_3)_2 \cdot 6H_2O$: 1.147 mmol = 0.333 g

$Co(NO_3)_2 \cdot 6H_2O$: 1.147 mmol = 0.334 g

AUTHOR'S PROFILE

Nurul Infaza Talalah obtained her Bachelor of Science in Physics with Electronics (Hons.) in 2009 from University Malaya Sabah, MSc in Nanotechnology (2016) from Universiti Putra Malaysia.

LIST OF PUBLICATION:

Ramli, Nurul Infaza Talalah, Hartini Ahmad Rafaie, Mohd Firdaus Kasim, and Mohd Syafiq Affandi. 2021. "Improved Capacitive Performance of Activated Carbon-Doped Titanium Dioxide for Supercapacitor Electrode Material" 14, Specia (1): 63–69.

Rafaie, Hartini Ahmad, Syazni Hanun Nur Ili Dasiano, Muhd Firdaus Kasim, Nurul Infaza Talalah Ramli, Zul Adlan Mohd Hir, and Mohamad Hafiz Mamat. 2022. "Constructing Ni-Doped ZNO/GO Heterostuctures For Enhanced Sunlight-Triggered Degradation Of Methylene Blue Dye." *Malaysian Journal of Analytical Sciences* 26 (3): 520–31.

Ramli, Nurul Infaza Talalah, Suraya Abdul Rashid, Yusran Sulaiman, Md Shuhazlly Mamat, Syazwan Afif Mohd Zobir, and Shutesh Krishnan. 2016. "Physicochemical and Electrochemical Properties of Carbon Nanotube/Graphite Nanofiber Hybrid Nanocomposites for Supercapacitor." *Journal of Power Sources* 328: 195–202.

Ramli, Nurul Infaza Talalah, Ab Malik Marwan Ali, Nur Hafiz Hussin, Mohamad Fariz Mohamad Taib, and Oskar Hasdinor Hassan. 2024. “Unveiling Zn/Ni/Co Ternary Mixed Transition Metal Oxides Composite Anchored on Graphene Oxide As a Potential Material for Supercapacitor Electrode.” *Malaysian Journal of Analytical Sciences* 28 (4): 886–98.

Ramli, Nurul Infaza Talalah, Suraya Abdul Rashid, Md Shuhazlly Mamat, Yusran Sulaiman, and Shutesh Krishnan. 2018. “Incorporation of Iron Oxide into CNT/GNF as a High-Performance Supercapacitor Electrode.” *Materials Chemistry and Physics* 212: 318–24.

Ramli, Nurul Infaza Talalah, Suraya Abdul Rashid, Md Shuhazlly Mamat, Yusran Sulaiman, Syazwan Afif Zobir, and Shutesh Krishnan. 2017. “Incorporation of Zinc Oxide into Carbon Nanotube/Graphite Nanofiber as High Performance Supercapacitor Electrode.” *Electrochimica Acta* 228: 259–67.

Ramli, Nurul Infaza Talalah, Hartini Ahmad Rafaie, Muhd Firdaus Kasim, and Hanifa Binti Ibno. 2019. “Facile Preparation of Activated Carbon/Zinc Oxide Nanocomposite for Supercapacitor Application.” *Recent Innovations in Chemical Engineering (Formerly Recent Patents on Chemical Engineering)* 13 (3): 223–31.

Ramli, Nurul Infaza Talalah, Ab Malik Marwan Ali, Nur Hafiz Hussin, Mohamad Fariz Mohamad Taib, and Oskar Hasdinor Hassan. 2023. “Unravelling the Supercapacitive Potential of Zn-Ni-Co Mixed Transition Metal Oxide.” *Recent Innovations in Chemical Engineering*.

Ramli, Nurul Infaza Talalah, Ab Malik Marwan Ali, Nur Hafiz Hussin, Mohamad Fariz Mohamad Taib, and Oskar Hasdinor Hassan. 2025. “A Theoretical Insight into the Electronic and Optical Behavior of $ZnCo_2O_4$.” *Journal of Advanced Research in Micro and Nano Engineering* 28 (1): 95–104.